The Dissertation Committee for Swathi Mahalaxmi Mula
certifies that this is the approved version of the following dissertation:

Stability and turbulence characteristics of a spiraling vortex filament using proper orthogonal decomposition

Committee:

Charles E. Tinney, Supervisor

David B. Goldstein

Venkatramanan Raman

Jayant Sirohi

David G. Bogard

Stability and turbulence characteristics of a spiraling vortex filament using proper orthogonal decomposition

by

Swathi Mahalaxmi Mula, B.E.

DISSERTATION

Presented to the Faculty of the Graduate School of

The University of Texas at Austin

in Partial Fulfillment

of the Requirements

for the Degree of

DOCTOR OF PHILOSOPHY

THE UNIVERSITY OF TEXAS AT AUSTIN

May 2015

Dedicated to my family and friends.

Acknowledgments

I am thankful to all the people who have motivated and supported me in this entire journey of my graduate life. I am truly indebted to my academic advisor Dr. Charles E. Tinney for introducing me to the world of scientific research in fluid dynamics and guiding me towards the righteous path in my career. I would like to deeply express my gratitude for the thoughtful discussions we had together that had greatly influenced me in my thinking and action as a researcher. I appreciate his support in providing me with all the resources for the successful completion of the projects we worked together. I would also like to sincerely express my gratitude to Dr. Jayant Sirohi for the numerous discussions and the support provided to my research. I would like to extend my deepest appreciation to other members of my committee, Dr. David B. Goldstein, Dr. Venkatramanan Raman and Dr. David G. Bogard, for their time and helpful recommendations to my research.

I would like to acknowledge Chris Cameron, my fellow graduate student, for his assistance with the PIV measurements. I would like to extend my sincere appreciation to the staff members at the Department of Aerospace Engineering and Engineering Mechanics for the numerous support provided: Joseph Pokluda for the machine work, Pablo Cortez for the help with electronics, Scott Messec for the IT support, and Geetha Rajagopal for the ad-

ministrative work. I would also like to thank my friends and fellow graduate students at UT for the research discussions and friendly interactions which were stress-busting.

I would like to acknowledge the financial support provided by the Army/Navy/NASA Verticla Lift Research Center of Excellence (VLRCOE) led by the University of Maryland; Grant No. W911W6-11-2-0012.

On a more personal note, I am deeply indebted to my parents and my dear husband, Shireesh Annam, for the unconditional support. Without you, I could have not come this far. To my siblings, family and friends, you have always been encouraging. I thank you for being morale boosters and appreciate your patience at difficult times.

Stability and turbulence characteristics of a spiraling vortex filament using proper orthogonal decomposition

Swathi Mahalaxmi Mula, Ph.D.
The University of Texas at Austin, 2015

Supervisor: Charles E. Tinney

The stability and turbulence characteristics of a vortex filament emanating from a single-bladed rotor in hover are investigated using proper orthogonal decomposition. The rotor is operated at a tip chord Reynolds number and a tip Mach number of 218,000 and 0.22, respectively, and with a blade loading of $C_T/\sigma = 0.066$. In-plane components of the velocity field (normal to the axis of the vortex filament) are captured by way of 2D particle image velocimetry with corrections for vortex wander being performed using the Γ_1 method. Using the classical form of POD, the first POD mode alone is found to encompass nearly 75% of the energy for all vortex ages studied and is determined using a grid of sufficient resolution as to avoid numerical integration errors in the decomposition. The findings reveal an equal balance between the axisymmetric and helical modes during vortex roll-up which immediately transitions to helical mode dominance at all other vortex ages. This helical mode is one of the modes of the elliptic instability. While the snapshot POD is shown to reveal similar features of the first few energetic modes, the classical POD

is employed here owing to the easier interpretation of the Fourier-azimuthal modes. The spatial eigenfunctions of the first few Fourier-azimuthal modes associated with the most energetic POD mode are shown to be sensitive to the choice of the wander correction technique used. Higher Fourier-azimuthal modes are observed in the outer portions of the vortex and appeared not to be affected by the choice of the wander correction technique used.

Table of Contents

Acknowledgments v

Abstract vii

Nomenclature xii

List of Tables xv

List of Figures xvi

Chapter 1. Introduction 1
- 1.1 Fixed-wing aircraft trailing vortices . . . 2
- 1.2 Helicopter rotor trailing vortices . . . 3
  - 1.2.1 Turbulence in the vortex . . . 5
- 1.3 Vortex instabilities . . . 7
  - 1.3.1 Elliptic instability . . . 9
  - 1.3.2 Vortex breakdown . . . 14
  - 1.3.3 Stability investigations on spiraling vortex filaments . . . 15
- 1.4 Scope of the current research . . . 29
- 1.5 Outline of subsequent chapters . . . 30

Chapter 2. Experimental setup 32
- 2.1 Rotor setup . . . 32
- 2.2 Particle image velocimetry (PIV) . . . 35
- 2.3 PIV measurements of a rotor wake in hover . . . 39
  - 2.3.1 Measurements accuracies . . . 44
    - 2.3.1.1 Magnification errors . . . 45
    - 2.3.1.2 Particle tracking errors . . . 46
    - 2.3.1.3 Peak locking errors . . . 49
  - 2.3.2 PIV vector processing . . . 51

Chapter 3. Analysis technique **53**
3.1 Vortex center identification techniques 54
3.1.1 Centroid of Q (CoQ) 54
3.1.2 Centroid of vorticity 55
3.1.3 Normalized helicity 56
3.1.4 Γ_1 method 56
3.1.5 Geometric center 57
3.2 Vortex characteristics 59
3.2.1 Vortex wander 59
3.2.2 Convergence test 62
3.2.3 Mean statistics 65
3.3 Low dimensional representation using POD 72
3.3.1 Snapshot POD 72
3.3.2 Classical POD 74
3.3.2.1 Low dimensional axial vorticity 77

Chapter 4. Low-dimensional characteristics **78**
4.1 Grid resolution for POD 78
4.2 Energy spectrum 79
4.2.1 Spatial structures of the Fourier modes of the first POD mode ($n = 1$) 83
4.2.1.1 Asymmetries in the vortex filament 98
4.2.2 Spatial structures of the Fourier modes for the second POD mode 101

Chapter 5. Comparisons between classical and snapshot forms of POD applied to spiraling vortex filament **105**
5.1 Energy spectrum and organized motions 105
5.1.1 Asymmetries in the vortex filament 114

Chapter 6. Sensitivity of POD to the choice of the vortex centering technique **123**
6.1 Mean statistics 125
6.2 Low-dimensional characteristics 130

6.2.1 Fourier-azimuthal modes for the first $n = 1$ POD mode . 132
6.2.1.1 Higher Fourier modes associated with the first $n = 1$ POD mode 144

Chapter 7. Summary and future work **151**
7.1 Summary 151
7.2 Future work 160

Bibliography **162**

Nomenclature

$\boldsymbol{\sigma}$	Standard deviation of wander
χ	Total resolved kinetic energy of the mean vortex flow
Γ_v	Circulation strength of the vortex filament
$\hat{\tau}$	Torsion of the helix
$\hat{p}$	Pitch of the helix
$\mathfrak{E}$	Low-dimensional turbulence kinetic energy per unit mass
$\mathfrak{u}_{i=1,2}$	Fluctuating part of the low-dimensional in-plane velocity components
ν	Kinematic viscosity of the fluid (air)
Ω	Rotation speed of the rotor
ψ	Vortex age
ρ	Density of the fluid (air)
σ	Rotor solidity
$\tilde{u}_{i=1,2}$	Instantaneous in-plane velocity components
Ξ	Total resolved turbulence kinetic energy
c	Blade chord
C_T	Coefficient of thrust

C_T/σ	Blade loading
L_m	Measurement resolution
m	Fourier-azimuthal mode
Ma	Tip Mach number
n	POD mode in the classical form of POD
N_b	Number of blades
n_s	POD mode in the snapshot form of POD
R	Rotor radius
R_c	Radius of curvature of the helix
r_c	Core-radius
Re	Tip chord Reynolds number
S_k	Stokes number
$U_{i=1,2}$	In-plane mean velocity components
$u_{i=1,2}$	Fluctuating part of the in-plane velocity components
V_Θ	Swirl (or tangential) velocity
V_{tip}	Blade tip speed
$z\prime$	Coordinate along the axis perpendicular to the measurement plane
β^n	Normalized eigenspectra in the classical form of POD
ω_z	Axial vorticity (parallel to the vortex axis)

ε^f Normalized eigenspectra in the snapshot form of POD

(r, θ) Polar coordinates along the measurement plane with the origin at the vortex center

$(x\prime, y\prime)$ Cartesian coordinates along the measurement plane with the origin at the vortex center

$(x\star, y\star)$ Instantaneous position of the vortex from the mean vortex center

CoQ Centroid of Q

FOV Field of view

GC Geometric center

PIV Particle Image Velocimetry

POD Proper Orthogonal Decomposition

RPM Revolutions per Minute

TKE Turbulence Kinetic Energy (per unit mass)

List of Tables

1.1 Parameters of the helical vortex filament studied here. 22

2.1 Rotor parameters and test conditions. 36
2.2 Particle tracking error estimates in tangential velocity. 47
2.3 Particle tracking error estimates in radial velocity. 48
2.4 Peak locking estimates. 49

3.1 Overview of the experimental conditions reported by others on the core-radius estimates using twisted ($\oplus$) and untwisted ($\star$) blades. 66
3.2 Estimates of the binormal induced velocity measured from the current experiment compared with the theoretical predictions using Eq. 3.6. 69

List of Figures

1.1 Counter-rotating flow structures in the trailed vortex sheet taken from the measurements of Ramasamy *et al.* (2009b) [75]. . . . 4

1.2 Scatter plot of vortex position at sample vortex ages taken from Mula *et al.* (2013) [64]. . . . 4

1.3 Structure of a trailing vortex taken from Ramasamy *et al.* (2009b) [75] highlighting (1) the laminar inner region, (2) an intermediate transitional region and, (3) the outer turbulent region. . . . 5

1.4 Long-wave and short-wave instabilities taken from the flow-visualization study of Leweke & Williamson (1998) [46]. . . . 8

1.5 Close-up view of short-wave instabilities taken from the flow-visualization study of Leweke & Williamson (1998) [46]. . . . 9

1.6 Axial vorticity field of a linear mode structure of the elliptic instability in the transverse plane as described by Sipp (2000) [82]. Solid and dashed lines indicate opposite signs of vorticity. . . . 11

1.7 Contour plot of axial vorticity of the most unstable mode of the elliptic instability in the numerical investigations of Schaeffer & Dizer [80]. (a) Linear regime and (b) weakly non-linear regime. Solid and dashed lines correspond to positive and negative isovorticity contours respectively. . . . 12

1.8 (a-e) Evolution of axially averaged vorticity contours in a plane perpendicular to the vortex axis (in strongly nonlinear regime of elliptic instability) in the numerical investigations of Schaeffer & Dizer [80]. . . . 13

1.9 Vortex breakdown in the flow visualization study of Leweke & Williamson [47]. . . . 15

1.10 Non-dimensional amplification rate (or growth rate of perturbations) for helices at a sample pitch with an instability mode of $\gamma/k\prime$ waves per cycle (wavenumber) as found by Widnall (1972) [94]. The values of the ratio of vortex core radius to the radius of cylinder (that encloses helix) are shown on each curve [94]. . . . 17

1.11 Instability mode shapes for sample wavenumbers taken from Widnall (1972) [94]. Dark portions are outside the cylinder on the near side while light portions are on the inside. . . . 18

1.12 Schematic showing the velocity induced by a straight-line vortex filament AB [9]. Γ_v is the circulation strength of the vortex filament. 18

1.13 Maximum divergence rates (or growth rate of perturbations) for the one-, two-, and four-bladed hovering rotors at constant blade-loading, $C_T/\sigma = 0.075$, from the numerical studies of Bhagwat & Leishman (2000) [9]. 21

1.14 Maximum non-dimensional divergence rates (or growth rate of perturbations) for one-, two-, three- and four-intertwining helical vortex filaments. 23

1.15 Instabilities on rotor-tip vortex filaments of a three-bladed rotor (at 4 revolutions per second) in hover in the flow visualization study of Ohanian *et al.* (2012) [66]. b1-blade 1, b2-blade 2, b3-blade 3; v1, v2, v3 represent vortex filaments from blades 1, 2, and 3, respectively. 24

1.16 Traces of short-wave instabilities on rotor-tip vortex filaments of a three-bladed rotor (at 8 revolutions per second) in hover in the flow visualization study of Ohanian *et al.* (2012) [66]. . . . 24

1.17 Short-wave and Long-wave instabilities on tip vortex filaments from a horizontal axis one-bladed wind turbine taken from Leweke *et al.* (2014) [48]. 25

1.18 Schematic of vortex wander and coordinate system (for in-plane motions) with respect to the mean slipstream boundary provided by Mula *et al.* (2013) [64]. Vortices 1, 2, 3, and 4 represent tip vortices from blades 1, 2, 3, and 4, respectively. 26

1.19 Wander of vortex from blade 2 overlaid the 95% confidence region for vortex ages between (a) 10° - 80°, (b) 100° - 170°, (c) 190° - 260° using CoQ in the measurements of Mula *et al.* (2013) [64]. Dashed lines are separated by $y\star/R = 0.03$; $x\star/R = 0.03$. 27

1.20 Phase motion of the (a) $x\star$ and (b) $y\star$ displacements in figure 1.18 between vortex 4 and vortex 3 using CoQ in the measurements of Mula *et al.* (2013) [64]. The 95% confidence interval region has been drawn. Dashed lines are separated by $y\star/\boldsymbol{\sigma}_y = 3$; $x\star/\boldsymbol{\sigma}_x = 3$. 29

2.1 Rotor test stand. 33

2.2 (a) Rotor blade and (b) its airfoil (NACA 0012). 34

2.3 Close-up view of the rotor hub. 34

2.4 Counter weight in (a) side view and (b) bottom view. 35

2.5 General setup of a 2D PIV system [18]. 38
2.6 General method for evaluating PIV measurements [18]. 38
2.7 Schematic of the experimental setup and coordinate transformation. 40
2.8 Tip vortices seen by dark voids of seed in the illuminated laser sheet. 41
2.9 Schematic of a two-level calibration plate [18]. 42
2.10 Schematic (unscaled) of the measurement plane, calibration plane and laser sheet. Front edge of the calibration plate represents the calibration plane. 43
2.11 (Top) (a) Histogram of the measurement horizontal displacement and (b) its corresponding sub-pixel component. (Bottom) (a) Histogram of the measurement vertical displacement and (b) its corresponding sub-pixel component. Bin size is 0.05 pixels and the plots are illustrated for a sample instantaneous data at $\psi = 90°$. 50
2.12 (a) Sample PIV snapshot at $\psi = 45°$ and (b) the corresponding original vector map (sub-sampled) with (c) the corresponding post-processed vector map. The vortex center and core boundary are also identified. 52

3.1 Schematic illustration for the Γ_1 method. 57
3.2 (a) Q method applied to a sample vortex at 250° vortex age from the measurements of Mula *et al.* (2013) [64]. Dark circles identify locations of peak swirl velocity. (b) Sub-sampled PIV vector map at 40° wake age from the studies of Mula *et al.* (2013) [64]. Vortex centers detected using CoQ (circle), centroid of vorticity (diamond), maximum normalized helicity (square), Γ_1 method (triangle-up), GC-ellipse (star) and GC-average (triangle-down) 58
3.3 Instantaneous PIV vector map (sub-sampled) at $\psi = 180°$ with the vortex center (○) identified using the Γ_1 method. 60
3.4 (a) Vortex wander with a 95% confidence ellipse at $\psi = 45° - 585°$. Dashed lines are separated by 0.04 in $x\star/R$ and 0.02 in $y\star/R$. (b) Standard deviation of vortex wander along the principal major (◇, |) and minor (△, ...) axes. 61
3.5 (a) Schematic illustration for the vortex wander correction. M and I are the mean and instantaneous vortex centers, respectively. Mean velocity vector field (sub-sampled) at $\psi = 180°$ (b) before and (c) after wander correction. Corresponding vortex core boundaries are also identified. 63

3.6 (a) Convergence of mean core-radius. (b) Convergence of mean swirl velocity, $|V_\Theta/V_{tip}|$, on a vortex slice: number of samples $N_s = 25 - 350$ 64

3.7 Core-radius trends of the current study (C) compared to the previous studies listed in table 3.1. 65

3.8 Contours of the mean axial vorticity (ω_z/Ω) at $\psi = 45°$ to 495°. Locations of peak swirl velocity ($V_{\Theta,max}$), which define the boundaries of the vortex core, also identified. 67

3.9 Turbulent kinetic energy per unit mass, $(\text{TKE}/V_{tip}^2) \times 10^3$, at (a) $\psi = 180°$ and (b) $\psi = 315°$. Locations of peak swirl velocity ($V_{\Theta,max}$) also identified. 69

3.10 Swirl velocity, $(|V_\Theta|/V_{tip}) \times 20$ ($\bigtriangledown$), and $(\text{TKE}/V_{tip}^2) \times 10^3$ ($\star$) at (a) $\psi = 180°$ and (b) $\psi = 315°$ on a vortex slice. 70

3.11 Total resolved turbulence kinetic energy (Ξ) normalized with the total resolved kinetic energy (χ) of the mean flow. 71

3.12 Coordinate transformation. 74

4.1 Sensitivity of the POD eigenvalues to the grid resolution $\Delta r/r_c$. (a) $n = 1$, (b) $n = 2$, and (c) $n = 3$. 80

4.2 (a) Energy spectra of the first seven POD modes. (b) Energy spectra of the POD modes on a logarithmic scale. 81

4.3 Fourier mode energy spectra of the first ($n = 1$) POD mode for $m = 0$, 1, 2 and 3. 82

4.4 Radial profiles of vorticity and circulation profiles for $(m, n) = (0, 1)$ at (a) $\psi = 45°$ and (b) $\psi = 315°$. 83

4.5 Contours of the (a) real and (b) imaginary components of the axial vorticity of the helical mode $(m, n) = (1, 1)$ at $\psi = 135°$. Circles of mean core-radius (|) and peak TKE (....) are indicated. 84

4.6 Schematic of a helical mode of the elliptic instability. (a) Base flow with circular streamlines, (b) application of the helical mode to the base flow, and (c) resultant flow of elliptical streamlines. 85

4.7 Schematic of a helical mode of the elliptic instability. (a) Base flow with circular streamlines, (b) application of the helical mode to the base flow, and (c) resultant flow of elliptical streamlines with expansion ($\mathfrak{e}$) and contraction ($\mathfrak{c}$) of streamlines . . 87

4.8 Axial vorticity contours of the modes of the elliptic instability observed by (a) Pierrehumbert (1986) [67] and (b) Sipp (2000) [82]. 88

4.9 Contours of the real component of the axial vorticity of the helical mode $(m, n) = (1, 1)$ at $\psi = 45° - 495°$. Circles of mean core-radius (|) and peak TKE (....) are indicated. 89

4.10 (a) Mean axial vorticity (ω_z/Ω), (b) reconstruction of the fluctuating vorticity at an instant in time using $(m, n) = (1, 1)$, (c) mean vorticity plus the $(1, 1)$ mode at $\psi = 405°$. Core-boundaries for the mean (black) and low-dimensional (red) vortices also indicated. 91

4.11 (a) Original instantaneous vorticity at an instant in figure 4.10 and (*b*) the corresponding core-boundaries for the mean (figure 4.10a), low-dimensional (figure 4.10b) and original instantaneous vortices for a sample set of data at $\psi = 405°$. Mean (black), low-dimensional (red) and instantaneous (blue) core boundaries. 92

4.12 Contours of the (a) real and (b) imaginary components of the axial vorticity of the double helical mode $(m, n) = (1, 1)$ at $\psi = 135°$. Circles of mean core-radius (|) and peak TKE (....) are indicated. 93

4.13 Schematic of a double helical mode of the elliptic instability. (a) Base flow with circular streamlines, (b) application of the double helical mode to the base flow, and (c) resultant flow of elliptical streamlines. 94

4.14 Light intensity of the four-lobed structures of the double helical mode of the elliptic instability from the findings of Roy *et al.* (2011) [79]. 95

4.15 Contours of the real component of the axial vorticity of the double helical mode $(m, n) = (2, 1)$ at $\psi = 45° - 495°$. Circles of mean core-radius (|) and peak TKE (....) are indicated. . . . 97

4.16 Turbulence kinetic energy per unit mass, $(\text{TKE}/V_{tip}^2) \times 10^3$, at (a) $\psi = 180°$ and (b) $\psi = 315°$. Vortex core boundary identified by the locations of peak swirl velocity $(V_{\Theta,max})$ also identified. 98

4.17 $(\mathfrak{E}/V_{tip}^2)\times 10^3$ constructed using the individual Fourier modes for the first $(n = 1)$ POD mode at (a) $\psi = 180°$ and (b) $\psi = 315°$ on a vortex slice. 99

4.18 $(\mathfrak{E}/V_{tip}^2) \times 10^3$ constructed using the combinations of Fourier modes for the first $(n = 1)$ POD mode at (a) $\psi = 180°$ and (b) $\psi = 315°$ on a vortex slice. 99

4.19 Total resolved turbulence kinetic energy (Ξ) normalized with the total resolved kinetic energy (χ) of the flow. Contributions from the axisymmetric ($m = 0$), helical ($m = 1$) and double helical ($m = 2$) modes for the first ($n = 1$) POD mode relative to the mean kinetic energy (χ) of the flow also indicated. . . . 100

4.20 Fourier energy spectrum: $m = 0$, 1, and 2 for the second POD mode ($n = 2$). 102

4.21 Contours of the real component of the axial vorticity of the helical mode $(m, n) = (1, 2)$ at $\psi = 45° - 495°$. Circles of mean core-radius (|) and peak TKE (....) are indicated. 103

4.22 Contours of the real component of the axial vorticity of the helical mode $(m, n) = (1, 2)$ at $\psi = 45° - 495°$. Circles of mean core-radius (|) and peak TKE (....) are indicated. 104

5.1 Energy spectra of the first ten POD modes of the snapshot technique at (a) $\psi = 45°$ and (b) $\psi = 315°$. 106

5.2 Mode shapes of the snapshot POD alongside their counterparts of the classical POD at $\psi = 45°$: (top) radial profile of circulation; (top & bottom) axial vorticity contours. τ_1: mean core-boundary, τ_2: locations of peak TKE, τ_3: mean core-radius, τ_4: mean location of peak TKE. 107

5.3 Mode shapes of the snapshot POD alongside their counterparts of the classical POD at $\psi = 315°$: (top & middle) axial vorticity contours; (bottom) radial profile of circulation. τ_1: mean core-boundary, τ_2: locations of peak TKE, τ_3: mean core-radius, τ_4: mean location of peak TKE. 109

5.4 Continued on next page and caption provided at the end of the figure. 111

5.4 Continued on next page and caption provided at the end of the figure. 112

5.4 Axial vorticity of the most unstable mode of elliptic instability, from (a) snapshot POD and (b) classical POD: (real component) helical mode $(m, n) = (1, 1)$, at $\psi = 45° - 495°$. τ_1: mean core-boundary, τ_2: locations of peak TKE, τ_3: mean core-radius, τ_4: mean location of peak TKE. 113

5.5 Resolved energy comparisons between (a) the axisymmetric mode $(m, n) = (0, 1)$ (classical POD) and its counterpart of the snapshot POD, (b) the helical mode $(m, n) = (1, 1)$ (classical POD) and its counterpart of the snapshot POD. 114

5.6 Turbulence kinetic energy per unit mass, $(\mathrm{TKE}/V_{tip}^2) \times 10^3$, at (a) $\psi = 180°$ and (b) $\psi = 315°$. Mean vortex core boundary identified by the locations of peak swirl velocity ($V_{\Theta,max}$) also identified. 116

5.7 Low-dimensional turbulence kinetic energy per unit mass, $\mathfrak{E}/V_{tip}^2 \times 10^3$, at $\psi = 180°$ and 315°. Slice ϵ at each vortex age corresponds to the slice drawn in figure 5.6 for the respective vortex age. Mean vortex core boundary identified by the locations of peak swirl velocity ($V_{\Theta,max}$) also identified. 117

5.8 Low-dimensional turbulence kinetic energy per unit mass, $\mathfrak{E}/V_{tip}^2 \times 10^3$, on a vortex slice ϵ in figure 5.7 at $\psi = 180°$ and 315°. Actual TKE on the vortex slice also indicated. 118

5.9 Low-dimensional turbulence kinetic energy per unit mass, $\mathfrak{E}/V_{tip}^2 \times 10^3$, at $\psi = 180°$ and 315°. Slice ϵ at each vortex age corresponds to the slice drawn in figure 5.6 for the respective vortex age. Mean vortex core boundary identified by the locations of peak swirl velocity ($V_{\Theta,max}$) also identified. 119

5.10 Low-dimensional turbulence kinetic energy per unit mass, $\mathfrak{E}/V_{tip}^2 \times 10^3$, on a vortex slice ϵ in figure 5.7 at $\psi = 180°$ and 315°. Actual TKE on the vortex slice also indicated. 120

5.11 Low-dimensional turbulence kinetic energy per unit mass, $\mathfrak{E}/V_{tip}^2 \times 10^3$, at $\psi = 180°$ and 315°. Slice ϵ at each vortex age corresponds to the slice drawn in figure 5.6 for the respective vortex age. Mean vortex core boundary identified by the locations of peak swirl velocity ($V_{\Theta,max}$) also identified. 121

5.12 Low-dimensional turbulence kinetic energy per unit mass, $\mathfrak{E}/V_{tip}^2 \times 10^3$, on a vortex slice ϵ in figure 5.7 at $\psi = 180°$ and 315°. Actual TKE on the vortex slice also indicated. 122

6.1 Sample instantaneous vector maps with centers identified by the Γ_1 ($\circ$) and GC ($\star$) methods at (a) $\psi = 45°$ and (b) $\psi = 315°$. Instantaneous vortex core boundaries are also identified. . . . 124

6.2 Mean core-radius trends in the current study using the two vortex centering techniques: Γ_1 and GC methods. 125

6.3 Mean axial vorticity (ω_z/Ω) using (a) Γ_1 approach and (b) GC method at $\psi = 180°$ and 315°. Locations of peak swirl velocity ($V_{\Theta,max}$), which define the mean core-boundary, also identified. 126

6.4 Mean axial vorticity ($-\omega_z/\Omega$) at (a) $\psi = 180°$ and (b) $\psi = 315°$ on a vortex slice through the vortex center. 127

6.5 Turbulence kinetic energy per unit mass, (TKE/V_{tip}^2)×10^3, using (a) the Γ_1 approach and (b) the GC technique at $\psi = 180°$ and 315°. Mean vortex core boundary identified by the locations of peak swirl velocity ($V_{\Theta,max}$) also identified. 128

6.6 Swirl velocity, ($|V_\Theta|/V_{tip}$) × 20 ($\bigtriangledown$), and (TKE/V_{tip}^2) × 10^3 ($\star$) at (a) $\psi = 180°$ and (b) $\psi = 315°$ on a vortex slice. Vortex core boundary identified by peak swirl velocity also indicated. . . . 129

6.7 Total resolved turbulence kinetic energy (Ξ) normalized with the total resolved kinetic energy (χ) of the flow. 130

6.8 (a) Energy spectra of the first seven POD modes. (b) Energy spectra of the POD modes on a logarithmic scale. 131

6.9 Fourier mode energy spectra associated with the first ($n = 1$) POD mode. 133

6.10 Fourier energy spectra associated with the first POD mode on a logarithmic scale. 133

6.11 Radial profile (in normalized form) of the resolved energy (per unit mass) of the first three ($m = 0$ to 2) Fourier-azimuthal modes associated with the first ($n = 1$) POD mode at (a) $\psi = 45°$ and (b) $\psi = 315°$ using the Γ_1 (filled symbols) and GC (open symbols) methods. Mean core radius using the Γ_1 (solid line) and GC (dashed line) methods also identified. 135

6.12 Radial profiles of circulation ($\square$) for $(m, n) = (0, 1)$ at (a) $\psi = 45°$ and (b) $\psi = 315°$. 136

6.13 Continued on next page and caption provided at the end of the figure. 138

6.13 Continued on next page and caption provided at the end of the figure. 139

6.13 Contours of the real component of the axial vorticity of the helical mode $(m, n) = (1, 1)$ at $\psi = 45° - 495°$. Circles of mean core-radius ($\mathbb{I}$) are indicated. 140

6.14 Continued on next page and caption provided at the end of the figure. 141

6.14 Continued on next page and caption provided at the end of the figure. 142

6.14 Contours of the real component of the axial vorticity of the helical mode $(m, n) = (2, 1)$ at $\psi = 45° - 495°$. Circles of mean core-radius ($\mathbb{I}$) are indicated. 143

6.15 Continued on next page and caption provided at the end of the figure. 146

6.15 Continued on next page and caption provided at the end of the figure. 147
6.15 Radial profiles (in normalized form) of the resolved energy (per unit mass) of $m = 3$ to 25 associated with the first ($n = 1$) POD mode at $\psi = 45° - 495°$ using (a) Γ_1 and (b) GC methods. 148
6.16 Continued on next page and caption provided at the end of the figure. 149
6.16 Contours of the real component of the axial vorticity of the higher Fourier modes ($m = 3$ to 8) associated with $n = 1$ at $\psi = 315°$ using (a) Γ_1 and (b) GC methods. Circles of mean core-radius (l) are indicated. 150

Chapter 1

Introduction

Understanding the aerodynamics of helicopters is essential to improving their performance and efficiency. Helicopter rotor wakes are three-dimensional, inherently unsteady, and are dominated by spiraling vortex filaments that emanate from the blade tips. Unlike fixed-wing aircraft, where vortices from the wing tips sweep away, vortices from a rotor blade tip remain in close proximity to other blades thereby inducing highly unsteady air loads, significant blade vibrations, and heavy noise [97]. While helicopters have certain advantages relative to fixed wing aircraft (access to remote locations, an ability to take off and land in small areas as well as their ability to hover), their tip vortices can be highly energetic and have been shown to suspend sand particulate from the ground in the air, thereby causing visibility restriction to the pilot. These tip vortices also interact with other components of the helicopter such as the fuselage and tail rotor assembly, thereby elevating cabin noise and vehicle drag (resulting in power loss). Overall, tip vortices play a

This chapter may compose material from the author's previously published article, S. M. Mula, J. H. Stephenson, C. E. Tinney and J. Sirohi. Dynamical characteristics of the tip vortex from a four-bladed rotor in hover. *Exp. Fluids*, 54, 1600, 2013. For this project, Stephenson built the rotor test stand while Tinney and Sirohi served as the project advisors.

pivotal role in the performance of a helicopter and hence, a comprehensive understanding of their characteristics is warranted. The current study aims to better understand the aerodynamics of these rotor tip vortices in terms of their stability and turbulence characteristics. Unfortunately, the scarcity of experimental studies concerning the stability and turbulence characteristics of such spiraling vortex filaments leaves many questions unanswered. In order to fill this void, a quantitative experimental study coupled with unique analysis techniques is performed here on a reduced-scale rotor in hover. What makes this study so unique is the low-dimensional analysis of the vortex filament, which reveals, for the first time, the various constituents that make up the vortex filament produced by a rotor in hover.

This chapter begins by reviewing topics related to the stability and turbulence characteristics associated with trailing vortex flows. An introduction to the dynamics of trailing vortices is provided in § 1.1 and § 1.2 in the context of fixed-wing aircraft and helicopter rotors, respectively. The turbulence properties of trailing vortices are reviewed in § 1.2.1 followed by a review on their stability in § 1.3. The chapter ends with a concluding section in § 1.4, which discusses the scope of the current study, followed by an outline of subsequent chapters of this manuscript in § 1.5.

1.1 Fixed-wing aircraft trailing vortices

Trailing vortices are the most energetic structures in the wake of a fixed-wing aircraft. During landing or take off, trailing vortices can form tornado-

like structures capable of endangering nearby lighter aircraft. Such a threat requires that there be sufficient spacing between aircraft during landing and take off operations; this spacing depends on how long the danger persists, which in turn depends on how fast the vortices diffuse. These vortices do not decay merely by simple diffusion but are subject to instabilities, which can eventually breakdown the vortex [46]. Likewise, trailing vortices in the case of a helicopter rotor wake can breakdown under the influence of instabilities and turbulence that are inherent to the rotor wake.

1.2 Helicopter rotor trailing vortices

Even during the initial roll-up of a vortex sheet, which emanates from the rotor blade, the tip vortex interacts with counter-rotating flow structures [26] that reside inside the trailed sheet, as shown by the measurements of Ramasamy *et al.* (2009b) [75] in figure 1.1. The vortices that form from the blade tips of rotorcraft form compact filaments, which are helical in geometry unlike the straight-line vortex filaments in the case of fixed-wing aircraft. These vortex filaments are dynamic in nature due to the inherent unsteadiness present in the rotor wake. The dynamical nature is also evident in terms of the perturbations in the locations of these trailing vortex filaments. For instance, figure 1.2 (taken from Mula *et al.* (2013) [64]) shows the scatter in the instantaneous locations of a vortex filament on a plane perpendicular to its filament axis. This scatter is shown at sample vortex ages (100°, 130° and 160°), where a vortex age is an angular position on the vortex filament (in

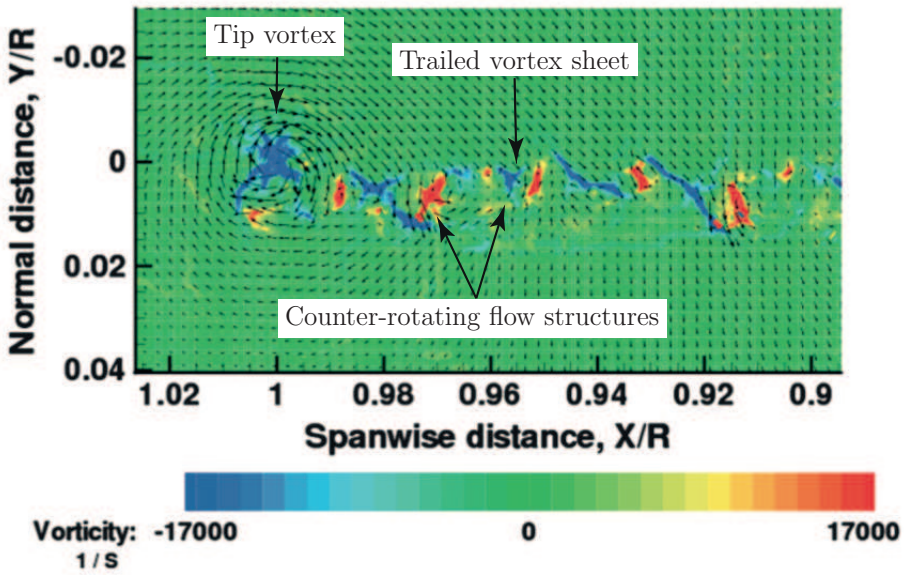

Figure 1.1: Counter-rotating flow structures in the trailed vortex sheet taken from the measurements of Ramasamy *et al.* (2009b) [75].

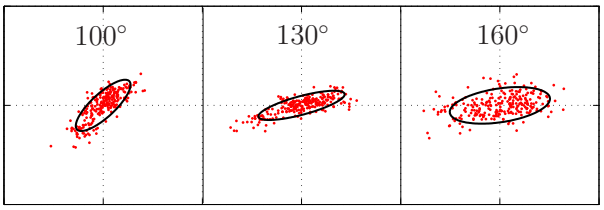

Figure 1.2: Scatter plot of vortex position at sample vortex ages taken from Mula *et al.* (2013) [64].

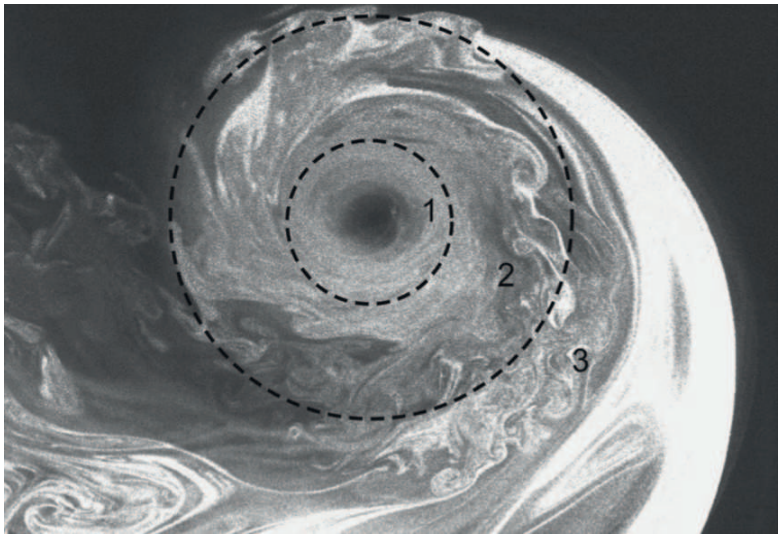

Figure 1.3: Structure of a trailing vortex taken from Ramasamy *et al.* (2009b) [75] highlighting (1) the laminar inner region, (2) an intermediate transitional region and, (3) the outer turbulent region.

rotor azimuth) relative to the blade from which the filament originates. Such perturbations (in figure 1.2) in the position of the vortex filament give rise to three-dimensional instabilities that travel along the filament axis, as described by Widnall (1972) [94], Bhagwat *et al.* (2000a) [9], Ohanian *et al.* (2012) [66] and Leweke *et al* (2014) [48] (detailed here in § 1.3.3).

1.2.1 Turbulence in the vortex

Consider a transverse cross-section (a plane perpendicular to the filament axis) of a blade tip vortex filament as shown in figure 1.3 (excerpted from Ramasamy *et al.* (2009b) [75]). The figure reveals three distinct regions inside the vortex [73, 75]: a laminar inner region, a second intermediate

region that is intermittently transitional (comprising coherent eddies of various scales), and an outer region that is turbulent (comprising less coherent eddies). Studies of Huffaker *et al.* (1970) [32], Garodz (1971) [21], Ragab & Sreedhar (1995) [70], Zeman (1995) [98] and Devenport *et al.* (1996) [16] suggest that the vortex core is laminar. However, high velocity fluctuations have been found inside the vortex core (by Phillips & Graham (1984) [68], Bandyopadhyay *et al.* (1991) [4], Devenport *et al.* (1996) [16], Han *et al.* (1997) [27], Ramasamy *et al.* (2009b) [75], and Beresh *et al.* (2010) [7]) which extend up to two core-radii from the center of the vortex [27, 75]. Some of the discrepancies are attributed to the difficulties associated with developing a universally adopted method for correcting for vortex wander. Devenport *et al.* (1996) [16] suggests that the fluctuations within the vortex core are a result of inactive motions produced by the turbulence in the outer wake surrounding the core. Whereas, Bandhyopadhyay *et al.* (1991) [4] points out that the vortex core comprises intermittent patches of turbulent and relaminarized fluid due to the intermittent exchange of momentum (by organized motions) between the outer turbulent region and the vortex core. Nevertheless, if the vortex core is merely laminar, the presence of high velocity fluctuations should suggest the presence of instabilities within the vortex [7]. However, there are limited quantitative experimental studies on the helicopter vortex filaments that actually explore the stability and turbulence characteristics owing to the complicated geometry associated with these unsteady vortex filaments.

1.3 Vortex instabilities

Helical vortex filaments in an inviscid fluid (such as the case of helicopter vortex filaments) are always unstable [9]. This is certainly true for circular vortex filaments [95]. For instance, if an ideally straight vortex filament is considered, the filament is supposedly very stable. As another straight filament is brought in close vicinity and parallel to the first filament, both the filaments are likely to undergo instabilities [15]. This is due to a strain induced on each filament by the other. In the case of a helical vortex filament, strain is inherently induced by three mechanisms: (1) the proximity of the vortex to neighboring vortices, (2) curvature of the vortex filament, and (3) torsion [20].

When a vortex filament is subject to external strain it is likely to undergo three-dimensional instabilities such as long-wave and short-wave instabilities that travel along the vortex filament [15, 61, 94–96]. As visualized by Crow (1970) [15] and Leweke & Williamson (1998, 2011) [46, 47], in the limit of small perturbations (linear regime) these waves are sinusoidal in their behavior. For instance in figure 1.4, taken from the flow visualization study by Leweke & Williamson (1998) [46], sinusoidal long-wave and short-wave perturbations are shown on two counter-rotating straight-line vortex filaments under the influence of strain induced on each filament by the other. The most unstable long-waves are those whereby the two filaments mutually perturb out-of-phase with respect to each other in their plane of separation, as shown in figure 1.4. Such a long-wave instability, as it was first introduced by Crow (1970) [15], is called Crow instability that comprises wavelengths

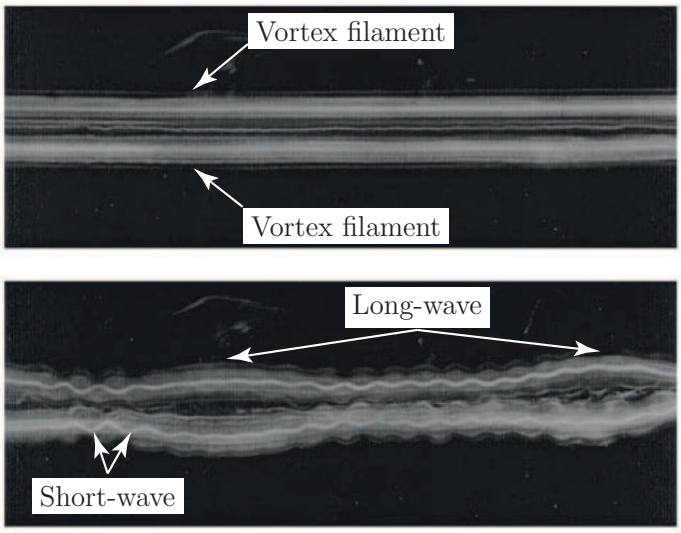

Figure 1.4: Long-wave and short-wave instabilities taken from the flow-visualization study of Leweke & Williamson (1998) [46].

on the order of about eight vortex spacings[1]. Further, the filaments are also unstable to short-waves whose wavelength is on the order of the filament core-radius [46, 61, 96]. Figure 1.5 shows a close-up view of a short-wave instability where the centerline of the vortex core mutually perturbs out-of-phase with respect to its edges; the instability modifies the structure of the vortex core [46]. Such a short wave instability is called an elliptic instability, which was theoretically discovered by Moore & Saffman (1975) [61], Tsai & Widnall (1976) and numerically demonstrated by Robinson & Saffman (1984) [78], Pierrehumbert (1986) [67] and Bayly (1986) [6]. An elliptic instability occurs in a vortex which is elliptically deformed under the influence of strain [6, 67]. Unlike the

[1]Vortex spacing here is defined as the separation distance between the two straight line filaments.

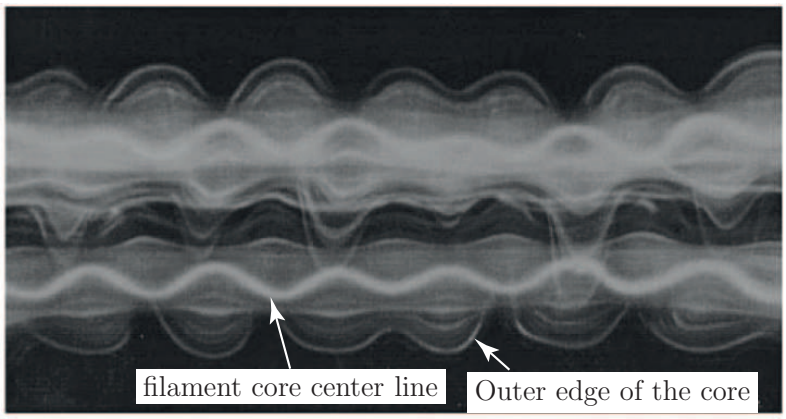

Figure 1.5: Close-up view of short-wave instabilities taken from the flow-visualization study of Leweke & Williamson (1998) [46].

Crow instability, which forms only in counter-rotating vortex filaments [35], an elliptic instability can occur even in the case of co-rotating vortices (as seen by Meunier & Leweke (2005) [60]).

1.3.1 Elliptic instability

Elliptic instability was discovered and rediscovered in a variety of flows [38]. The earliest known investigations comprise theoretical studies by Moore & Saffman (1975) [61] and Tsai & Widnall (1976) [87] who developed linear stability analysis of a finite core vortex (in an inviscid medium), with no axial flow (or with a small axial flow [61]), where the vortex was slightly deformed elliptically by the presence of weak strain. Subsequent numerical studies by Robinson & Saffman (1984) [78] showed that the short-wave instability (elliptic instability), which was found analytically in the presence of weak strain, continued to occur in the presence of significant strain. Following these stud-

ies, the instability was rediscovered numerically (by Pierrehumbert (1986) [67] and Bayly (1986) [6]) in an idealized, two-dimensional, unbounded, elliptically deformed vortex (in inviscid fluid medium) with finite core when subjected to three-dimensional short-wave perturbations; as for the occurrence of these elliptic instabilities, in such an inviscid flow, there was found to be no minimum threshold wavelength of these short-wave perturbations [6,67]. However, Landman & Saffman (1987) [43] later found that the presence of a non-vanishing viscosity had a stabilizing effect, thereby building a cutoff on the minimum wavelength for the development of these instabilities [43]. In the context of a bounded and strained vortex flow (with finite core), elliptic instabilities were observed in both theoretical (see Waleffe (1989) [91] and Gledzer & Ponomarev (1992) [22]) and experimental (see Leweke & Williamson [46], Vladimirov *et al.* (1987) [90] and Malkus (1989) [54]) studies. For instance, the elliptic instabilities demonstrated earlier in figures 1.4 and 1.5 actually correspond to an open flow configuration of a pair of counter-rotating vortex filaments (finite core, no axial flow), which are bounded by a rectangular cylinder [46]. Furthermore, as shown by Laceze *et al.* (2007) [41] and Roy *et al.* (2011) [79], the addition of a significant axial velocity to the vortex was found to have a profound influence on these elliptic instabilities.

In the linear regime[2], an elliptic instability occurs when one or two normal modes of the same axial wavenumber (along the vortex axis) resonate with the external strain [38, 61, 87]. In a non-axial flow situation, the most

[2]In the limit of small perturbations.

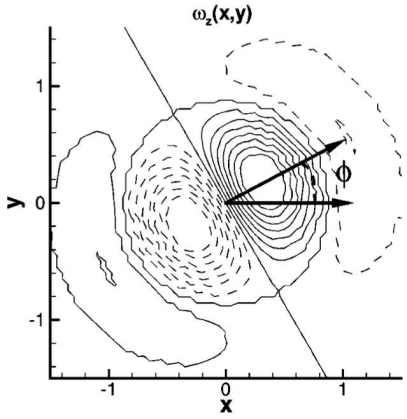

Figure 1.6: Axial vorticity field of a linear mode structure of the elliptic instability in the transverse plane as described by Sipp (2000) [82]. Solid and dashed lines indicate opposite signs of vorticity.

unstable short-waves (associated with elliptic instabilities) correspond to azimuthal mode $|m| = 1$ [61, 78]. But in a general sense (axial or non-axial flow) if the vortex is confined, the external strain always excites a pair of normal modes that correspond to azimuthal modes m and $m + 2$ [38, 41]. Therefore, once again in a non-axial flow, the most unstable waves for a bounded vortex flow correspond to azimuthal modes -1 and 1 (see Malkus (1989) [54], Gledzer & Ponomarev (1992) [22], and Leweke & Williamson [46]), which satisfy the above criteria. A sample illustration of a linear mode structure of the elliptic instability in the transverse plane of a vortex filament, constructed from the superposition of modes $m = -1$ and 1, is shown in figure 1.6 (taken from Sipp (2000) [82]). As the axial velocity increases, the corresponding most unstable azimuthal modes (of the elliptic instability) progressively change from -1 and 1 to other combinations of non-positive modes m and $m + 2$ (such as -2

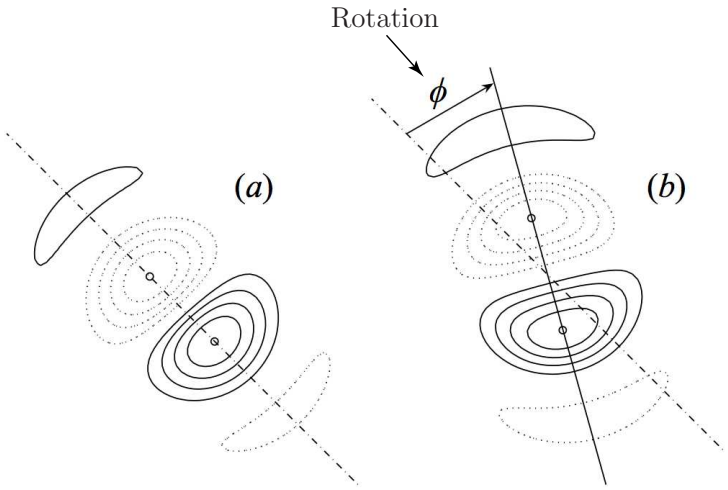

Figure 1.7: Contour plot of axial vorticity of the most unstable mode of the elliptic instability in the numerical investigations of Schaeffer & Dizer [80]. (a) Linear regime and (b) weakly non-linear regime. Solid and dashed lines correspond to positive and negative isovorticity contours respectively.

and 0, and then -3 and -1, and so on), as seen by Lacaze *et al.* (2007) [41] and Roy *et al.* (2011) [79]. Likewise, an increase in rotation rates of the mean vortex flow, which can have a stabilizing effect on the elliptic instability, can also modify the conditions on the resonance of normal modes and their corresponding azimuthal modes [14].

Non-linear aspects of the elliptic instability were also explored in strained vortex flows in the absence of axial velocities (by Waleffe (1989) [91], Sipp (2000) [82] and Schaeffer & Dizes (2010) [80]). In the limit of a weakly non-linear regime, the structure of a linear mode of the elliptic instability rotates about the vortex axis, as shown in figure 1.7 (excerpted from Schaeffer & Dizes (2010) [80]), without producing any significant modification to the structure

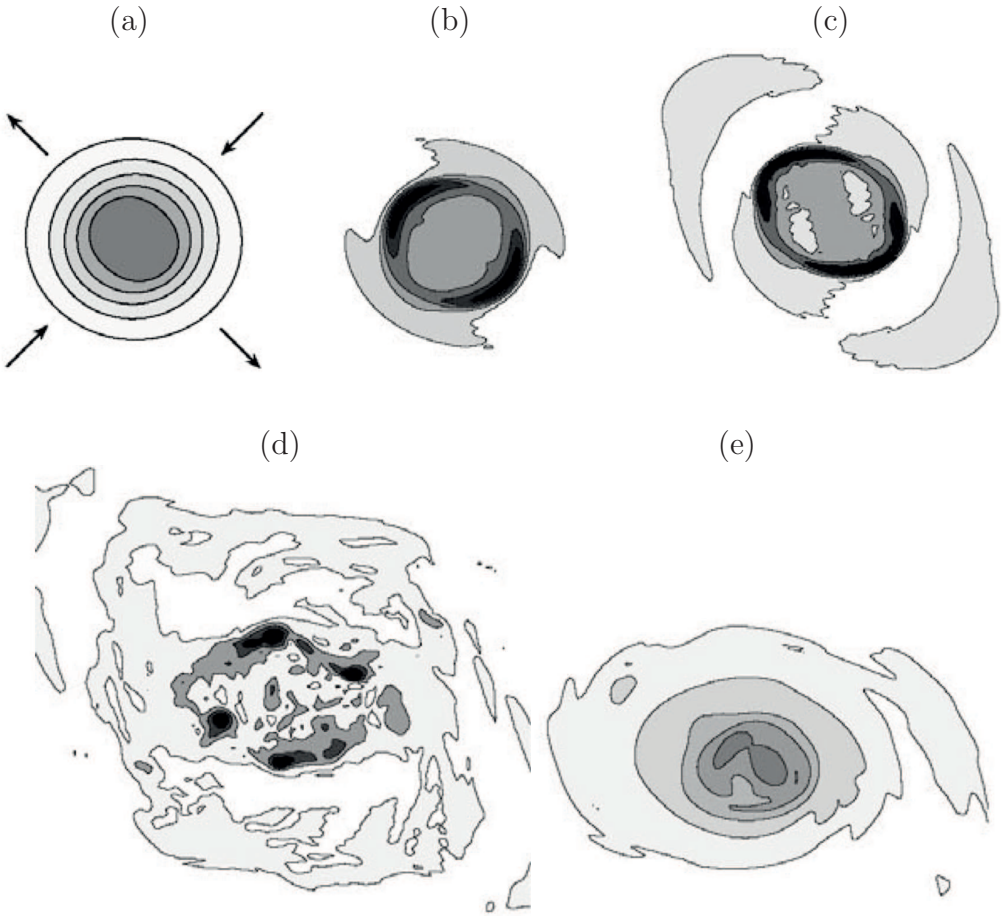

Figure 1.8: (a-e) Evolution of axially averaged vorticity contours in a plane perpendicular to the vortex axis (in strongly nonlinear regime of elliptic instability) in the numerical investigations of Schaeffer & Dizer [80].

of the mode. In this regime, as described by Waleffe (1989) [91] and Sipp (2000) [82], the instability can saturate and attenuate to return to its linear regime and repeat the process. However, in a highly non-linear regime, as shown by Schaeffer & Dizes (2010) [80], there is no saturation mechanism. While the elliptic instability grows, it also increases the size of the vortex core (see figure 1.8a-b taken from Schaeffer & Dizes (2010) [80]). However, the growth in the core radius ends when secondary vortices (figure 1.8c) form around the primary vortex. These secondary structures move away from the vortex axis, destabilize, and then break down into smaller scales by the action of viscosity (see figure 1.8d). After breakdown, the primary vortex recovers its shape through relaminarization and forms a core (figure 1.8e) comprising a much larger radius and a much lower vorticity compared to the original vortex. After recovery, the elliptic instability can again develop and repeat the process.

1.3.2 Vortex breakdown

Long-wave instabilities when present in combination with short-wave instabilities can cause vortex breakdown. Once again, consider a pair of counter-rotating straight-line vortex filaments illustrated in figure 1.4. Based on the observations of Leweke & Williamson (2011) [47], in the absence of short-wave instabilities non-linear evolution of Crow-instability forms large-scale vortex rings that can remain energetic for a very long time. However, when short-wave instabilities are also present, non-linearities in both short-

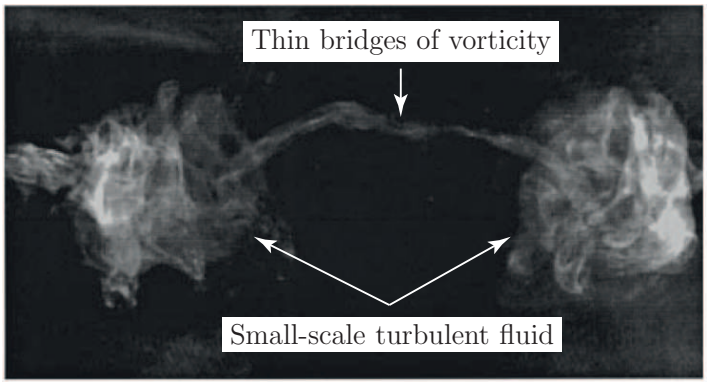

Figure 1.9: Vortex breakdown in the flow visualization study of Leweke & Williamson [47].

wave and long-wave perturbations can develop much earlier, thereby causing breakdown of large-scale coherent structures to periodic regions of disorganized turbulence which are linked by thin bridges of vorticity (see figure 1.9 taken from Leweke & Williamson (2011) [47]). These small-scale structures are less energetic when compared to the large-scale vortex rings when only the Crow instability is present. Therefore, the combined effect of both long-wave and short-wave instabilities can play a significant role in the diffusion mechanism of trailing vortices.

1.3.3 Stability investigations on spiraling vortex filaments

While earlier sections of this chapter reviewed topics concerning instabilities associated with vortex flows in a more general sense, the current section focus more specifically on the instabilities associated with spiraling vortex filaments. As stated earlier, spiraling vortex filaments are subject to

three-dimensional disturbances due to the inherent strain induced by the curvature effect; the presence of multiple vortex filaments, such as those that are produced by multi-bladed rotors, induces additional strain. The earliest known investigations (on helical filaments) comprise the linear stability studies developed by Widnall (1972) [94], which revealed an existence of three-dimensional instabilities whose wavelength was much greater than that of the filament core size. These are the so called long-wave instabilities, as per the terminology used in straight vortex filaments (see § 1.3). Sample illustrations on the growth rate of these long-wave perturbations are provided in figure 1.10, along with various mode shapes of these perturbations in figure 1.11 [94]. The first mode shape in figure 1.11, whose wavenumber is not specified, is an instability whose wavelength is much smaller than the local radius of curvature of the filament (but larger than the filament core size). Also demonstrated are the mode shapes for sample half-integer wavenumbers in figure 1.11. At these wavenumbers, the perturbations on successive turns of the helix are out-of-phase.

Complementary to the studies of Widnall (1972), Bhagwat & Leishman (2000) [9] developed numerical investigations on helical vortex filaments from single- and multi-bladed rotors in hover. The methodology developed by Bhagwat & Leishman (2000) (for stability investigations) is very general and can be applied to any rotor wake geometry. In this methodology, vortex filaments are divided into various line segments. Velocity induced from each segment (see figure 1.12) at a point, say M on a filament, is obtained using

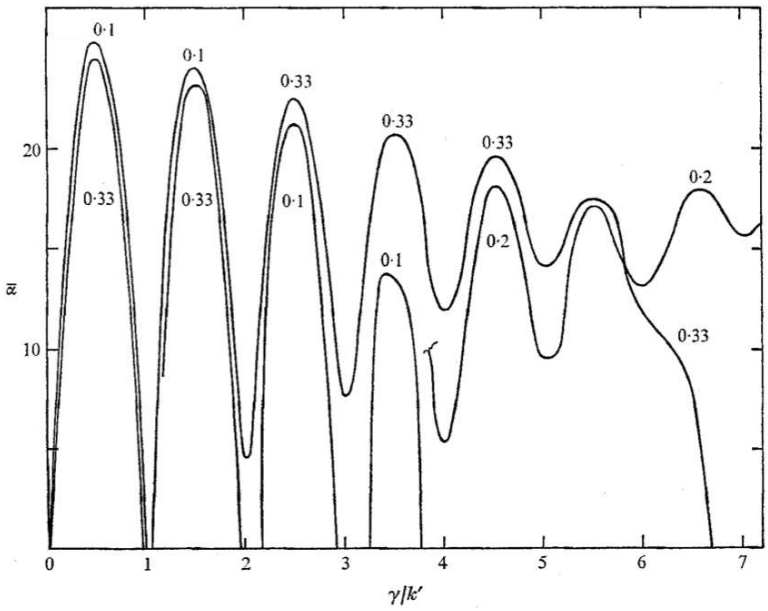

Figure 1.10: Non-dimensional amplification rate (or growth rate of perturbations) for helices at a sample pitch with an instability mode of $\gamma/k\prime$ waves per cycle (wavenumber) as found by Widnall (1972) [94]. The values of the ratio of vortex core radius to the radius of cylinder (that encloses helix) are shown on each curve [94].

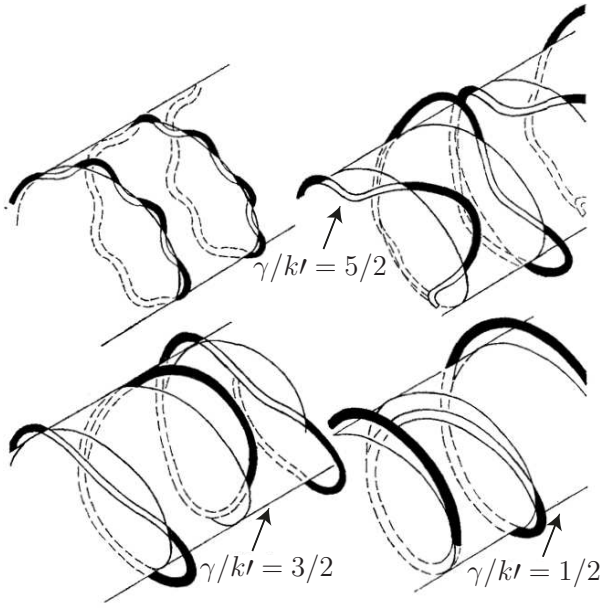

Figure 1.11: Instability mode shapes for sample wavenumbers taken from Widnall (1972) [94]. Dark portions are outside the cylinder on the near side while light portions are on the inside.

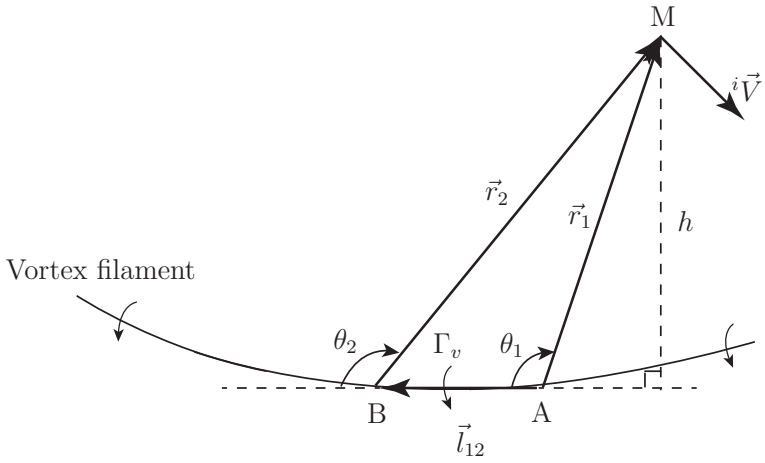

Figure 1.12: Schematic showing the velocity induced by a straight-line vortex filament AB [9]. Γ_v is the circulation strength of the vortex filament.

the Biot-Savart law,

$$\{{}^i\vec{V}\}_c = \frac{\Gamma_v}{2\pi h}\,(\cos\theta_1 - \cos\theta_2)\,\{\widehat{e}\}_c, \tag{1.1}$$

where $\{\ \}_c$ defines the vector components in cartesian system (x, y, z), ${}^i\vec{V}$ is the velocity induced at point M by the i^{th} segment and $\widehat{e}$ is the unit vector of ${}^i\vec{V}$. In order to account for singularity as $h \to 0$ in Eq. 1.1, the Biot-Savart law is modified such that it includes a viscous vortex core with an induced velocity profile,

$$V = \left(\frac{\Gamma_v}{2\pi}\right)\frac{r}{(r_c^{2n} + r^{2n})^{\frac{1}{n}}}, \tag{1.2}$$

where r is the radial distance from the vortex center and r_c is the core-radius. As $n \to 0$ Eq. 1.2 reduces to the Rankine vortex model; for $n = 1$ and $n = 2$ Eq. 1.2 represents the Scully [81] and Lamb-Oseen [42] models, respectively. Thus, for a vortex with viscous core, the Biot-Savart law is rewritten as

$$\{{}^i\vec{V}\}_c = \left(\frac{\Gamma_v}{2\pi}\right)\frac{h}{(r_c^{2n} + h^{2n})^{\frac{1}{n}}}\,(\cos\theta_1 - \cos\theta_2)\,\{\widehat{e}\}_c. \tag{1.3}$$

The equilibrium wake is then subjected to small perturbations where the perturbed induced velocity, due to each segment, is obtained as

$$\{\delta^i V\}_c = \left(\frac{\Gamma_v}{2\pi}\right)\frac{1}{(r_c^{2n} + h^{2n})^{\frac{1}{n}}}\,([A]\{\delta\vec{r}_A\}_c + [B]\{\delta\vec{r}_B\}_c + [M]\{\delta\vec{r}_M\}_c), \tag{1.4}$$

where $[A]$, $[B]$ and $[M]$ are the coefficient matrices which are in terms of the known local parameters of the line segment AB and point M in figure 1.12; $\delta\vec{r}_A$, $\delta\vec{r}_B$ and $\delta\vec{r}_M$ denote the perturbations in positions A, B and M, respectively.

Further, perturbations on vortex filaments are assumed to be in the form of traveling waves. For instance,

$$\{\delta\vec{r}_M\}_p = \{\delta\vec{r}_0\}_p e^{\alpha t + \imath\omega\psi_M}, \{\delta\vec{r}_M\}_c = [T]_M\{\delta\vec{r}_M\}_p, \tag{1.5}$$

where ψ_M is the vortex age corresponding to point M, α is the growth rate of the perturbations, ω is the wavenumber, $\{\ \}_p$ represents the vector components in the polar coordinate system (r, θ, z) and $[T]_M$ is the transformation matrix evaluated at point M between the polar and cartesian coordinates. Applying Eq. 1.5 in Eq. 1.4, one achieves the following,

$$\begin{aligned}\{\delta^i\vec{V}\}_c = \left(\frac{\Gamma_v}{2\pi}\right)\frac{1}{(r_c^{2n}+h^{2n})^{\frac{1}{n}}}\ (e^{\imath\omega(\psi_A-\psi_M)}[A] + e^{\imath\omega(\psi_B-\psi_M)}[B] \\ +[M])[T]_M\{\delta\vec{r}_0\}_p e^{\imath\omega\psi_M}, \\ = \left(\frac{\Gamma_v}{2\pi}\right)[^iC][T]_M\{\delta\vec{r}_M\}_p.\end{aligned} \tag{1.6}$$

The total perturbed induced velocity $\delta\vec{V}$, at point M, is obtained by summing together contributions from all segments of the vortex filaments.

$$\{\delta\vec{V}\}_c = \left(\frac{\Gamma_v}{2\pi}\right)\sum\nolimits_i[^iC][T]_M\{\delta\vec{r}_M\}_p = \left(\frac{\Gamma_v}{2\pi}\right)[C][T]_M\{\delta\vec{r}_M\}_p. \tag{1.7}$$

Further, the total perturbation velocity $\delta\vec{V}$ can also be obtained as,

$$\begin{aligned}\{\delta\vec{V}\}_c = \{\delta\dot{\vec{r}}_M\}_c = [T]_M\{\delta\dot{\vec{r}}_M\}_p + [\dot{T}]_M\{\delta\vec{r}_M\}_p, \\ = [\alpha[T]_M + [\dot{T}]_M]\{\delta\vec{r}_M\}_p.\end{aligned} \tag{1.8}$$

Therefore, equating Eq. 1.7 and Eq. 1.8,

$$\left(\frac{\Gamma_v}{2\pi}\right)[C][T]_M\{\delta\vec{r}_M\}_p = [\alpha[T]_M + [\dot{T}]_M]\{\delta\vec{r}_M\}_p, \tag{1.9}$$

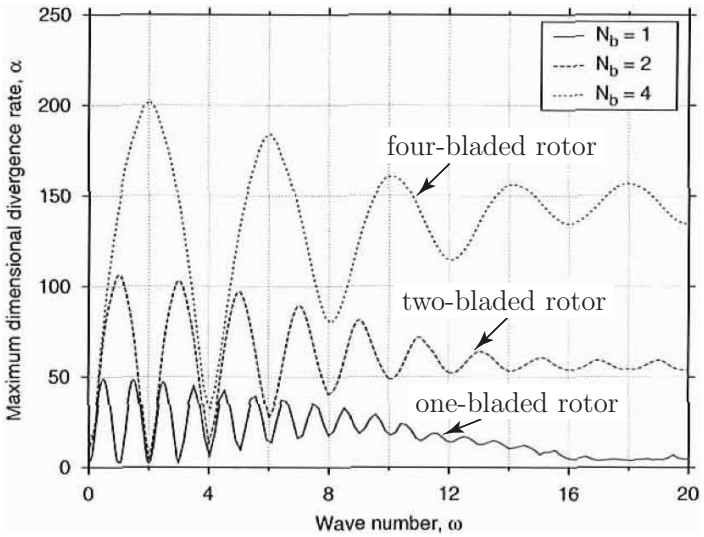

Figure 1.13: Maximum divergence rates (or growth rate of perturbations) for the one-, two-, and four-bladed hovering rotors at constant blade-loading, $C_T/\sigma = 0.075$, from the numerical studies of Bhagwat & Leishman (2000) [9].

reduces to a standard eigenvalue problem,

$$\alpha\{\delta\vec{r}_M\}_p = [\left(\frac{\Gamma_v}{2\pi}\right)[C] - [\dot{T}]_M[T]^{-1}]\{\delta\vec{r}_M\}_p. \tag{1.10}$$

Once again, α is the growth rate of perturbations in the wake. By applying this methodology to hovering rotor wakes, Bhagwat & Leishman (2000) [9] showed that the growth rates of perturbations were positive for all wavenumbers of long-waves (see figure 1.13). This indicates that the rotor tip vortex filaments are always unstable. Also, their findings in figure 1.13 show that the most unstable long-waves occur at wavenumbers of half-integer multiples of the number of blades (N_b). Similar results can be seen in the findings of Widnall (1972) [94] in figure 1.10. At these wavenumbers, successive filaments from rotor blades mutually perturb out-of-phase, which complement the findings

in figure 1.11 [94] (see at $\omega = 1/2, 3/2$ & $5/2$). However, at wavenumbers of integer multiples of N_b long-wave perturbations are least unstable. Also, at these wavenumbers, successive filaments from rotor blades mutually perturb in-phase.

Pitch (mm)	Radius of helix, R (mm)	r_c (mm)
146	500	4.97

Table 1.1: Parameters of the helical vortex filament studied here.

The methodology described in Eq. 1.1 to Eq. 1.10 can also be applied to intertwining helical vortex filaments in a more general sense. For instance, consider helical filament(s) with constant parameters: pitch, cylindrical radius and core-radius defined in table 1.1. The parameters in this table are actually estimates of the initial pitch and cylindrical radius of the helix measured in the current study, while the estimate of core-radius (r_c) is obtained at the earliest vortex age ($\psi = 45°$) in the measurement envelope. The resultant non-dimensional growth rates of perturbations ($\bar{\alpha} = \alpha/\Gamma_v/2\pi R^2$) on single- and multiple-intertwining helical vortex filaments are demonstrated in figure 1.14, which qualitatively resembles the findings (on most unstable and least unstable long-waves) of rotor tip vortex filaments in figure 1.13.

As for the flow-visualization studies, three-dimensional long-wave instabilities were identified by Ohanian *et. al* (2012) [66] on vortex filaments produced by a three-bladed rotor in hover. As shown in figure 1.15 for a sample rotation rate [66], the wavelength of these long-waves appears to be

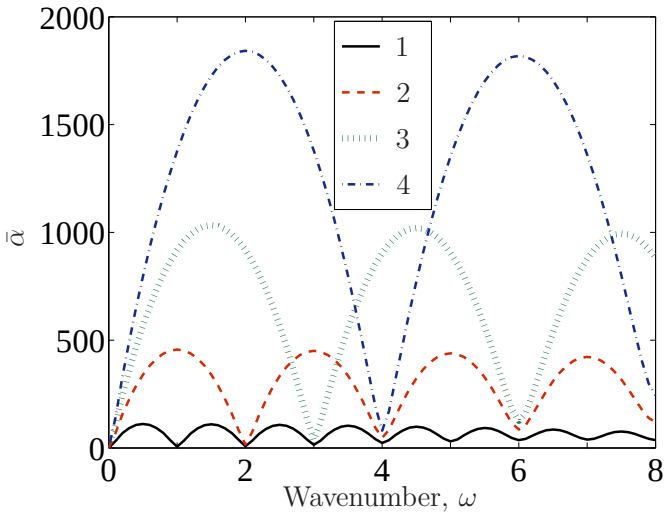

Figure 1.14: Maximum non-dimensional divergence rates (or growth rate of perturbations) for one-, two-, three- and four-intertwining helical vortex filaments.

much smaller than the local radius of curvature of the filament, but much larger than the size of the filament core. Traces of short-wave instabilities (as per the terminology used in § 1.3), whose wavelength is on the order of core-radius, were also observed on these filaments at a different rotation rate (see figure 1.16). Complementary to these observations, recent flow-visualization studies by Leweke *et al.* (2014) [48] also demonstrated the existence of such short-wave instabilities on filaments from a horizontal wind turbine wake. A sample illustration of these short-wave instabilities in the wake of a single-bladed wind turbine is shown in figure 1.17. The simultaneous development of long-wave instabilities, at which the perturbations on successive turns of the helix are out-of-phase, can also be seen in the far wake of the rotor. These

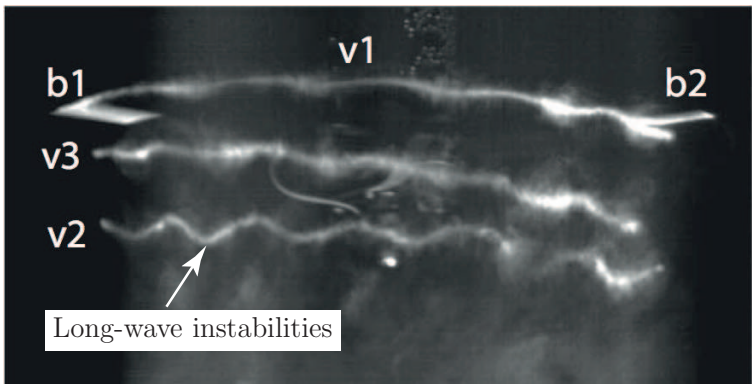

Figure 1.15: Instabilities on rotor-tip vortex filaments of a three-bladed rotor (at 4 revolutions per second) in hover in the flow visualization study of Ohanian *et al.* (2012) [66]. b1-blade 1, b2-blade 2, b3-blade 3; v1, v2, v3 represent vortex filaments from blades 1, 2, and 3, respectively.

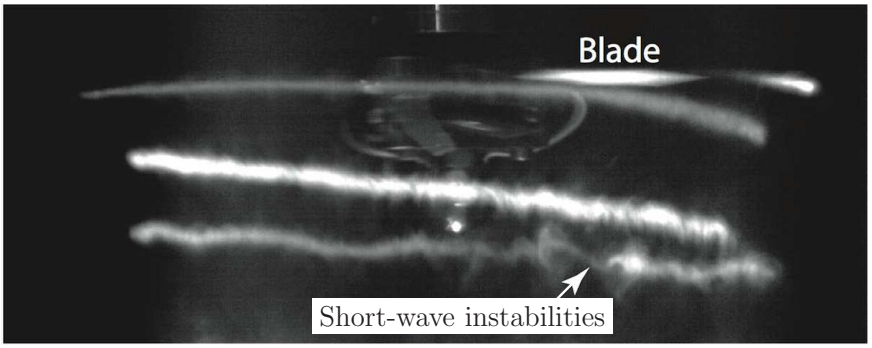

Figure 1.16: Traces of short-wave instabilities on rotor-tip vortex filaments of a three-bladed rotor (at 8 revolutions per second) in hover in the flow visualization study of Ohanian *et al.* (2012) [66].

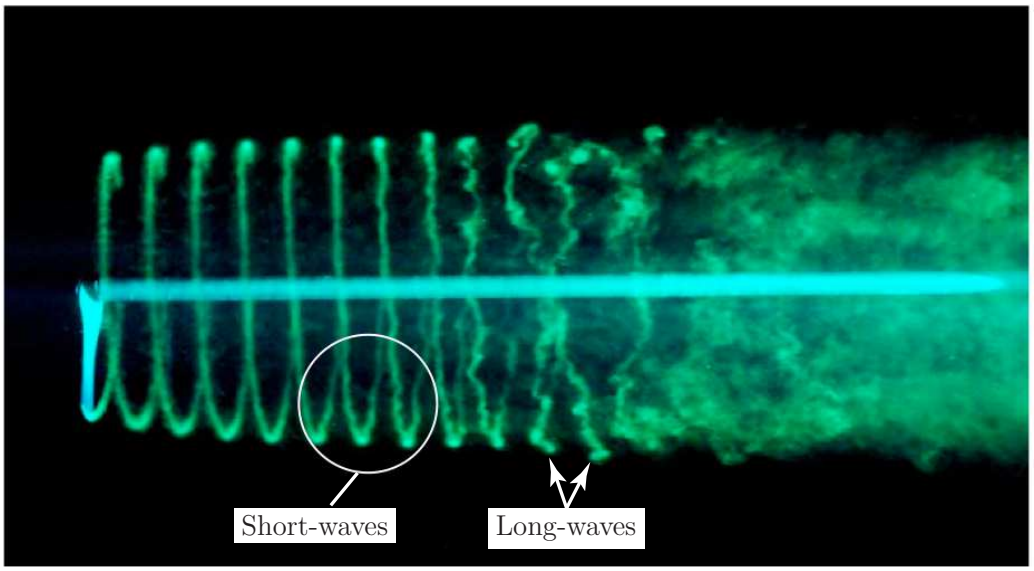

Figure 1.17: Short-wave and Long-wave instabilities on tip vortex filaments from a horizontal axis one-bladed wind turbine taken from Leweke *et al.* (2014) [48].

findings suggest that the simultaneous presence of such long-waves and short-waves lead to a rapid breakdown of the tip vortices. Similar conclusions were drawn earlier in the case of straight vortex filaments (see § 1.3.2).

In addition to the above analytical, numerical and flow-visualization studies, quantitative experimental investigations were also carried out on helical vortex filaments. This involved performing stereoscopic PIV experiments on a four-bladed rotor in hover by Mula *et al.* (2013) [64]. Long-wave perturbations in the instantaneous positions of a vortex filament $(x\star, y\star)$ on a plane perpendicular to the filament axis were captured using different vortex center identification techniques: CoQ [33, 89], normalized helicity [44, 45, 88], centroid of vorticity, Γ_1 [24], and a geometric centering approach. All of these

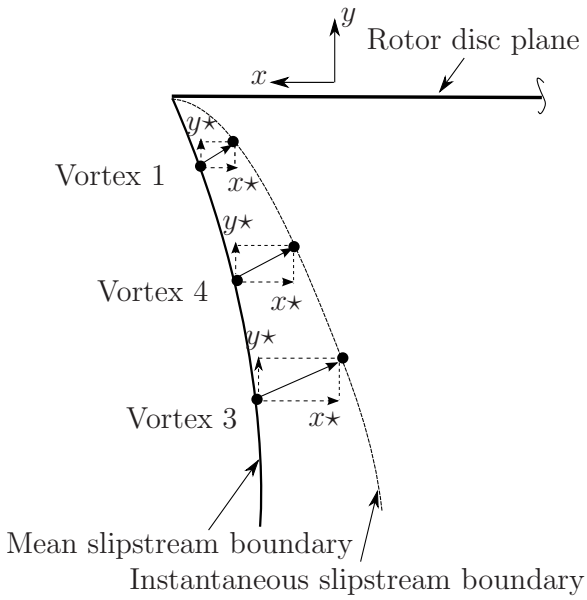

Figure 1.18: Schematic of vortex wander and coordinate system (for in-plane motions) with respect to the mean slipstream boundary provided by Mula *et al.* (2013) [64]. Vortices 1, 2, 3, and 4 represent tip vortices from blades 1, 2, 3, and 4, respectively.

techniques (detailed in § 3) produced similar results, where vortex wander on a plane perpendicular to the vortex axis is concerned. A schematic of wander, for filaments from the four-bladed rotor, is shown in figure 1.18. For the range of vortex ages studied: $\psi = 10° - 260°$, figure 1.19 illustrates vortex wander with a 95% confidence interval. At each ψ, the wander is anisotropic. The amount of wander increases with the increase in vortex age, and, the preferred direction of wander rotates with the increasing vortex age. Furthermore, in order to obtain the relative in-plane motion between vortices from different rotor blades (see figure 1.18), the perturbations of each vortex $(x\star, y\star)$ are normalized with the standard deviation $(\boldsymbol{\sigma}_x, \boldsymbol{\sigma}_y)$ of the corresponding com-

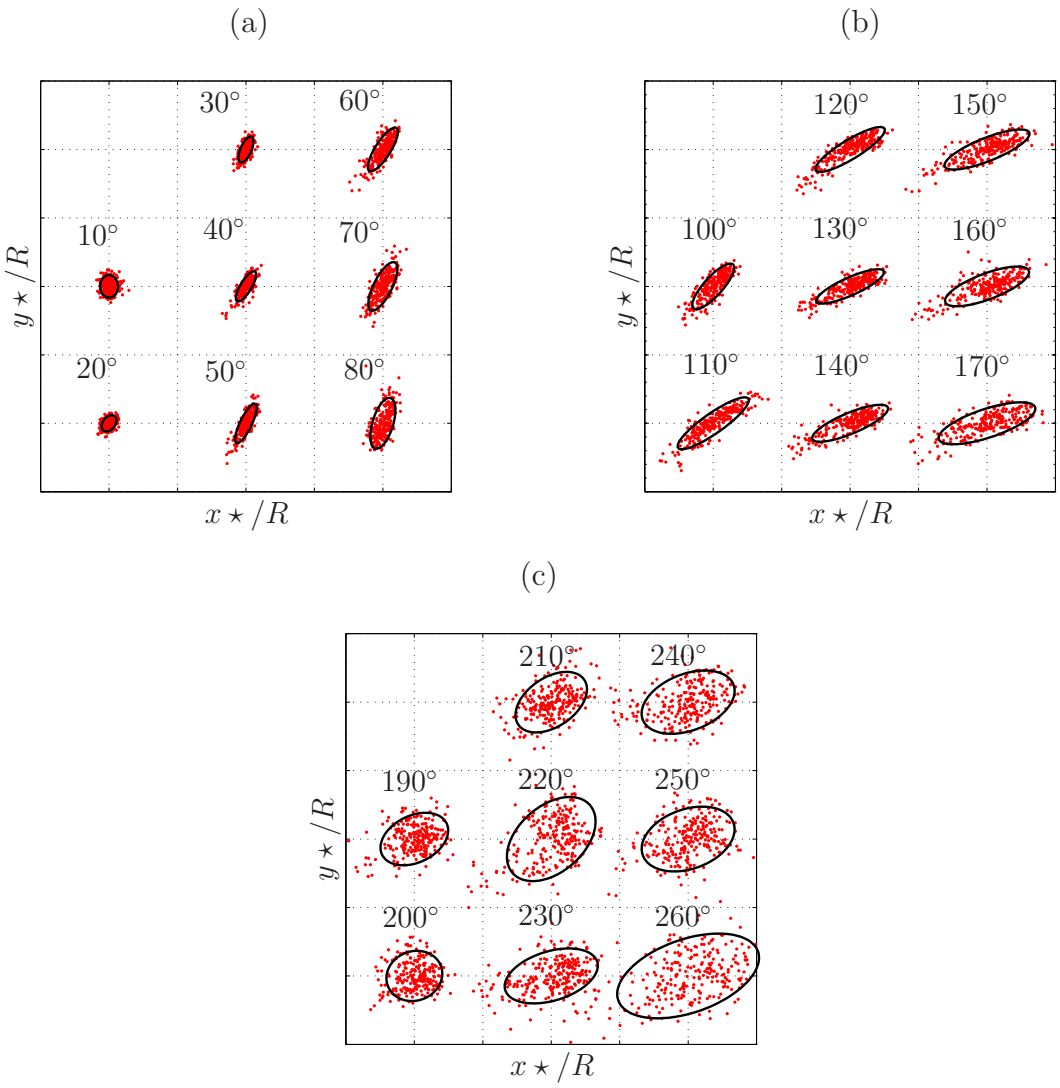

Figure 1.19: Wander of vortex from blade 2 overlaid the 95% confidence region for vortex ages between (a) 10° - 80°, (b) 100° - 170°, (c) 190° - 260° using CoQ in the measurements of Mula *et al.* (2013) [64]. Dashed lines are separated by $y\star/R = 0.03$; $x\star/R = 0.03$.

ponent. Such a normalization is done in order to eliminate the amplitude dependence brought by the spatial growth in wander with the increase in vortex age. Figure 1.20a, b illustrates the normalized instantaneous perturbations in two perpendicular directions, for vortex 4 with vortex 3 (see figure 1.18 for vortex notations) at different azimuthal positions (in rotor azimuth): $10° - 80°$. Once again, a 95% confidence ellipse is constructed which identifies a preferred direction of orientation inclined at 45° to the horizontal axis in figure 1.20a, b at all azimuthal positions. Similar findings were observed between vortices 1 and 4, and vortices 1 and 3 (demonstrated in Mula *et al.* (2012) [63]). Hence, from figure 1.20, all the vortices in figure 1.18 wandered predominantly in-phase in every direction, which suggests the dominance of long-waves with wavenumbers of integer multiples of the number of blades in the measurement envelope (as described by Bhagwat & Leishman (2000a) [9]).

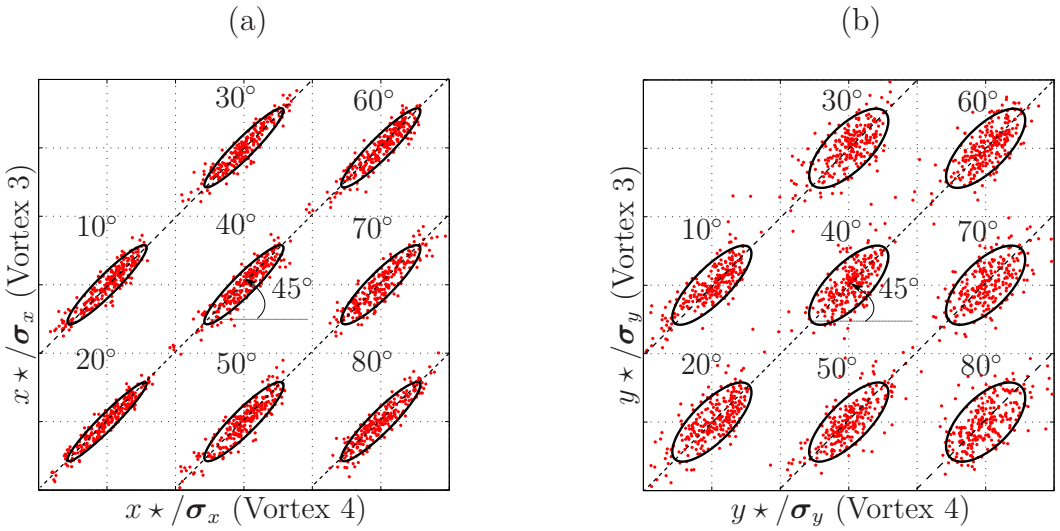

Figure 1.20: Phase motion of the (a) $x\star$ and (b) $y\star$ displacements in figure 1.18 between vortex 4 and vortex 3 using CoQ in the measurements of Mula *et al.* (2013) [64]. The 95% confidence interval region has been drawn. Dashed lines are separated by $y\star/\boldsymbol{\sigma}_y = 3$; $x\star/\boldsymbol{\sigma}_x = 3$.

1.4 Scope of the current research

As there are a limited number of quantitative experimental studies characterizing the behavior of short-wave instabilities on spiraling vortex filaments, the objective of the current study is to better understand these instabilities as well as the organized turbulence that reside within the vortex produced by a rotor blade in hover using Particle Image Velocimetry (PIV). The vortex studied here is formed by a single-bladed rotor; the advantages of such a configuration guarantees no interference from instabilities formed by the presence of other vortex filaments in a multi-bladed rotor [55, 75]. Corrections for vortex wander are performed using the Γ_1 method [24], which is an integral based

approach. Therefore, the results are not corrupted by the noise introduced by the gradients of the velocity field. The Proper Orthogonal Decomposition (POD) technique [53] is used to flush out the more energetic flow features responsible for characterizing the bulk motions of the tip vortex and is performed over extended vortex ages. The current study is complementary to the one conducted by Roy *et al.* (2011) [79], who used dye images to determine the low-order features associated with tip vortices from a fixed-wing. Furthermore, Lumley's POD technique is implemented using two different forms. That is, the classical and snapshot [83] forms. While the classical form of POD, described by Glauser (1987) [23], Citrinity & George (2000) [13] and Tinney *et al.* (2008) [85], provides an easier interpretation of the low-order features, the snapshot form [83] is computationally more efficient when using spatially resolved PIV data. And so, both these forms of POD are applied to spiraling vortex filaments in the current study and subsequently compared. In addition, a sensitivity study is also developed on the choice of the vortex centering technique to the low-dimensional features (of the tip vortex) obtained by way of POD.

1.5 Outline of subsequent chapters

Details of the experimental setup, test conditions, and measurement uncertainties are provided in § 2. In § 3, details of some basic characteristics of tip vortices from the experimental measurements, as well as comparisons with the studies reported in the open literature, are provided. This is done

in an effort to provide confidence in the measurements reported here as the statistical properties of the spiraling vortex filament have been studied extensively over the past several decades. This is followed by a description of the classical and snapshot forms of the proper orthogonal decomposition (POD) technique. Low-dimensional characteristics of the spiraling vortex filament using the classical form of POD are demonstrated in § 4, with subsequent comparisons between the classical and snapshot forms of POD (applied to the helical filament) being provided in § 5. Following this, a sensitivity study on the choice of the vortex centering approach to the low-dimensional features obtained by POD is demonstrated in § 6. A summary of the important conclusions, along with a direction of future work, is then provided in § 7.

Chapter 2

Experimental setup

The motivation for conducting this study is to characterize the turbulence and wandering motion of a vortex filament from a single bladed rotor in hover. One could use simulated data for such an analysis, but one is confined to Reynolds number effects (in the case of DNS) or validation and grid resolution issues (in the case of LES). In what follows, details of the rotor test stand and experimental conditions are provided in § 2.1, followed by an overview of particle image velocimetry in § 2.2 and instrumentation in § 2.3. Possible sources of measurement errors are identified and quantified in § 2.3.1.

2.1 Rotor setup

The experiment was conducted in a room measuring 6.5 m × 8.0 m × 6.5 m on a rotor test stand as shown in figure 2.1. This test stand was installed at the center of the room. The setup consisted of a 1.0 m diameter, single-bladed rotor, whose blade was untwisted, manufactured with a square

This chapter may compose material from the author's previously published article, S. M. Mula and C. E. Tinney. A study of the turbulence within a spiralling vortex filament using proper orthogonal decomposition. *J. Fluid Mech.*, 769: 570–589, 2015. For this project, Tinney served as the project advisor.

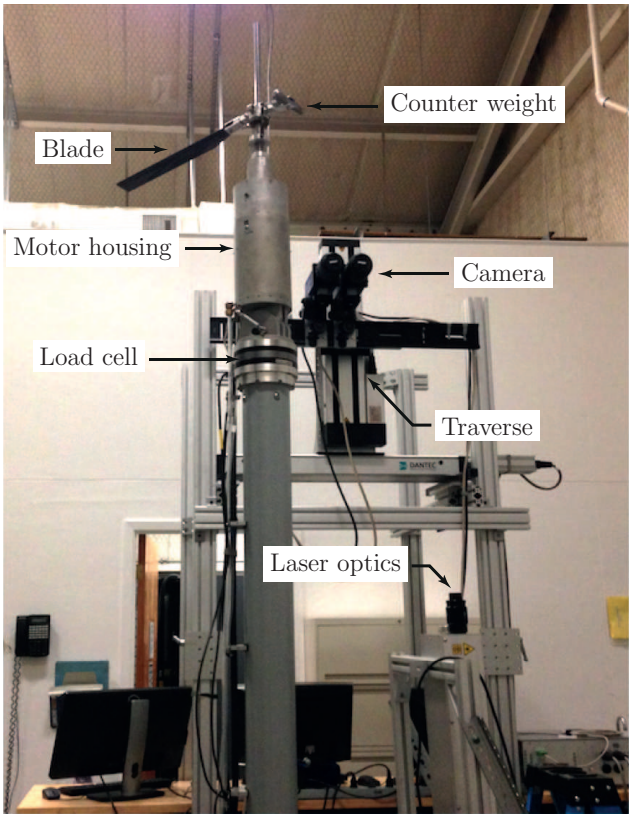

Figure 2.1: Rotor test stand.

tip and comprised a NACA 0012 airfoil profile with a constant chord of $c = 52$ mm (see figure 2.2). The blade was attached to the rotor hub by a flap-hinge, which allowed the blade to flap; the hub was located 3.0 m above the ground. A close-up view of this hub is illustrated in figure 2.3. By adjusting the pitch link, which was connected to the swashplate shown in figure 2.3, the blade was set to a collective pitch angle of 7.3°. Further, this single blade was balanced with a counter-weight (statically up to 99%) provided in figure 2.4. The rotor was operated by a 9 kW motor (located at the heart of the test

(a)

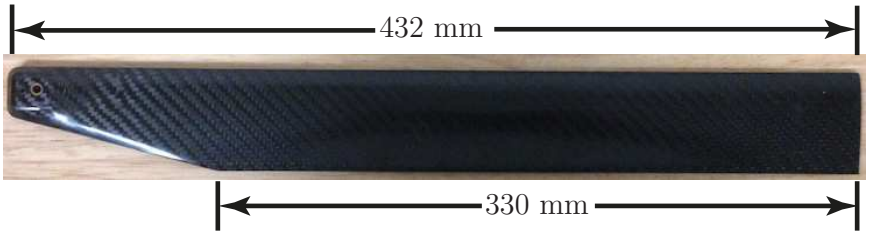

(b)

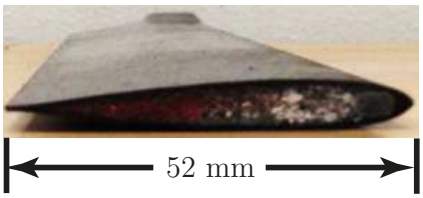

Figure 2.2: (a) Rotor blade and (b) its airfoil (NACA 0012).

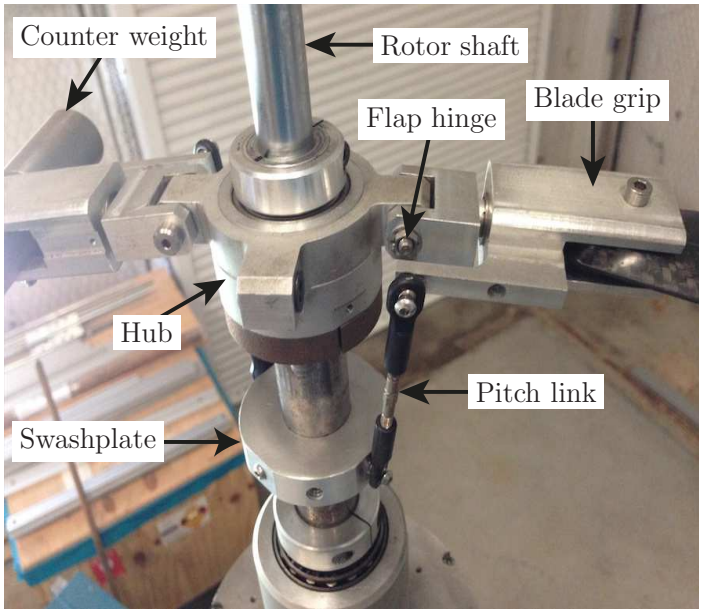

Figure 2.3: Close-up view of the rotor hub.

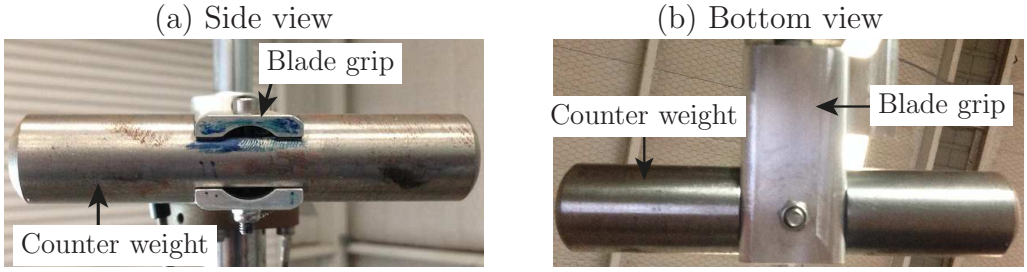

Figure 2.4: Counter weight in (a) side view and (b) bottom view.

stand in figure 2.1) that can provide a maximum rotational speed of 8000 RPM and a maximum torque of 10 Nm. For the current study, the rotor was operated at 1500 RPM which corresponds to a tip chord Reynolds number of $Re = 218,000$ ($Re = V_{tip}c/\nu$, where V_{tip} is the blade tip speed and c is the tip chord) and a tip Mach number of $Ma = 0.22$ ($Ma = V_{tip}/a$, where a is the speed of sound and is valued at 351.8 m/s). These conditions resulted in a blade loading of $C_T/\sigma = 0.066$, where the blade loading is a dimensionless measure of the thrust acting on the rotor blade. In C_T/σ, C_T is the coefficient of thrust ($C_T = T/\rho A V_{tip}^2$, where T is the rotor thrust and A is the rotor disk area), and σ is the rotor solidity, which is the ratio of the total blade area to the total disk area. The rotor thrust was measured using a fixed-frame load cell shown in figure 2.1. Details of the rotor parameters and the test conditions are provided in table 2.1.

2.2 Particle image velocimetry (PIV)

Given the conditions at which the rotor here is operated, the velocity measurements of the rotor wake are captured by way of Particle Image

Parameter	Value
Rotor diameter, $2R$	1.0 m
Number of blades, N_b	1
Blade chord, c	52 mm
Blade twist	0°
Blade airfoil	NACA 0012
Rotor hub	Flap hinge
Collective pitch	7.3°
Rotor speed, Ω	1500 RPM
Reynolds number, Re	218,000
Mach number, Ma	0.23
Solidity, $\sigma = N_b c/\pi R$	0.033
Rotor thrust, T	13 N
Coefficient of thrust, C_T	0.00218
Blade loading, C_T/σ	0.066

Table 2.1: Rotor parameters and test conditions.

Velocimetry (PIV). A brief description on how the PIV technique works is provided in this section, followed by details concerning the current instrumentation and measurements in § 2.3.

Particle image velocimetry is an optical, non-intrusive approach of obtaining spatially resolved, instantaneous, two-component or three-component velocity measurements on a multi-point grid space. The principal components of a PIV system include a CCD camera, a laser with sheet generating optics and a seed generator. Figure 2.5 shows a typical 2D PIV setup. To obtain velocity measurements using PIV,

1. The CCD camera is calibrated in order to relate seed particle displace-

ments to pixel dimensions of the camera

2. Fluid is then seeded with tiny particles, which can trace the fluid flow

3. The camera is then synchronized with the laser sheet in the double frame mode

4. After this synchronization, the field of view is illuminated twice with the laser sheet with a small separation time (called inter-frame timing) between the two laser pulses

5. The light scattered from tracer particles at the first and second illuminations of laser is then captured by the CCD camera on two different images.

6. The image plane is then divided into small interrogation windows (see figures 2.5 and 2.6). Average displacement of particles in each interrogation window is estimated by producing a correlation map (see figure 2.6) between the image intensities of the first and second images taken at the first and second pulses of laser, respectively. Based on the location of the correlation peak in the interrogation window, the displacement vector is determined; given the inter-frame timing, the velocity vector in each interrogation window is estimated.

7. The velocity field is then post-processed to remove any spurious displacement vectors; missing vectors are then interpolated using a nearest neighbor fit.

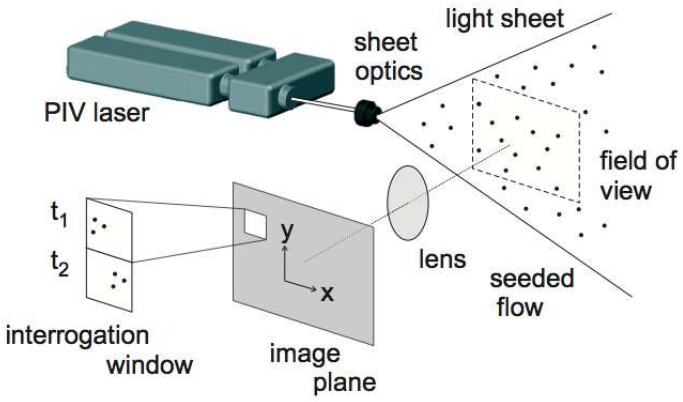

Figure 2.5: General setup of a 2D PIV system [18].

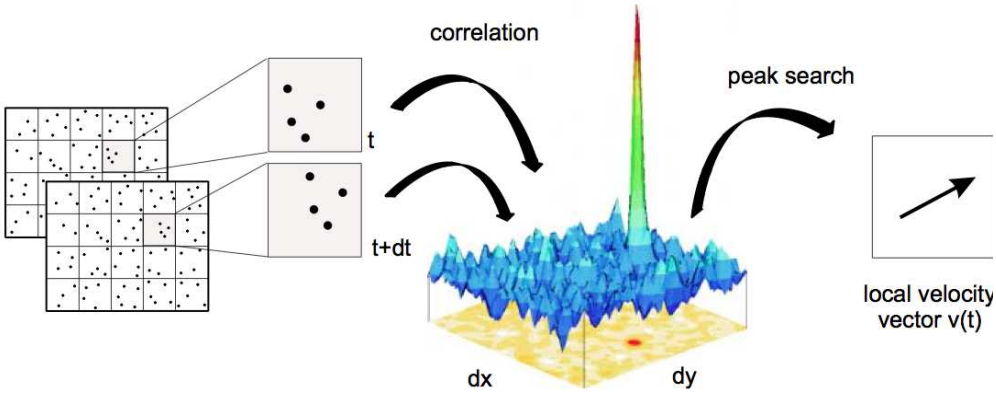

Figure 2.6: General method for evaluating PIV measurements [18].

2.3 PIV measurements of a rotor wake in hover

In the current study, two-component velocity measurements were performed along a 2D slice of the rotor wake (along a plane normal to the vortex filament axis) by phase aligning the rotor with the 2D PIV system (using a 1/rev optical switch). The PIV system used here is a commercial system manufactured by LaVision and comprises a double-pulse Nd-YAG laser source and a 2M pixel (1.6k $\times$ 1.2k pixel) CCD camera. The CCD camera is limited by a maximum sampling frequency of 15 Hz in double frame mode, which prevents time resolved measurements of the vortex filament from being performed. The laser source, with sheet forming cylindrical optics, produced a thin sheet (2 mm thickness) of 532 nm (green) laser. The laser sheet was oriented such that it was aligned along the quarter-chord of the blade at 0° vortex age. A schematic of the laser-sheet orientation is shown in figure 2.7 with a sample slice of the illuminated rotor wake being shown in figure 2.8. This slice illustrates multiple tip vortices of a spiraling vortex filament, which can be identified by the dark voids of olive oil seed; seeding was provided by way of a PIVTECH 14 cascadable Laskin nozzle olive oil seeder.

Given the orientation of the laser-sheet, the PIV camera was positioned such that the axis of the camera lens was orthogonal to the measurement plane in order to acquire a precise focus (see figures 2.7 and 2.10). The camera lens and the object distance were chosen such that only one vortex (including provisions for vortex wander) was captured so as not to compromise on the spatial resolution. The lens used here has a focal length of 105 mm ($f\# = 2.8$).

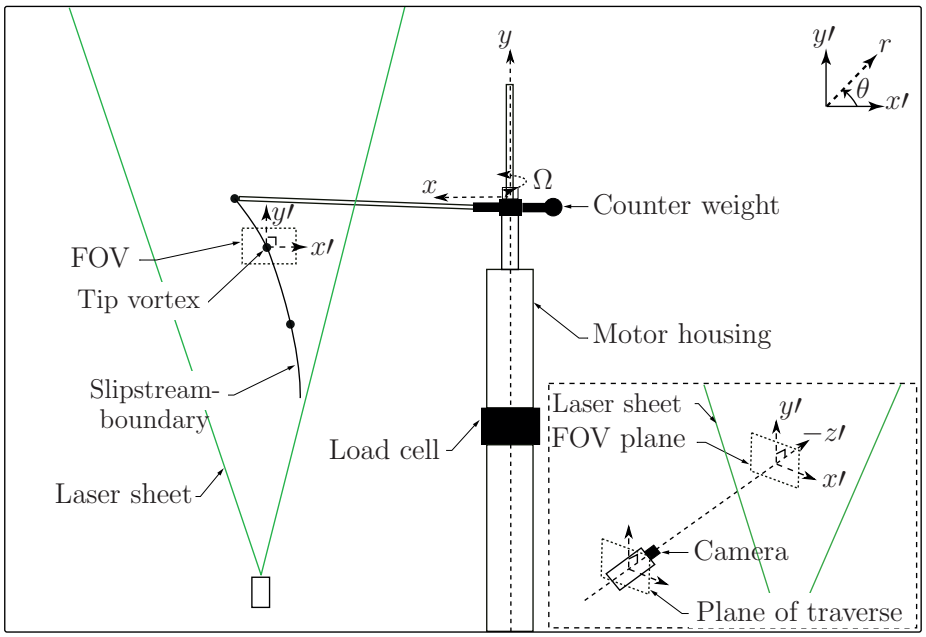

Figure 2.7: Schematic of the experimental setup and coordinate transformation.

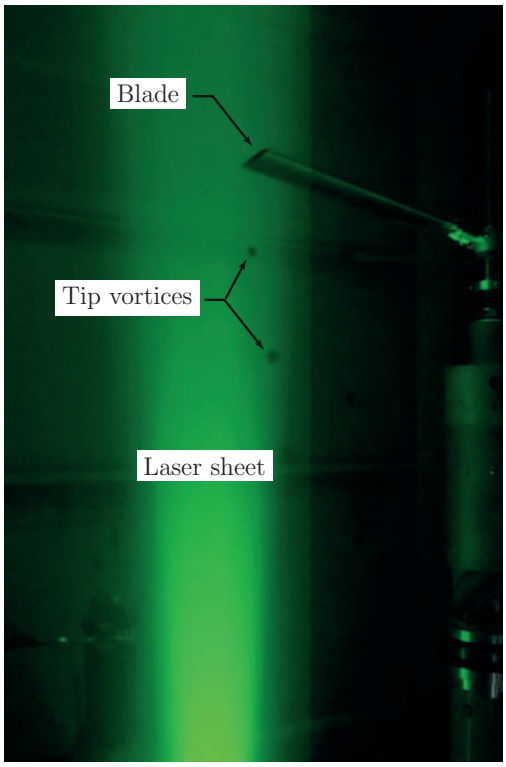

Figure 2.8: Tip vortices seen by dark voids of seed in the illuminated laser sheet.

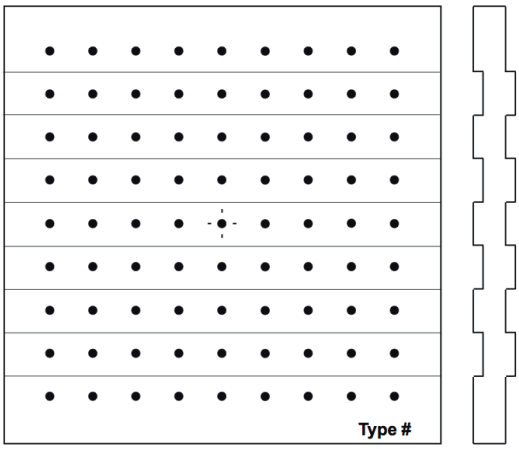

Figure 2.9: Schematic of a two-level calibration plate [18].

Once the setup (laser & camera) was arranged, the next essential step was the calibration of the camera. This is required in order to relate particle displacements to pixel dimensions. In order to do this, the calibration plate illustrated in figure 2.9 (comprising known reference points) was positioned such that its front edge, which faced the camera, was aligned along the laser sheet. An illustration of this is provided in figure 2.10. The plate was then focused and imaged by the camera lens. The markers were identified in the image and the calibration was processed using a pinhole model [18, 28]. The average deviation of the positions of the dewarped markers (in the image) from the ideal grid was found to be 0.28 pixel, which satisfies the suggestions that it be less than 0.3 pixel for the calibration to be considered good [34]. The resultant field of view (FOV) was found to be 88 mm×66 mm while the object distance of the lens was found to be $z_o =$ 905 mm.

After the calibration was performed, the inter-frame timing between

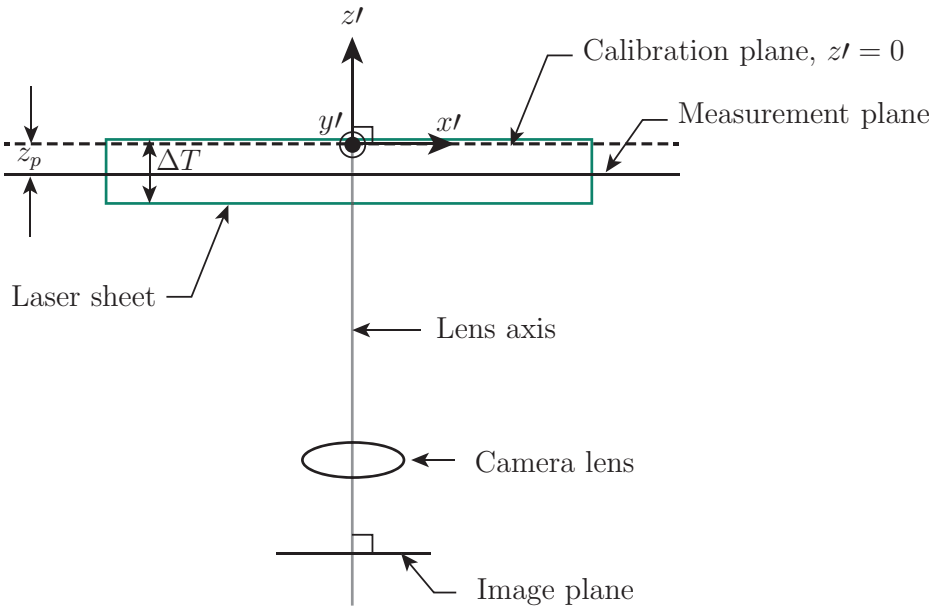

Figure 2.10: Schematic (unscaled) of the measurement plane, calibration plane and laser sheet. Front edge of the calibration plate represents the calibration plane.

the two laser pulses was adjusted to 36 μs. The test area was then seeded with atomized olive oil with adjustments being performed periodically to ensure good seed in the measurement region. This was an iterative process that required additional focusing of the camera. Measurements were then acquired at multiple vortex ages: $\psi = \{45°, 90°, 135°, 180°, 225°, 270°, 315°, 405°, 495°, 585°\}$, where 350 statistically independent pairs of PIV snapshots were acquired at each vortex age. Furthermore, the camera was repositioned at each vortex age using a 2D traverse so that the new vortex location was roughly centered on the camera image. This 2D traverse can be seen in figure 2.1 with the plane of the traverse also being illustrated in figure 2.7.

2.3.1 Measurements accuracies

Where the experimental and even numerical data is concerned, it is essential to determine the uncertainties associated with such measurements in order to ensure that quality and reliable data is acquired for subsequent analysis. Firstly the current setup assumes that the vortex axis is perpendicular to the measurement plane. Because of the relatively low blade loading on the rotor, the helical pitch ($\hat{p} = H/(2\pi R_c) = 0.046$, where H is the vertical displacement of the helix over one rotor revolution and $R_c = (1 + (H/(2\pi R))^2)R$ is the radius of curvature) and vortex filament torsion ($\hat{\tau} = P/R = 0.046$ using $P = H/(2\pi)$ as the reduced pitch) were also small so that the measurement plane was nearly orthogonal to the vortex axis [27,50,64]. The resultant angle of inclination between the vortex axis and a line normal to the measurement

plane was estimated to be 2.66°. The effect of this small correction appeared to have little influence on the low-dimensional features discussed in subsequent chapters. And so, this orthogonality assumption appears reasonable.

Secondly, given the inter-frame timing (36 μs) between the two laser pulses (laser sheet thickness of 2 mm) and the rotation speed of the rotor (1500 RPM), measurement accuracies are estimated to be within 0.3° of the blade motion (in rotor azimuth). Additional sources of measurement errors are discussed in more detail in the following sections.

2.3.1.1 Magnification errors

Prior to acquiring the PIV measurements, as it was mentioned earlier, the lens of the PIV camera was slightly adjusted in order to bring the measurement plane into focus. This adjustment resulted in a misalignment of the measurement plane (in $z\prime$ direction) from the calibration plane, which is illustrated in figure 2.10. This misalignment is on the order of the laser sheet thickness. Therefore, the offset location of the seed particles (z_p) relative to the calibration plane is on the order of 2 mm. Based on the object distance (z_o = 905 mm) acquired from the calibration, and using expressions from Discetti & Adrian (2012) [17], the magnification error is determined to be

$$\epsilon(\%) = \frac{\gamma}{1-\gamma} \times 100, \tag{2.1}$$

where $\gamma = z_p/z_o$ so that the resultant magnification error ϵ is found to be less than 0.2%.

2.3.1.2 Particle tracking errors

A second concerning source of error is associated with particle tracking which occurs when seed particles fail to accurately follow the fluid motion. In the current setup, seeding was provided by a PIVTEC 14 cascadable Laskin nozzle olive oil seeder, which produced particles with a nominal diameter of 1 μm (based on the manufacturer's specifications). Following the analysis of Birch & Martin (2013) [11], the maximum particle tracking error associated with each component of velocity (radial and tangential) is estimated. Birch & Martin (2013) considered an incompressible Batchelor vortex [5] with the following tangential velocity profile,

$$\frac{v\left(r\right)}{v_0} = \left(1 + \frac{1}{2\alpha}\right)\frac{1}{\eta}\left(1 - \exp\left(-\alpha\eta^2\right)\right), \tag{2.2}$$

where v_0 is the peak tangential velocity, r is the radial location from the center of the vortex, $\eta = r/r_c$ (r_c is the location of peak tangential velocity), and $\alpha = 1.25643$. By letting v' represent the tangential velocity of the seed particles, the tracking error associated with the tangential velocity can then be determined as

$$\frac{v}{v'} - 1 = A\exp\left(-B\eta^2\right), \tag{2.3}$$

where A represents the error amplitude in the tangential velocity. B is a constant over the range $14 \leq Cr_c/v_0 \leq 1400$, where $C = 18\nu/\phi d^2$, d is the particle diameter and $\phi = \rho'/\rho$ is the particle density ratio (ρ' is the particle density). The maximum value for the error amplitude A can be estimated

from the following expression,

$$A = 2\left(\alpha + \frac{1}{2}\right)^2 \left(\frac{v_0'}{Cr_c'}\right)^2, \tag{2.4}$$

where $r_c{}'$ is the radial location of peak tangential velocity (v_0') of seed particle. Estimates of $r_c{}'$ and v_0' are obtained from the PIV measurements. Table 2.2

ψ	v_0' (m/s)	r_c' (mm)	Cr_c'/v_0'	$A(\%)$	S_k
45°	31.18	5.51	62.98	0.155	0.111
270°	25.43	6.98	97.96	0.064	0.072
495°	27.44	8.21	106.65	0.054	0.065

Table 2.2: Particle tracking error estimates in tangential velocity.

provides an estimate of the tracking errors for the tangential component of velocity over the range of vortex ages studied. The maximum error is found to be less than 0.16%.

As for the radial component of velocity, centrifugal forces inside the vortex core induce a radial acceleration that alters the measured velocity in this direction. Because of this, tracking errors associated with the radial velocities are more sensitive than the tangential velocities. To estimate this error, we rely on the Stokes number. The Stokes number ($S_k = \tau'/\tau$) is a ratio of the characteristic time scales of the particle (τ') to that of the fluid (τ) and is listed in table 2.2. The time scale τ' is considered to be the response time of a particle (considered as a sphere in Stokes flow) when subjected to a unit step-change in fluid flow velocity whereas τ for the fluid is taken as the local

time scale $\tau = r/v$ associate with the large scale motion. Estimates for S_k in table 2.2 are obtained from the following expression,

$$S_k = 2\sqrt{2A}\left(1 - \frac{1}{\phi}\right). \tag{2.5}$$

To then quantify the tracking errors for the large scale vortex, Birch & Martin (2013) considered the case where $u = 0$ (no radial velocity in the vortex). An estimate of the tracking errors for the radial component of velocity are then obtained from the following expression,

$$\frac{u_0'}{v_0} = \frac{S_k}{5.8}, \tag{2.6}$$

where u_0' represents the maximum radial velocity of the particle, (induced by centrifugal forces) which is where the maximum error will reside. The resultant estimates for this source of error is provided in table 2.3 which shows that the maximum error in the radial velocity is less than 2.0% of v_0. Furthermore, the nominal diameter (1 μm) of the seed particles used in this experiment satisfies the suggestions for minimizing the particle tracking errors inherent to vortex dominated flows [49, 59].

ψ	S_k	$u_0'/v_0(\%)$
45°	0.111	1.91
270°	0.072	1.24
495°	0.065	1.12

Table 2.3: Particle tracking error estimates in radial velocity.

2.3.1.3 Peak locking errors

A check for peak locking errors[1] was also performed to ensure that the particle image displacements were unbiased by the integer pixel dimension. For an aberration free lens with circular aperture, the diffraction limited spot diameter is defined as [1, 58, 69, 93]

$$d_s = 2.44\ (M+1)\ \frac{f\lambda}{D}, \tag{2.7}$$

where λ is the wavelength of the laser used in the PIV system, f is the focal length of the lens, and D is the aperture diameter. M is the average lens magnification, which is obtained from the calibration. If d_p is the particle diameter, then the particle image diameter is obtained as

$$d_\tau = \sqrt{M^2 {d_p}^2 + {d_s}^2}. \tag{2.8}$$

For error-free estimates, $d_\tau/d_r \geq 2$ [93], where d_r is the pixel diameter of the

λ (nm)	$f^\# = \frac{f}{D}$	M	d_s (m)	d_r (m)	d_τ/d_r
532	2.8	0.135	4.1×10^{-6}	7.4×10^{-6}	0.56

Table 2.4: Peak locking estimates.

camera (specified by the manufacturer). For the current setup, based on the nominal particle diameter of the seed (1 μm), $d_\tau/d_r = 0.56 \leq 2$ (see table 2.4). Therefore, the measurements are prone to peak locking errors. To minimize

[1] The bias of particle image displacements to integer pixel dimension is called peak locking which occurs when the particle image diameter is less than the pixel dimension of the camera.

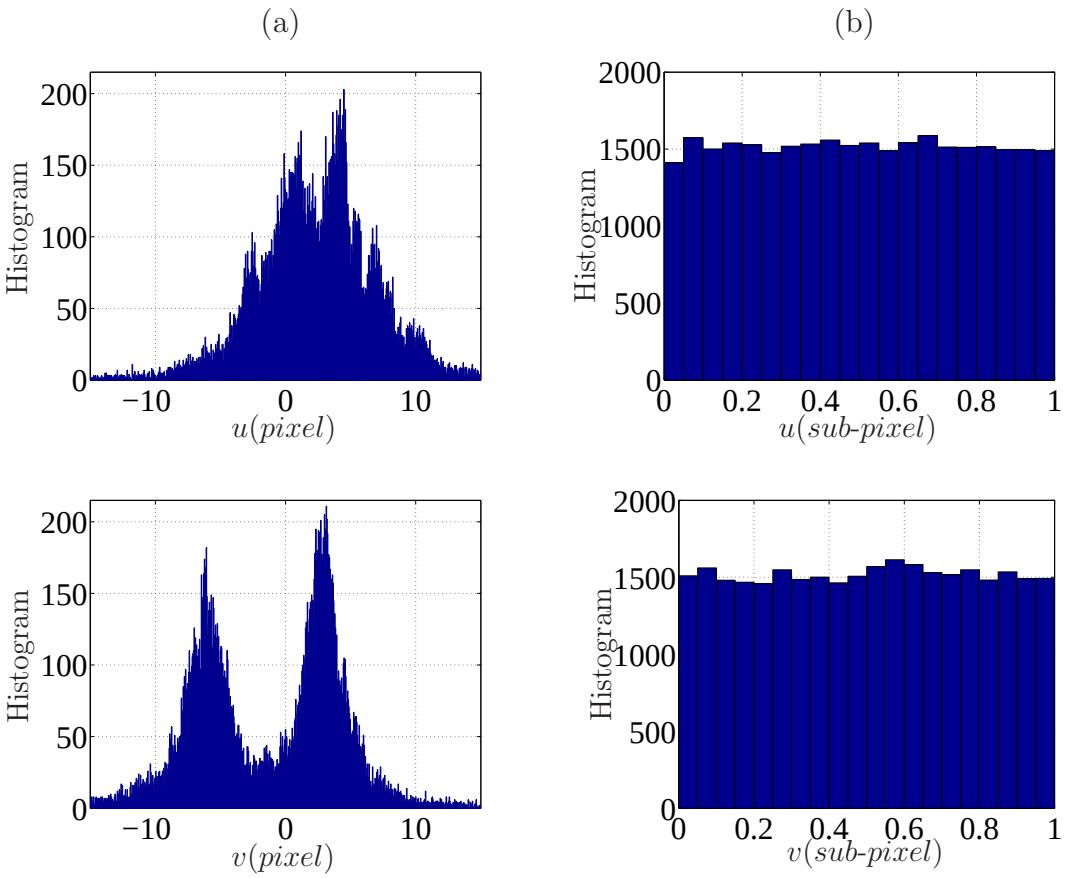

Figure 2.11: (Top) (a) Histogram of the measurement horizontal displacement and (b) its corresponding sub-pixel component. (Bottom) (a) Histogram of the measurement vertical displacement and (b) its corresponding sub-pixel component. Bin size is 0.05 pixels and the plots are illustrated for a sample instantaneous data at $\psi = 90°$.

these errors, the PIV images were slightly blurred. Sample histograms of the horizontal and vertical pixel displacements are shown in figure 2.11a (top & bottom), respectively, with that of the corresponding subpixel components in figure 2.11b (top & bottom), respectively. Therefore, as seen in figure 2.11b, peak locking errors are significantly minimized by having a nearly uniform distribution of particle image displacements in the sub-pixel dimension.

2.3.2 PIV vector processing

As for the processing of the raw PIV data, image pairs were converted to vector maps using DaVIS $v7.2$ with an initial interrogation window size of 64 pixel $\times$ 64 pixel that iteratively reduced to a final size of 16 pixel $\times$ 16 pixel with a 50% overlap. The resulting measurement resolution L_m, which is uniform in both $x\prime$ and $y\prime$, was found to be 0.88 mm (grid resolution = $L_m/2$). Spurious vectors were filtered by first establishing a threshold signal-to-noise ratio (set to 1.5 as per the suggestions in literature [72]), followed by the removal of groups (of less than 5 vectors) that then ended with a four-pass regional median filter [65, 92]. Spurious vectors often occurred in the inner core of the vortex due to the poor seeding levels that arise from centrifugal forces [40] (see figures 2.8 and 2.12a). Missing vectors were then interpolated using a nearest neighbor fit. Figure 2.12 shows a sample raw PIV vector map (sub-sampled and filtering enabled), and the resultant vector-map (after interpolation and smoothing) that is used in the subsequent analysis. The post-processed vector map is shown to fit the overall flow structure quite well.

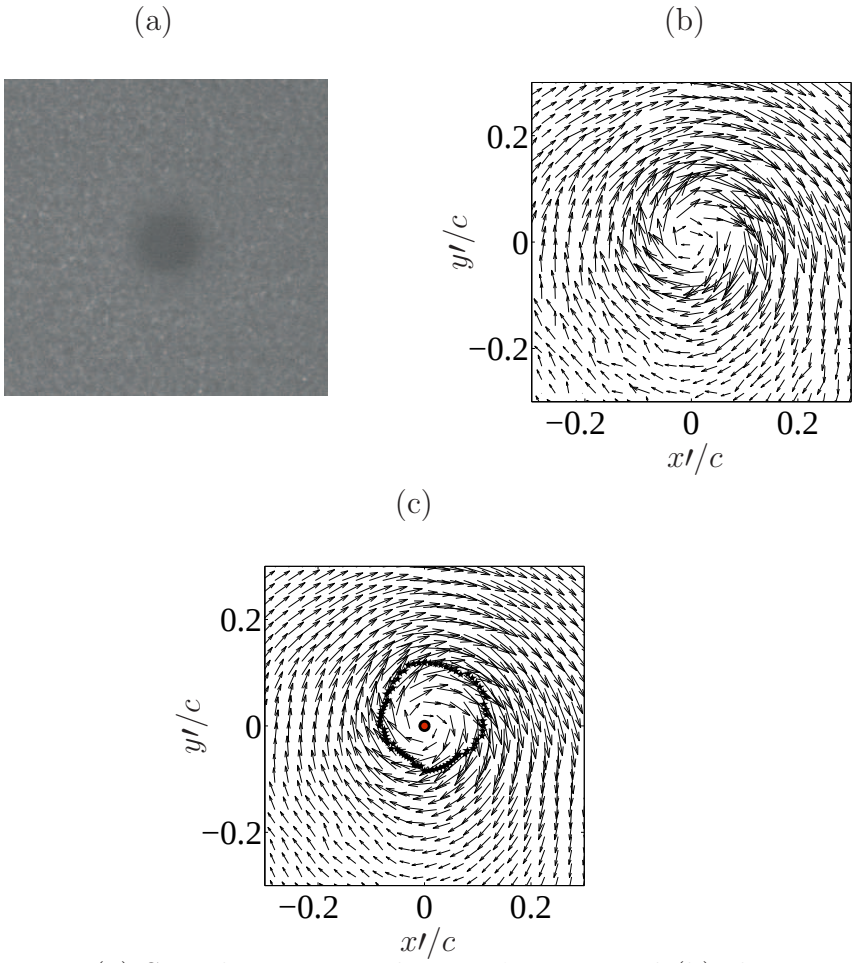

Figure 2.12: (a) Sample PIV snapshot at $\psi = 45°$ and (b) the corresponding original vector map (sub-sampled) with (c) the corresponding post-processed vector map. The vortex center and core boundary are also identified.

Chapter 3

Analysis technique

The overarching objective of this study is to develop a statistical description of the turbulence and inactive motions of a helical vortex produced by a single-bladed rotor during hover. To accomplish this, we will need to employ two separate analyses. The first requires one to correct for the wandering motions of the vortex so that an accurate mechanistic description of the vortex filament's statistical properties can be made. The second analysis method is employed to categorize the energy associated with the various constituents that make up the vortex. The outline of this chapter is as follows. In § 3.1, the various vortex centering techniques are reviewed and compared from which the mean statistics of the tip vortices are computed and displayed in § 3.2. The vortex wander, mean core-radius, swirl velocity, axial vorticity and turbulence fluctuations are shown and compared to a sampling of data provided in the open literature. This is done simply for no other reason than to provide

This chapter may compose material from the author's previously published articles,

S. M. Mula and C. E. Tinney. A study of the turbulence within a spiralling vortex filament using proper orthogonal decomposition. *J. Fluid Mech.*, 769: 570–589, 2015. For this project, Tinney served as the project advisor.

S. M. Mula, J. H. Stephenson, C. E. Tinney and J. Sirohi. Dynamical characteristics of the tip vortex from a four-bladed rotor in hover. *Exp. Fluids*, 54, 1600, 2013. For this project, Stephenson built the rotor test stand while Tinney and Sirohi served as the project advisors.

confidence in the measurements reported here, the true focus being that of the turbulence characteristics. This is followed by a description of the proper orthogonal decomposition (POD) technique in § 3.3 which is then applied to the 'wander corrected' PIV images. It is important to mention that the choice of the wander correction technique was found to influence the results obtained by way of POD. This important issue will be addressed at a later stage in § 6.

3.1 Vortex center identification techniques

Prior to performing any statistical analysis it is essential to first correct for vortex wander; otherwise, merely computing an ensemble average of instantanous vortices artificially results in high velocity fluctuations (as shown by Baker *et al.* (1974) [3], Devenport *et al.* (1996) [16], Heyes *et al.* (2004) [31] and, Bailey & Tavoularis (2008) [2]). In order to provide corrections for wander, the instantaneous vortex centers have to be identified; a number of schemes have been proposed for identifying the vortex center of a vortex core. A brief outline of these techniques, excerpted from Mula *et al.* (2013) [64], is provided below.

3.1.1 Centroid of Q (CoQ)

The centroid of Q determines the area center of scalar Q as described by van der Wall & Richard (2006) [89]. The second invariant, Q, comprises the symmetric (Λ) and skew-symmetric (Π) components of the velocity gradient

tensor, defined as,

$$Q = \frac{1}{2}(\tilde{u}_{i,i}^2 - \tilde{u}_{i,j}\ \tilde{u}_{j,i}) = -\frac{1}{2}(\tilde{u}_{i,j}\ \tilde{u}_{j,i}) = \frac{1}{2}(\|\Pi\|^2 - \|\Lambda\|^2), \tag{3.1}$$

where $\|\Pi\| = \mathrm{tr}[\Pi\Pi^t]^{1/2}$, $\|\Lambda\| = \mathrm{tr}[\Lambda\Lambda^t]^{1/2}$ and $\Lambda_{ij} = \frac{1}{2}(\tilde{u}_{i,j} + \tilde{u}_{j,i})$, $\Pi_{ij} = \frac{1}{2}(\tilde{u}_{i,j} - \tilde{u}_{j,i})$. Subscripts are written to define the derivative of the first subscript with respect to the second where $i, j = 1, 2, 3$. The region of vorticity intensity, as described by Hunt *et al.* (1988) [33], is identified by the region of positive Q. In order to pinpoint a center for the vortex core, one may choose to consider the centroid of the positive Q region; hence, centroid of Q [89]. Here the centroid of Q (X_c, Y_c) is determined as

$$(X_c, Y_c) = \left(\frac{\sum x\prime Q(x\prime, y\prime)}{\sum Q(x\prime, y\prime)}, \frac{\sum y\prime Q(x\prime, y\prime)}{\sum Q(x\prime, y\prime)} \right). \tag{3.2}$$

This is analogous to the center of mass approach where the numerator on the right-hand side of Eq. 3.2 would represent the sum of mass moments about the respective axis while the denominator would represent the total mass. For this centroid of Q approach, only those regions with $Q(x\prime, y\prime) > 0$ are considered.

3.1.2 Centroid of vorticity

The centroid of vorticity is similar to the CoQ method previously described. The vortex center using this method is identified as the centroid of axial vorticity on 2-D slices $(x\prime, y\prime)$ of the rotor tip vortex filament.

3.1.3 Normalized helicity

Normalized helicity was first introduced by Levich & Tsinober (1983) [44], and is defined as the cosine of the angle between velocity ($\vec{\tilde{u}}$) and vorticity ($\vec{\omega}$). The expression for normalized-helicity is

$$H = \frac{\vec{\tilde{u}} \cdot \vec{\omega}}{|\vec{\tilde{u}}||\vec{\omega}|}. \tag{3.3}$$

In the normalized-helicity method, vortex centers are identified as maximal normalized-helicity points on each of the 2-D slices $(x\prime, y\prime)$ of the rotor tip vortex filament [45].

3.1.4 Γ_1 method

The Γ_1 method is a non-Galilean invariant approach introduced by Graftieaux *et al.*(2001) [24] which provides a simple and robust way to identify centers of vortical structures in a flow. This method defines a scalar function Γ_1 as

$$\Gamma_1(P) = \frac{1}{N} \sum_S \frac{(P\vec{M} \times \vec{\tilde{u}}_M) \cdot \hat{e_z}}{|P\vec{M}||\vec{\tilde{u}}_M|}, \tag{3.4}$$

where $P\vec{M}$ defines the radius vector between a fixed point P in the measurement domain and all other points M in the region S, which could be of any arbitrary shape, that encloses point P for an estimate of $\Gamma_1(P)$ (see figure 3.1). $\vec{\tilde{u}}_M$ is the total velocity vector at point M and $\hat{e_z}$ is the unit vector normal to the measurement plane. The vortex center is identified by a point where Γ_1 is maximum. Being an integral based approach, the results are not corrupted

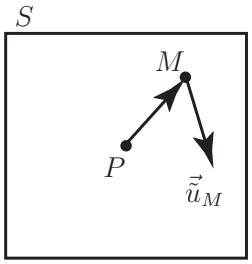

Figure 3.1: Schematic illustration for the Γ_1 method.

by noise introduced by divergences of the velocity field, albeit, the vortex center still relies on an accurate assessment of the velocity inside the vortex core where seeding is poor.

3.1.5 Geometric center

In the geometric center approach, the center of the vortex core is based on the geometry of the vortex core. A demonstration of this is shown in figure 3.2a from a raw PIV vector map using lightly shaded regions to identify where $Q > 0$ with dark circles depicting locations of peak swirl velocity, which define the bounds of the vortex core. Remarkable similarities in the boundaries of positive Q and the peak swirl velocity are manifest. The geometric center can then be identified using two different approaches. The first of these applies a best fit ellipse to the bounds of the peak swirl velocity whereby the geometric center is identified as the center of this ellipse (referred hereafter as GC-ellipse). In the second approach, the geometric center is identified as the average location of all points confined by the bounds of the peak swirl velocity

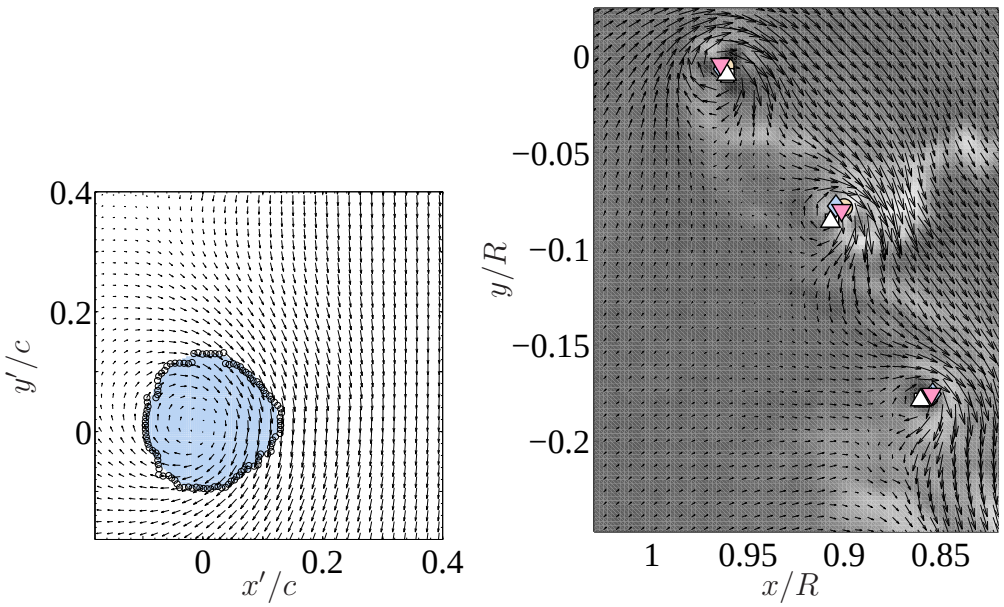

Figure 3.2: (a) Q method applied to a sample vortex at 250° vortex age from the measurements of Mula *et al.* (2013) [64]. Dark circles identify locations of peak swirl velocity. (b) Sub-sampled PIV vector map at 40° wake age from the studies of Mula *et al.* (2013) [64]. Vortex centers detected using CoQ (circle), centroid of vorticity (diamond), maximum normalized helicity (square), Γ_1 method (triangle-up), GC-ellipse (star) and GC-average (triangle-down)

(referred hereafter as GC-average). Mula *et al.* (2013) [64] have shown these two approaches to produce indistinguishable results.

Taken from the measurements of Mula *et al.* (2013) [64], figure 3.2b shows a sub-sampled PIV vector map at 40° wake age with the vortex centers identified using CoQ, centroid of vorticity, maximum normalized helicity, the Γ_1 method and geometric center (both approaches) to demonstrate the differ-

ences among these techniques. As the CoQ, normalized helicity and centroid of vorticity are divergence-based schemes, their accuracies in pin-pointing the vortex center have been the subject of scrutiny. Although the geometric center method is a non-divergence based technique, for a strained vortex, such as the rotor tip vortex, the geometric center of the vortex core does not have to coincide with the actual vortex center (the location of zero swirl). Therefore, for the current set of measurements, the Γ_1 method is preferred and is employed for the remainder of the analysis.

3.2 Vortex characteristics

Following the application of the Γ_1 method in the current study, the vortex centers of the instantaneous tip vortices are identified (sample illustration shown in figure 3.3) and the wander characteristics are derived, with a subsequent analysis of the mean characteristics: core-radius, swirl velocity, axial vorticity and turbulence fluctuations.

3.2.1 Vortex wander

Each instantaneous vortex is represented by its vortex center $(x^\star, y^\star)$ in order to demonstrate the wander characteristics; $(x^\star, y^\star)$ are the coordinates of instantaneous vortex center with respect to the mean vortex center, where the coordinate system $(x^\star, y^\star)$ is parallel to $(x\prime,\ y\prime)$. Figure 3.4a illustrates the wander fitted with a 95% confidence ellipse for a vortex at all the vortex ages in the measurement envelope: $\psi = 45^\circ - 585^\circ$. Overall, wander appears

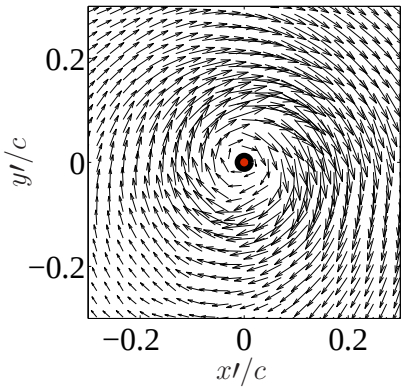

Figure 3.3: Instantaneous PIV vector map (sub-sampled) at $\psi = 180°$ with the vortex center ($\circ$) identified using the Γ_1 method.

to increase with the increasing vortex age. Further, as demonstrated by the 95% confidence ellipse, the wandering motion appears to be anisotropic in agreement with the previous studies (see Kindler *et al.* (2010) [39], Mula *et al.* (2013) [64] and Karpatne *et al.* (2014) [37]), which showed an anisotropic nature of wander for vortices from multi-bladed rotors in hover.

In order to quantify the characteristics of wander, figure 3.4b illustrates the standard deviation of wander along the principal major and minor axes (of the 95% confidence ellipse) across all the vortex ages studied. A third-order least-squares fit has also been added (identified by the solid and dashed lines) to help with the interpretation. This wandering motion is shown to grow linearly along the principal minor axis. Wander along the major axis grows faster than that of the minor axis at earlier vortex ages. However, the wandering motion (along the major axis) does not appear to show a continuous growth as it deviates from the least-squares fit in the vicinity of the first blade

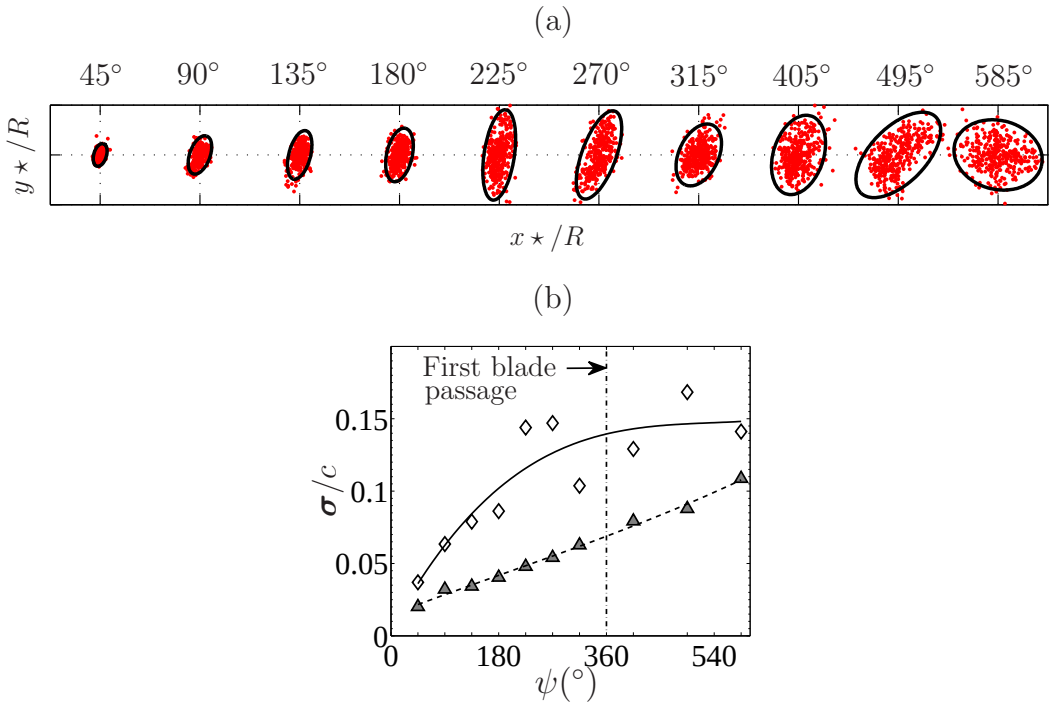

Figure 3.4: (a) Vortex wander with a 95% confidence ellipse at $\psi = 45° - 585°$. Dashed lines are separated by 0.04 in $x\star/R$ and 0.02 in $y\star/R$. (b) Standard deviation of vortex wander along the principal major ($\diamond$, ⎯) and minor ($\triangle$, ...) axes.

passage (360°). It is postulated that this discontinuity is a consequence of long-wave instabilities with non-integer wave numbers [9]. The growth rate of these long-wave instabilities have been shown to manifest a local minimum near the first blade passage, which is evident in figure 3.4b.

Having determined the instantaneous vortex centers with the wander characteristics, a correction for wander is performed which is illustrated in figure 3.5a. Each of the 350 instantaneous vortex centers, along with their vortices, is shifted to the mean vortex center. Figure 3.5b, c shows the mean velocity vector field for a vortex at $\psi = 180°$ before and after correction for wander, respectively. Vortex core boundaries identified by the locations of peak swirl velocity on the mean velocity field are also indicated. It is evident from figure 3.5 that the shape and size of the core before wander correction is remarkably different from that after correction; the presence of wander merely smears the uncorrected average vortex thereby falsely resulting in a bigger core.

3.2.2 Convergence test

Following the correction for wander, and prior to obtaining the mean characteristics, it is essential to determine if sufficient convergence has been achieved given the number of instantaneous samples available for analysis (350 PIV vector maps at each vortex age). Figure 3.6 illustrates the convergence of the mean core-radius and swirl velocity at a sample vortex age of $\psi = 405°$. It is evident from figure 3.6a that sufficient convergence in the mean core-radius

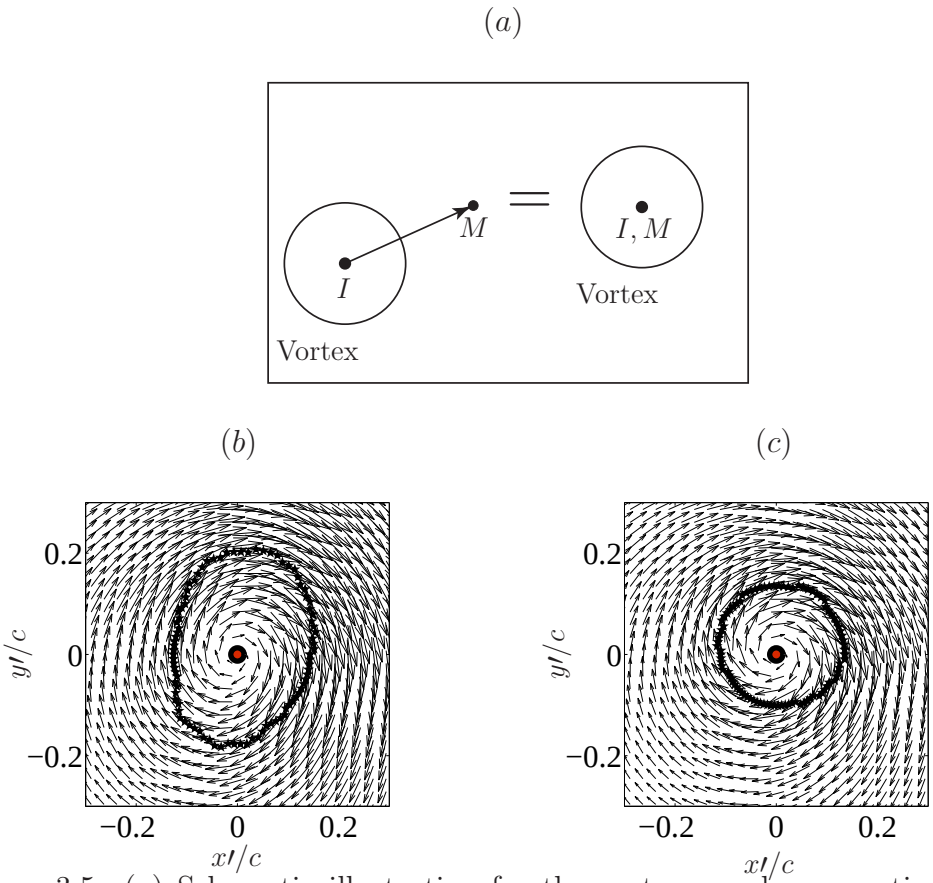

Figure 3.5: (a) Schematic illustration for the vortex wander correction. M and I are the mean and instantaneous vortex centers, respectively. Mean velocity vector field (sub-sampled) at $\psi = 180°$ (b) before and (c) after wander correction. Corresponding vortex core boundaries are also identified.

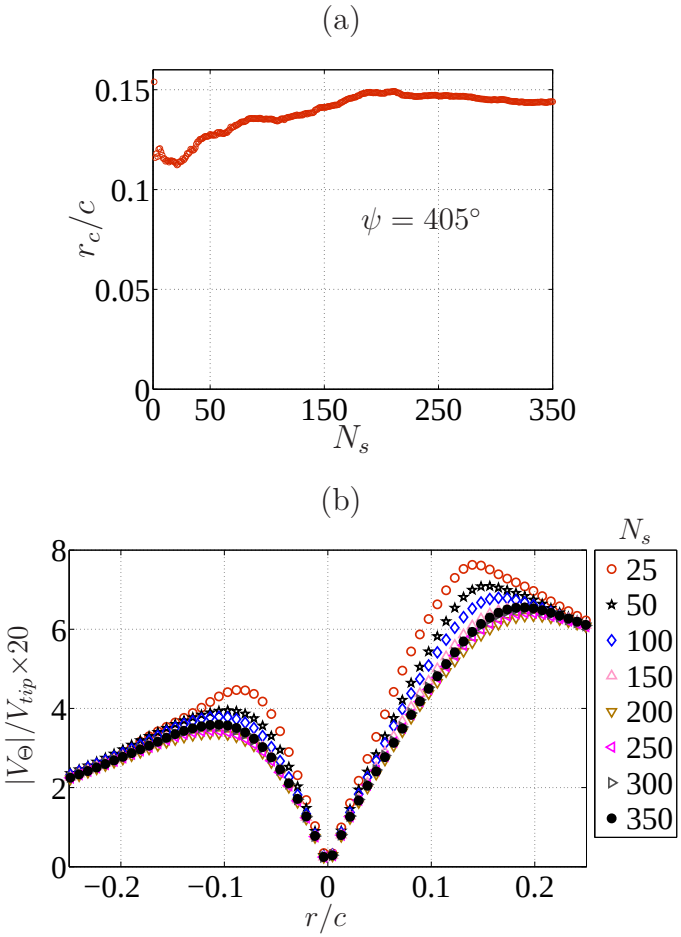

Figure 3.6: (a) Convergence of mean core-radius. (b) Convergence of mean swirl velocity, $|V_\Theta/V_{tip}|$, on a vortex slice: number of samples $N_s = 25 - 350$

is achieved for the total number of samples acquired in the current setup (350 samples). Similar convergence is demonstrated for the mean swirl velocity on a sample vortex slice in figure 3.6b.

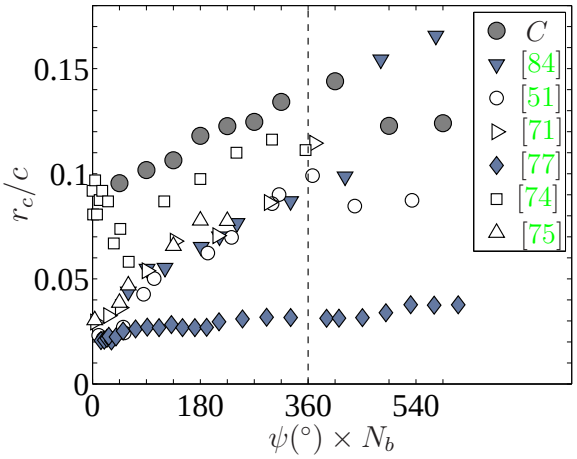

Figure 3.7: Core-radius trends of the current study (C) compared to the previous studies listed in table 3.1.

3.2.3 Mean statistics

Having obtained sufficient convergence, figure 3.7 illustrates the mean core-radius estimates for all the vortex ages in the measurement envelope (after wander correction). The core-radius at each vortex age is determined by the average of azimuthal locations of peak swirl velocities (of a mean vortex core, for example see figure 3.5b). The profile in figure 3.7 shows a monotonic increase from 10% to 15% of the blade chord up until the first rotor revolution. Here the current findings are compared to those reported in the open literature; see table 3.1 for a listing of the rotor operating conditions associated with these studies. In the current study, at the earliest vortex age of 45°, $L_m/r_c = 0.17$ (< 0.2), which satisfies the measurement resolution requirements suggested by Grant (1997) [25] and Martin *et al.* (2000) [55] for determining core-radius. In

Data source	Device	N_b	Re $\times 10^{-5}$	Ma	C_T/σ
Current work	PIV	1 ($\star$)	2.18	0.23	0.066
Thompson *et al.* (1988) [84]	LDV	1 ($\star$)	2.70	0.09	0.086
Leishman (1998) [51]	LDV	1 ($\star$)	2.72	0.28	0.09
Ramasamy & Leishman (2004) [71]	LDV	1 ($\star$)	2.72	0.26	0.064
Richard *et al.* (2008) [77]	PIV	4 ($\oplus$)	14.0	0.63	0.036
Ramasamy *et al.* (2009a) [74]	PIV	2 ($\star$)	0.34	0.08	0.113
Ramasamy *et al.* (2009b) [75]	PIV	1 ($\star$)	2.72	0.26	0.064

Table 3.1: Overview of the experimental conditions reported by others on the core-radius estimates using twisted ($\oplus$) and untwisted ($\star$) blades.

general, the trends in figure 3.7 are consistent with the open literature. That is, up until the first blade passage (360°), diffusion causes the core-radius to increase with increasing vortex age. Aside from the studies of Thompson *et al.* (1988) [84] and Richard *et al.* (2008) [77], the core-radius is shown to decrease after the first blade passage due to vortex stretching induced by the oncoming blade. The corresponding vortex Reynolds number (Γ_v/ν, where Γ_v is the circulation of the vortex) of our study was found to range between 8.3 $\times 10^4$ and 8.7$\times 10^4$ over the vortex ages studied.

Illustrations of the mean axial vorticity at $\psi = 45°$ to 495° are shown in figure 3.8. As expected, the mean axial vorticity peaks at the vortex center and decreases radially away from the vortex axis. It is also evident that the tip vortex core is asymmetric across the vortex ages in the measurement envelope. Such an asymmetry across the vortex ages is attributed to the fact that the helix emanated from the rotor is semi-infinite.

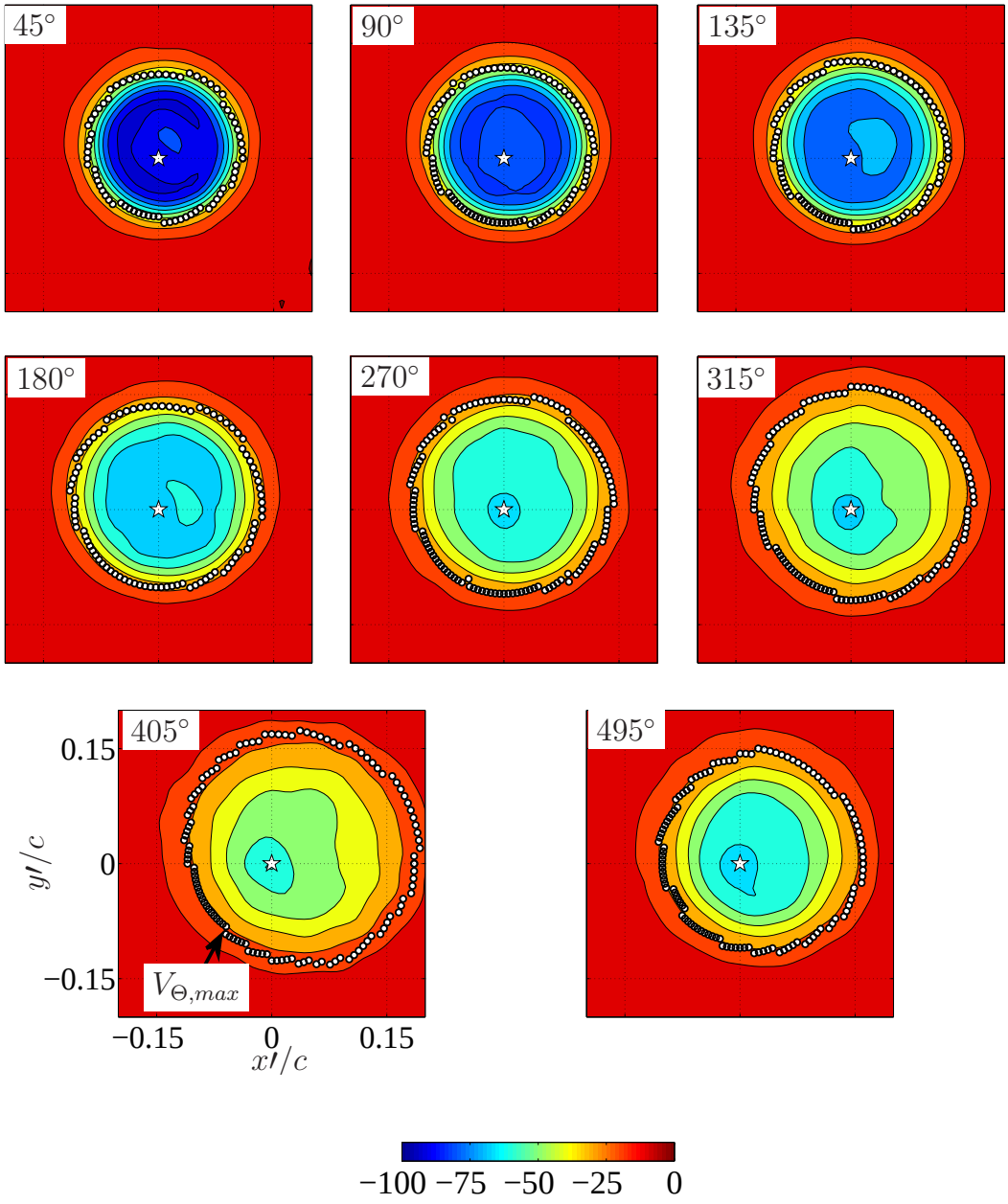

Figure 3.8: Contours of the mean axial vorticity (ω_z/Ω) at $\psi = 45°$ to $495°$. Locations of peak swirl velocity ($V_{\Theta,max}$), which define the boundaries of the vortex core, also identified.

Since the torsion of the helix is very small ($\hat{\tau} = 0.046$), its influence is significant on the binormal induced velocity (of the vortex), which is primarily responsible for the displacement of the vortex filament in a fluid [76]. Here, the binormal velocity is computed as the net in-plane velocity of the vortex,

$$\vec{v}_b = \frac{1}{A}\int\int \vec{U}(x\prime, y\prime)dx\prime dy\prime, \quad A = \int\int dx\prime dy\prime, \tag{3.5}$$

where $\vec{U}(x\prime, y\prime)$ is the mean (in-plane) velocity field within the vortex, A is the area of the vortex and the limits of integration are confined to $\sim 2r_c$ (from the vortex center). The dimensionless binormal velocity is then estimated using $\hat{v}_b = |\vec{v}_b|4\pi R_c/\Gamma_v$ and is provided in table 3.2 at various vortex ages throughout the measurement envelope using Γ_v as the circulation strength of the vortex. A comparison of our estimates to the theoretical predictions is also provided based on the following analytical expression from Ricca (1994) [76],

$$\hat{v}_b = \log\frac{R_c}{r_c} + C_{MS}, \tag{3.6}$$

where C_{MS} depends on the geometry of the helix and is determined using the closed analytical expression

$$C_{MS} = -\frac{1}{4} + \hat{p}^{-1} + \log\hat{p} + 1 - \frac{1}{2}\hat{p} + [\frac{3}{8}\zeta(3) - \frac{1}{2}]\hat{p}^2 - \frac{5}{8}\hat{p}^3 + O(\hat{p}^4), \tag{3.7}$$

derived by Boersma & Wood (1999) [12] for thin helical filaments of small pitch. These theoretical estimates are shown to compare favorably with our laboratory measurements.

The average spatial topography of the turbulence kinetic energy per unit mass (TKE $= 0.5\langle u_1^2 + u_2^2\rangle$, $u_{i=1,2}$ being the fluctuating part of the in-plane

		Measured			Predicted using Eq. 3.6
ψ (°)	Γ_v (m^2/s)	$\lvert\vec{v}_b\rvert$ (m/s)	$\hat{v}_b = \lvert\vec{v}_b\rvert / \frac{\Gamma_v}{4\pi R_c}$	C_{MS}	$\hat{v}_b$
45	1.311	5.26	25.25	19.38	23.99
135	1.349	5.23	24.41	19.38	23.86
270	1.325	4.74	22.54	19.38	23.72
315	1.386	4.85	22.03	19.38	23.62

Table 3.2: Estimates of the binormal induced velocity measured from the current experiment compared with the theoretical predictions using Eq. 3.6.

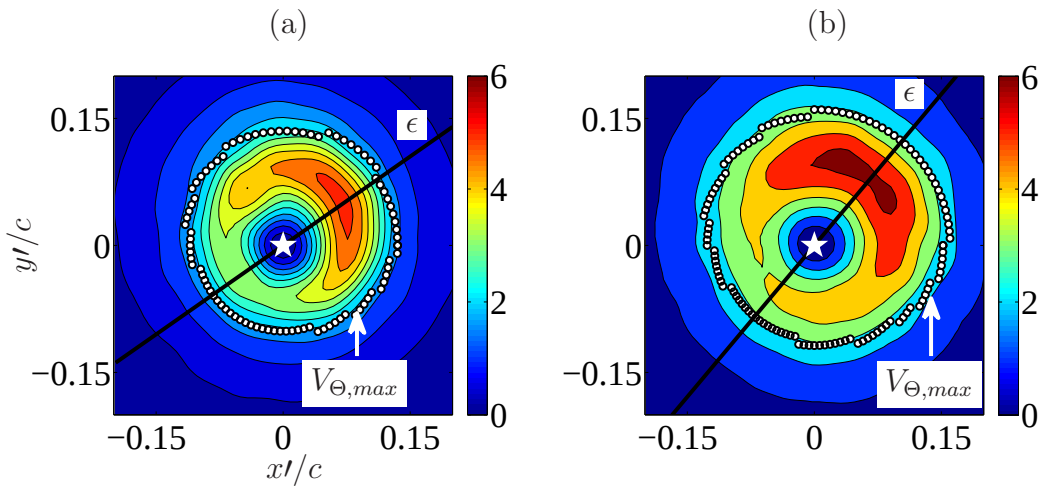

Figure 3.9: Turbulent kinetic energy per unit mass, (TKE/V_{tip}^2) $\times 10^3$, at (a) $\psi = 180°$ and (b) $\psi = 315°$. Locations of peak swirl velocity ($V_{\Theta,max}$) also identified.

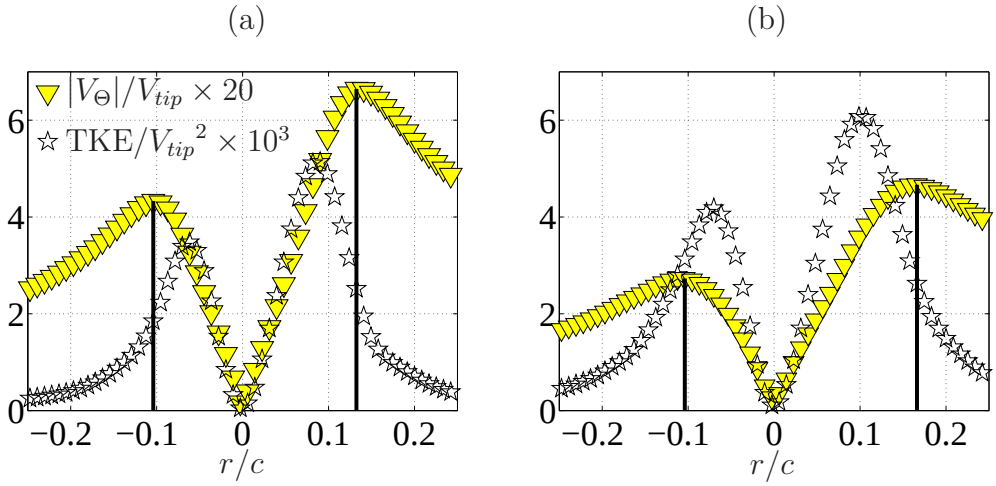

Figure 3.10: Swirl velocity, $(|V_\Theta|/V_{tip}) \times 20$ ($\triangledown$), and $(\text{TKE}/V_{tip}^2) \times 10^3$ ($\star$) at (a) $\psi = 180°$ and (b) $\psi = 315°$ on a vortex slice.

velocity components), for vortices captured at $\psi = 180°$ and 315° are shown in figure 3.9a, b, respectively. Since the in-plane velocity at the vortex center is zero, which is an inherent characteristic of a vortex flow, fluctuating part of the in-plane velocity is also zero ($u_{i=1,2} = 0$); therefore, the TKE approaches zero at the vortex center. The TKE peaks inside the bounds of the vortex core [16, 27], which are identified by the locations of peak swirl velocities ($V_{\Theta,max}$). Figure 3.10a, b shows the profiles of TKE (along with mean swirl velocities) on a sample slice ϵ in figure 3.10a, b for $\psi = 180°$ and 315°, respectively. From figures 3.9 and 3.10, the TKE is asymmetric inside the vortex core, which persisted across all the vortex ages in the measurement envelope. Further, it is worth estimating how energetic these velocity fluctuations are relative to the kinetic energy contained by the mean field. Therefore, the total resolved

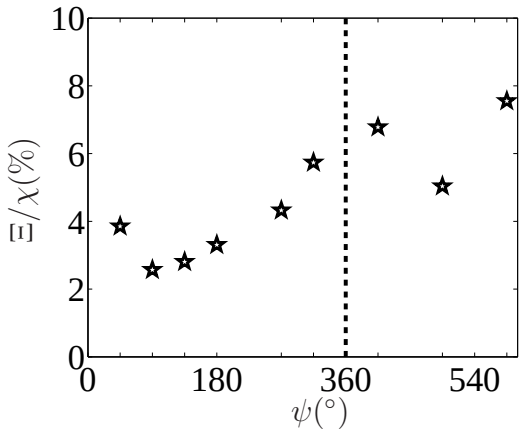

Figure 3.11: Total resolved turbulence kinetic energy (Ξ) normalized with the total resolved kinetic energy (χ) of the mean flow.

turbulence kinetic energy (Ξ) of a vortex (at each ψ) is determined,

$$\Xi(\psi) = \frac{1}{2}\int_A \langle u_i(x\prime, y\prime, \psi, t) u_i(x\prime, y\prime, \psi, t)\rangle dA, \tag{3.8}$$

where $dA = dx\prime dy\prime$. Likewise, the total resolved kinetic energy (χ) of the mean vortex flow at each ψ is estimated,

$$\chi(\psi) = \frac{1}{2}\int_A \langle U_i(x\prime, y\prime, \psi) U_i(x\prime, y\prime, \psi)\rangle dA, \tag{3.9}$$

with $U_{i=1,2}$ being the in-plane mean velocity components. Figure 3.11 illustrates how Ξ compares to χ in the measurement envelope. It is clear that Ξ is on the order of 2-8% of χ for the range of vortex ages studied. Additional details on the trends observed in figure 3.11 are explained in § 4 on the basis of the low-dimensional organized motions of the tip vortex (using POD).

3.3 Low dimensional representation using POD

Lumley's [53] proper orthogonal decomposition is used here to identify the most energetic features of the turbulence fluctuations that reside within the blade tip vortex. The technique has been rigorously exercised in both experimental and numerical disciplines [8]. While it is more customary for one to use the snapshot form of the POD technique [83] described in § 3.3.1 owing to the advantages of its computational efficiency, the classical form is employed here owing to the physical relevance of the Fourier modes and is described in § 3.3.2. Nevertheless, subsequent comparisons between these two forms of POD (applied to the current measurements) are discussed in § 5.

3.3.1 Snapshot POD

The process begins by computing the autocorrelation matrix C,

$$C_{kl}(\psi) = \frac{1}{N_s} \iint_A \left(\vec{u}\left(x\prime, y\prime, t_k, \psi\right) \cdot \vec{u}\left(x\prime, y\prime, t_l, \psi\right)\right) dx\prime dy\prime, \tag{3.10}$$

where $(\cdot)$ is the dot product of two vectors; N_s is the number of instantaneous velocity fields acquired at each vortex age (ψ); $\vec{u}$ is the fluctuating part of the in-plane velocity vector after wander correction; t_k and t_l represent the k^{th} and i^{th} instants of time, respectively. It is evident from Eq. 3.10 that the size of the autocorrelation matrix C depends on the number of instantaneous samples acquired, rather than the number of spatial points in the measurement grid. Following the diagonalisation of the matrix C the eigenpairs (α^f, V^f) are obtained, where $f = 1, 2, ..., N_s$. The eigenvalues α^f are ordered such that

$\alpha^f \geq \alpha^{f+1}$. The corresponding two-dimensional orthogonal spatial modes ($\vec{\mathfrak{U}}^f$) are obtained as

$$\vec{\mathfrak{U}}^f\left(x\prime, y\prime, \psi\right) = \sum_{k=1}^{N_s} V_k^f \vec{u}\left(x\prime, y\prime, t_k, \psi\right), \tag{3.11}$$

which are further normalized to produce the orthonormal basis functions,

$$\vec{\mathfrak{N}}^f\left(x\prime, y\prime, \psi\right) = \frac{\vec{\mathfrak{U}}^f\left(x\prime, y\prime, \psi\right)}{\sqrt{\iint\limits_A \left(\vec{\mathfrak{U}}^f\left(x\prime, y\prime, \psi\right) \cdot \vec{\mathfrak{U}}^f\left(x\prime, y\prime, \psi\right)\right) dx\prime dy\prime}}. \tag{3.12}$$

The contribution of each mode $\vec{\mathfrak{N}}^f$ to the total resolved turbulence kinetic energy of the flow is obtained as

$$\varepsilon^f = \frac{\alpha^f}{\sum\limits_{k=1}^{N_s} \alpha^k}. \tag{3.13}$$

From the orthonormal basic functions in Eq. 3.11, a low-dimensional reconstruction of the velocity field can be obtained from the following expression,

$$\vec{\mathfrak{u}}\left(x\prime, y\prime, t_k, \psi\right) = \sum_{f=1}^{n_s} a_k^f(\psi) \vec{\mathfrak{N}}^f\left(x\prime, y\prime, \psi\right), \tag{3.14}$$

where for $n_s = N_s$, $\vec{\mathfrak{u}} = \vec{u}$; and $a_{k,f}$ is the time varying expansion coefficient, which is derived by projecting the raw velocity field $\vec{u}$ on the orthonormal basic function $\vec{\mathfrak{N}}^f$,

$$a_k^f(\psi) = \iint\limits_A \left(\vec{u}\left(x\prime, y\prime, t_k, \psi\right) \cdot \vec{\mathfrak{N}}^f\left(x\prime, y\prime, \psi\right)\right) dx\prime dy\prime. \tag{3.15}$$

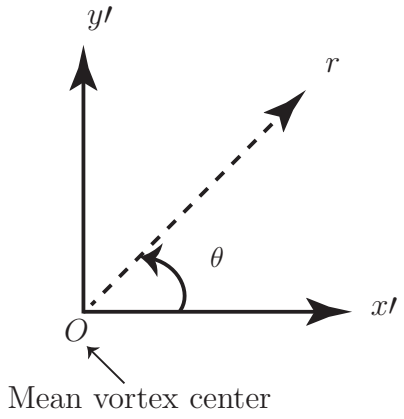

Figure 3.12: Coordinate transformation.

3.3.2 Classical POD

In the current study, the classical form of technique outlined by Glauser and George (1987) [23], Citrinity and George (2000) [13] and Tinney *et al.* (2008) [85] is employed. In this method, the vortex (and its surrounding fluid) is first decomposed in azimuth using Fourier-decomposition followed by a radial decomposition using POD. This is applied to only the fluctuating part of the velocity upon corrections for vortex wander.

The process begins by first transforming the raw PIV images from cartesian coordinates to cylindrical coordinates (i.e. $x\prime,\ y\prime,\ z\prime \rightarrow r,\ \theta,\ z\prime$; see figure 3.12). At each vortex age, the azimuthal grid resolution, $\delta\theta$, is determined such that it equals the resolution of the original grid at $r = r_c$, ($\delta\theta = \tan^{-1}(L_m/(2r_c))$. For example at $\psi = 135°$, $\delta\theta$ is equal to 4° (though it was found to vary only from 3° to 5° over the entire measurement envelope). The fluctuating part of the in-plane velocity field ($u_{i=1,2}$ where $\tilde{u}_i = U_i + u_i$, and $1 = r$ & $2 = \theta$) is then transformed in the azimuthal direction to obtain the

Fourier-azimuthal modes for each of the 350 PIV snap shots at a given vortex age as follows,

$$\hat{u_i}(r,\psi,t;m) = \frac{1}{2\pi}\int_{-\pi}^{\pi} u_i\,(r,\theta,\psi,t)\,e^{-\imath m\theta}\,\mathrm{d}\theta, \tag{3.16}$$

from which a two-point tensor is then formed,

$$B_{ij}(r,r',\psi;m) = \langle \hat{u_i}(r,\psi,t;m)\hat{u_j}^*(r',\psi,t;m)\rangle. \tag{3.17}$$

Here $\langle\ \rangle$ are used to denote ensemble averaging. In Eq. 3.16, the same azimuthal starting position is employed in order to preserve the asymmetries that are shown to reside in the TKE profiles in figures 3.9 and 3.10. Symmetry considerations for statistically axisymmetric flows without swirl are provided in Appendix A of Jung *et al.* (2004) [36]. Here it is assumed that these symmetries cannot be applied. An integral eigenvalue problem is then formed for each vortex age

$$\int_R B_{ij}\,(r,r',\psi;m)\Phi_j^{(n)}\,(r',\psi;m)r'\,\mathrm{d}r' = \Lambda^n\,(\psi;m)\,\Phi_i^{(n)}\,(r,\psi;m), \tag{3.18}$$

and is solved to produce an ordered sequence of eigenvalues ($\lambda^n \geq \lambda^{n+1}$) with eigenfunctions $\Phi_i^n\,(r,\psi;m)$. This vector decomposition ensures that the eigenfunctions corresponding to the in-plane velocity components are coupled. In order to construct the two-dimensional spatial modes that characterize the velocity field, the POD eigenfuctions Φ_i^n and the Fourier eigenfunctions $e^{\imath m\theta}$ are combined as follows,

$$\mathfrak{U}_i^{(m,n)}(r,\theta,\psi) = e^{\imath m\theta}\Phi_i^{(n)}(r,\psi;m). \tag{3.19}$$

Having discretized Eq. 3.18, the total number of POD modes is governed by the product between the number of points measured (N) and the number of in-plane components (η) used to construct B_{ij}. The radial extent is confined to $\sim 2r_c$ at each ψ. And so, given the grid resolution employed here ($L_m/2$; $L_m/r_c < 0.2$), $N > 20$, at least 40 POD modes are generated at each vortex age. Further, the total resolved energy [13, 85] of the flow, $\Pi(\psi)$, and the normalized eigenspectra, $\beta^n(\psi; m)$, are obtained as

$$\Pi(\psi) = \sum_n \sum_m \Lambda^n(\psi; m), \quad \beta^n(\psi; m) = \frac{\Lambda^n(\psi; m)}{\Pi(\psi)} \tag{3.20}$$

While Eq. 3.19 allows one to view the spatial topography of the modes associated with the average turbulence statistics, an instantaneous low-dimensional representation of the fluctuating velocity field can be obtained from the following expressions [53],

$$\hat{\mathfrak{u}}_i(r, \psi, t; m) = \sum_{n=1}^{k} \mathbf{a}^{(n)}(\psi, t; m)\Phi_i^{(n)}(r, \psi; m), \tag{3.21}$$

using uncorrelated and time varying coefficients,

$$\mathbf{a}^{(n)}(\psi, t; m) = \int_R \hat{u}_i(r, \psi, t; m)\Phi_i^{(n)*}(r, \psi; m) r \mathrm{d}r. \tag{3.22}$$

The mean square energy of these coefficients are the eigenvalues themselves: $\lambda^{(n)} = \langle \mathbf{a}^{(n)}\mathbf{a}^{(n)} \rangle$. For $k = \eta N$, $\hat{\mathfrak{u}}_i = \hat{u}_i$. A low-dimensional reconstruction of the fluctuating velocity is then obtained using the following inverse transformation,

$$\mathfrak{u}_i(r, \theta, \psi, t) = \int_m \hat{\mathfrak{u}}_i(r, \psi, t; m)\, e^{im\theta}\, \mathrm{d}m. \tag{3.23}$$

Further, from the low-dimensional fluctuating velocities, the low-dimensional turbulence kinetic energy per unit mass ($\mathfrak{E}$) can be obtained as,

$$\mathfrak{E}\left(r,\theta,\psi\right) = 0.5\langle \mathfrak{u}_1^2 + \mathfrak{u}_2^2 \rangle. \tag{3.24}$$

3.3.2.1 Low dimensional axial vorticity

Given the nature of the flow studied here, it is natural to seek a low-dimensional representation of the axial vorticity field. This is obtained using the following standard expression,

$$\mathfrak{W}_z{}^{(m,n)} = \frac{1}{r}\frac{\partial(r\mathfrak{U}_2{}^{(m,n)})}{\partial r} - \frac{1}{r}\frac{\partial \mathfrak{U}_1{}^{(m,n)}}{\partial \theta}, \tag{3.25}$$

with gradients in r being determined here using a first-order central difference scheme. Contrarily, gradients in θ are derived analytically by the nature of Fourier functions,

$$\frac{\partial \mathfrak{U}_1^{(m,n)}}{\partial \theta} = \imath m e^{\imath m\theta}\Phi_1^{(n)}(r,\psi;m). \tag{3.26}$$

Likewise, the axial vorticity field using the low-dimensional instantaneous fluctuating velocity can be determined by simply replacing $\mathfrak{U}_\mathfrak{i}{}^{(m,n)}$ in Eq. 3.25 with $\mathfrak{u}_\mathfrak{i}$ from Eq. 3.23.

Chapter 4

Low-dimensional characteristics

In this chapter, low-dimensional characteristics of the trailing tip vortices from the rotor are demonstrated using the classical form of POD described in § 3.

4.1 Grid resolution for POD

Prior to the low-dimensional representation of the tip vortex, it is essential to check if the measurements provide sufficient grid resolution to resolve the POD modes. An overly coarse grid results in an underestimation of the POD eigenvalues, whereas a denser grid results in superfluous information, which reduces the computational efficiency of the technique. Following the analysis of Tinney (2009) [86], the sensitivity of the POD eigenvalues to the discretization of the measurement domain is performed, where the velocity measurements (of the original grid, $L_m/2$) are projected (by a linear interpo-

This chapter may compose material from the author's previously published articles,

S. M. Mula and C. E. Tinney. A study of the turbulence within a spiralling vortex filament using proper orthogonal decomposition. *J. Fluid Mech.*, 769: 570–589, 2015. For this project, Tinney served as the project advisor.

S. M. Mula and C. E. Tinney. Classical and Snapshot forms of the POD technique applied to a helical vortex filament. *AIAA Paper* 2014-3257, 2014. For this project, Tinney served as the project advisor.

lation) onto a series of grids with increasing coarseness. The differences in the resulting eigenvalues from that of the original grid ($L_m/2$) are estimated,

$$\epsilon_p^n(\psi) = \frac{\sum_m {\Lambda_p}^n(\psi;m) - \sum_m \Lambda^n(\psi;m)}{\sum_m \Lambda^n(\psi;m)}. \tag{4.1}$$

In Eq. 4.1 Λ^n and ${\Lambda_p}^n$ represent the eigenvalues of the original and projected grids, respectively; $\sum_m {\Lambda_p}^n(\psi;m)$ represents the total energy (contains all the Fourier modes) of the n^{th} POD mode. Figure 4.1a,b,c illustrates the convergence in the first, second and third POD modes, respectively, for sample ψ. It is evident that a significant convergence is achieved for the original grid resolution ($\Delta r = L_m/2; L_m/2r_c < 0.1$) for $n = 1, 2$ and 3.

4.2 Energy spectrum

Following the application of the classical form of POD to the current set of measurements, an illustration of the POD energy spectrum is shown in figure 4.2a for sample vortex ages in the measurement envelope (where each POD mode in this figure contains all the Fourier modes). Convergence of the POD modes is evident in figure 4.2a with approximately 75% of the resolved energy residing in the first ($n = 1$) POD mode for the entire range of ψ studied here. Given the spatial resolution used to generate B_{ij}, this rapid convergence is a reflection of the organized motions that characterize the active motions of this vortex filament, as opposed to numerical integration errors [85,86]; similar rates of convergence were found at other vortex ages. Further, figure 4.2b

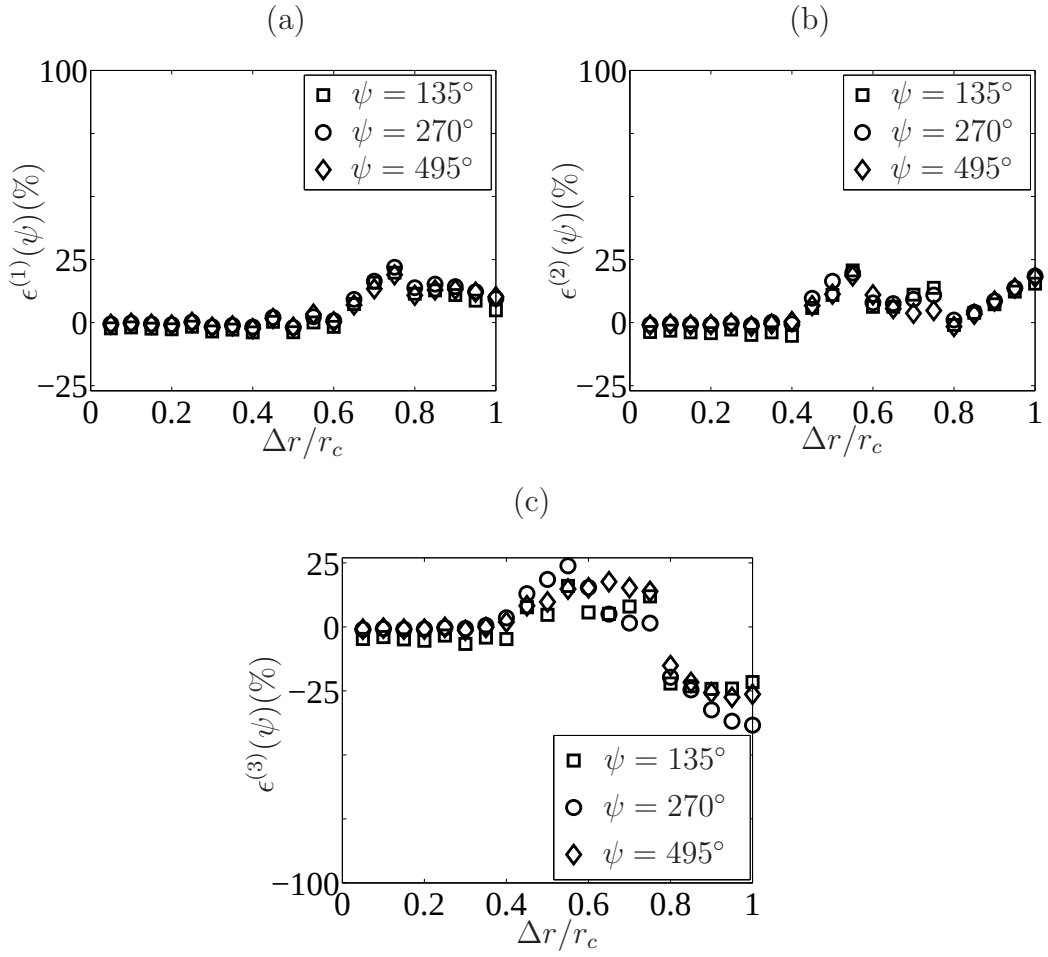

Figure 4.1: Sensitivity of the POD eigenvalues to the grid resolution $\Delta r/r_c$. (a) $n = 1$, (b) $n = 2$, and (c) $n = 3$.

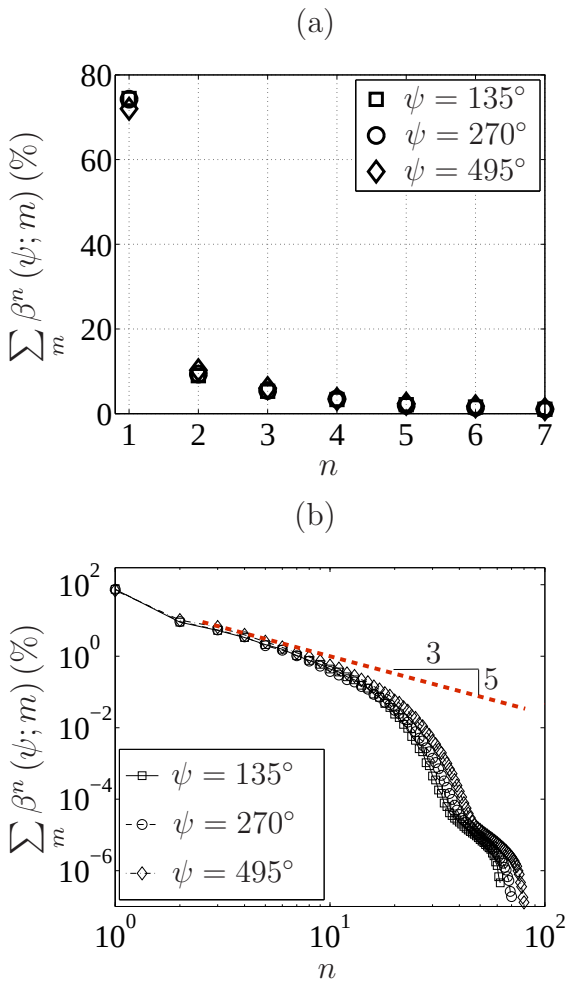

Figure 4.2: (a) Energy spectra of the first seven POD modes. (b) Energy spectra of the POD modes on a logarithmic scale.

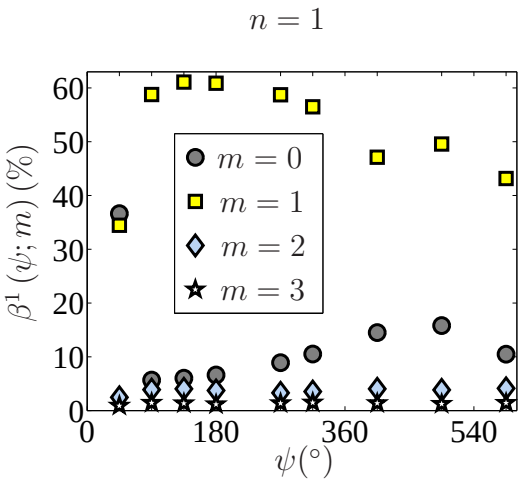

Figure 4.3: Fourier mode energy spectra of the first ($n = 1$) POD mode for $m = 0$, 1, 2 and 3.

illustrates the POD energy spectrum on a logarithmic scale. Here in the first decade of the POD modes, the energy spectrum appears to exhibit a $k^{-5/3}$ inertial range that is expected even for an inhomogeneous turbulent flow at high Reynolds numbers [62].

Since 75% of the resolved energy that is shown to reside in the first POD mode in figure 4.2*a* is distributed amongst the Fourier modes, figure 4.3 illustrates the Fourier energy spectrum for this first POD mode. It is evident that the helical mode ($m = 1$) dominates the energy spectrum ($> 40\%$) at all the vortex ages followed by the axisymmetric ($m = 0$) and double helical modes ($m = 2$). However, at $\psi = 45°$, both the axisymmetric and helical modes are equally imperative and is attributed to the roll-up of the vortex at the blade tip, which will be demonstrated shortly in the following section.

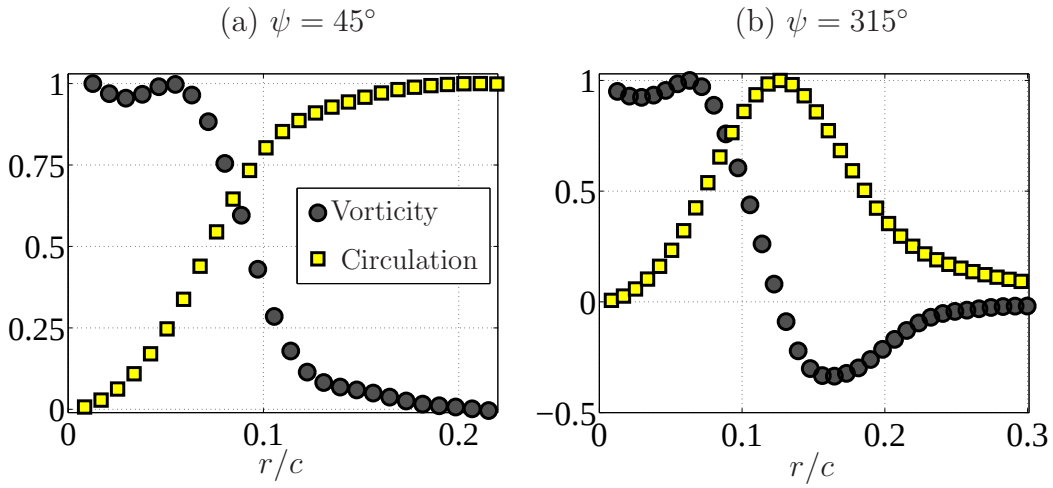

Figure 4.4: Radial profiles of vorticity and circulation profiles for $(m, n) = (0, 1)$ at (a) $\psi = 45°$ and (b) $\psi = 315°$.

4.2.1 Spatial structures of the Fourier modes of the first POD mode ($n = 1$)

In this section, the spatial structures of the axisymmetric ($m = 0$), helical ($m = 1$) and double helical ($m = 2$) modes associated with the first ($n = 1$) POD mode are presented. These structures are obtained using Eq. 3.19 and Eq. 3.25.

Where the axisymmetric mode is concerned, the radial profiles of circulation and axial vorticity are shown in figure 4.4a for $\psi = 45°$. These profiles reflect that of a vortex with viscous core (see Han *et al.* (1997) [27], Bhagwat & Leishman (2000) [10] and Ramasamy *et al.* (2007) [73]), in which the circulation at the vortex center is zero and increases radially outward and then remains constant in the inviscid region. Therefore, the axisymmetric mode is associated with the roll-up of the vorticity-sheet trailed from the rotor blade

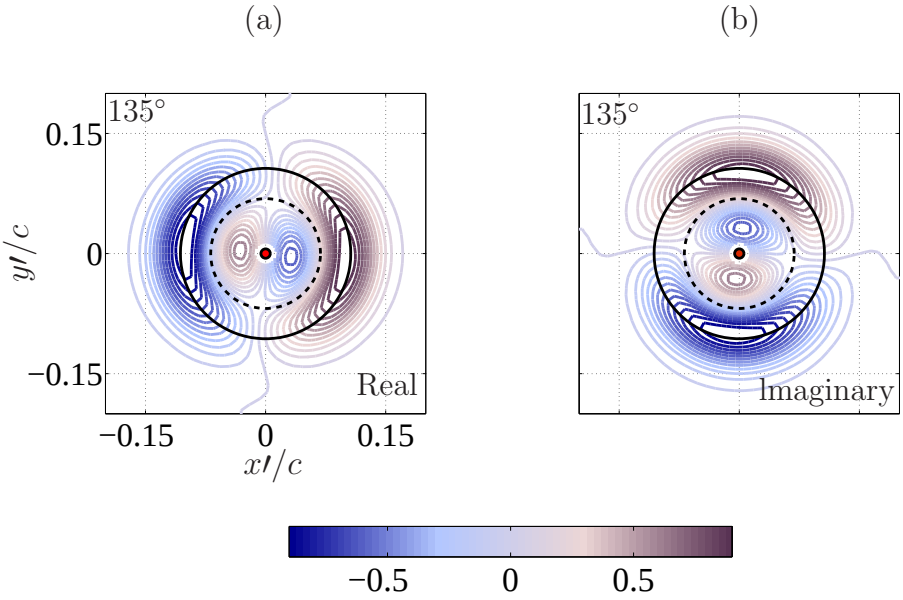

Figure 4.5: Contours of the (a) real and (b) imaginary components of the axial vorticity of the helical mode $(m, n) = (1, 1)$ at $\psi = 135°$. Circles of mean core-radius (__) and peak TKE (....) are indicated.

at early ages. However, at $\psi = 315°$ in figure 4.4b (after the roll-up process is complete) circulation and vorticity profiles associated with the axisymmetric mode manifest the kinds of behaviors observed in swirling jet flows (see Liang & Maxworthy (2005) [52]). In a swirling jet, the circulation is zero at $r = 0$ and increases radially outward until it peaks and then drops down to zero. The presence of this swirling jet mode reinforces flow-entrainment and diffusion mechanisms, which is shown in figure 4.3b to increase in energy from 5% (at $\psi = 90°$) to about 15% (at $\psi = 495°$).

Due to the nature of Fourier functions, non-zero Fourier modes like the helical ($m = 1$) or double helical modes ($m = 2$), comprise both real and imag-

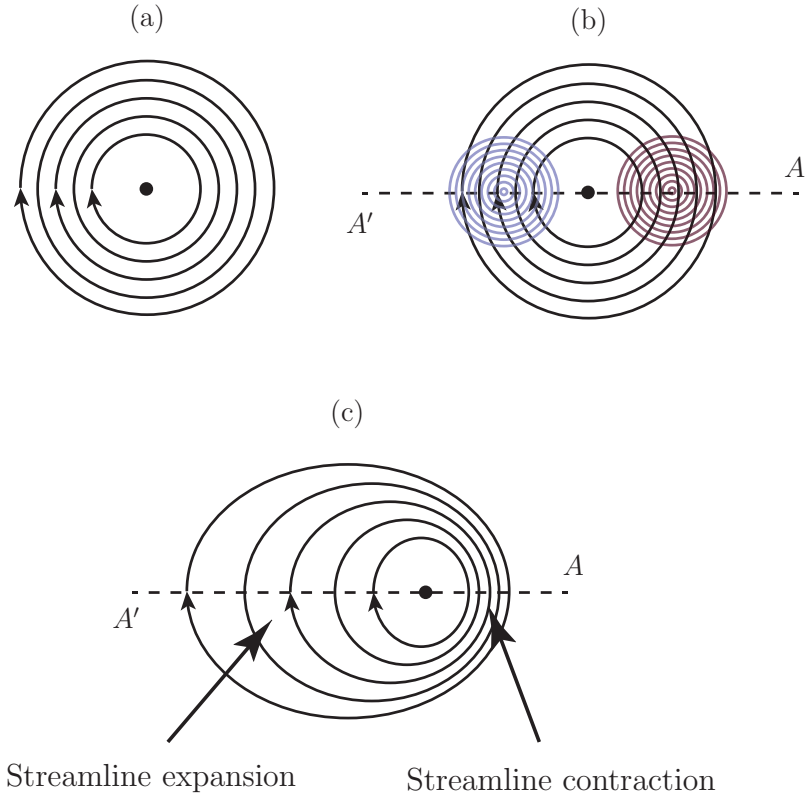

Figure 4.6: Schematic of a helical mode of the elliptic instability. (a) Base flow with circular streamlines, (b) application of the helical mode to the base flow, and (c) resultant flow of elliptical streamlines.

inary components. Figure 4.5 shows the real component of the axial vorticity of the helical mode at a sample vortex age ($\psi = 135°$). The spatial structure of the imaginary component is identical to its real counterpart, except that it is oriented at $\pi/(2m) = 90°$ (anti-clockwise) relative to its real counterpart.

To better understand the effect of the helical mode in figure 4.5 on the base vortex flow, consider the schematic shown in figure 4.6. To help

with the interpretation, consider the base vortex flow composed of circular streamlines as demonstrated in figure 4.6a. To this base vortex flow apply a helical mode that comprises only a single pair of counter-rotating eddies (see figure 4.6b); these eddies are represented by their axial vorticity field following the color convention used in figure 4.5 (blue-clockwise; red-anticlockwise). As a consequence, the resultant vortex flow is deformed. Given the sense of direction of the circular streamlines (figure 4.6a), the clockwise and anticlockwise eddies of the helical mode cause an expansion and contraction of the streamlines of the base vortex flow, respectively (figure 4.6c); hence, the resultant streamlines are elliptical streamlines. Further, as an extension to the schematic in figure 4.6, consider the schematic illustrated in figure 4.7. The schematic (figure 4.7) demonstrates the effect of the helical mode, which consists of two pairs of counter-rotating eddies, similar to that in figure 4.5. Once again, the clockwise and anticlockwise eddies of the helical mode cause an expansion and contraction of the streamlines of the base vortex flow, respectively (figure 4.7c). As a consequence, the resultant streamlines are once again elliptically deformed. Such an elliptical deformation of the base vortex (figures 4.6c and 4.7c) is a characteristic of the elliptic instability, which is a three-dimensional short-wave instability that travels along the vortex filament. Therefore, the helical mode in figure 4.5 is a mode associated with the elliptic instability and the structure of this helical mode is similar to the spatial structures of the elliptic instability modes observed by Pierrehumbert (1986) [67], Leweke & Williamson (1998) [46], and Sipp (2000) [82] (see fig-

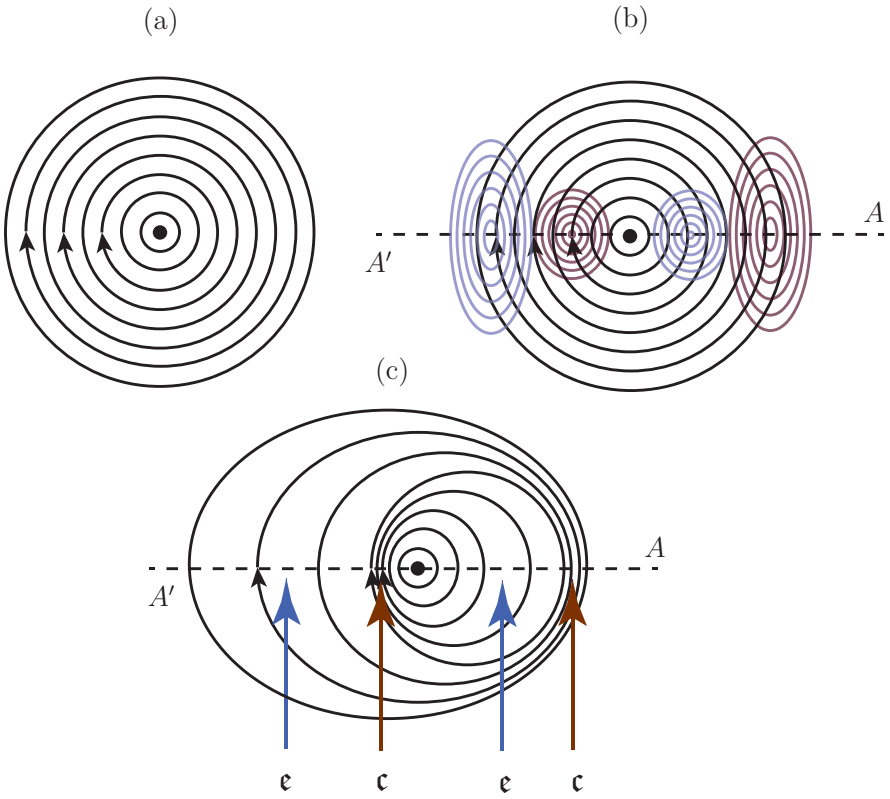

Figure 4.7: Schematic of a helical mode of the elliptic instability. (a) Base flow with circular streamlines, (b) application of the helical mode to the base flow, and (c) resultant flow of elliptical streamlines with expansion ($\mathfrak{e}$) and contraction ($\mathfrak{c}$) of streamlines

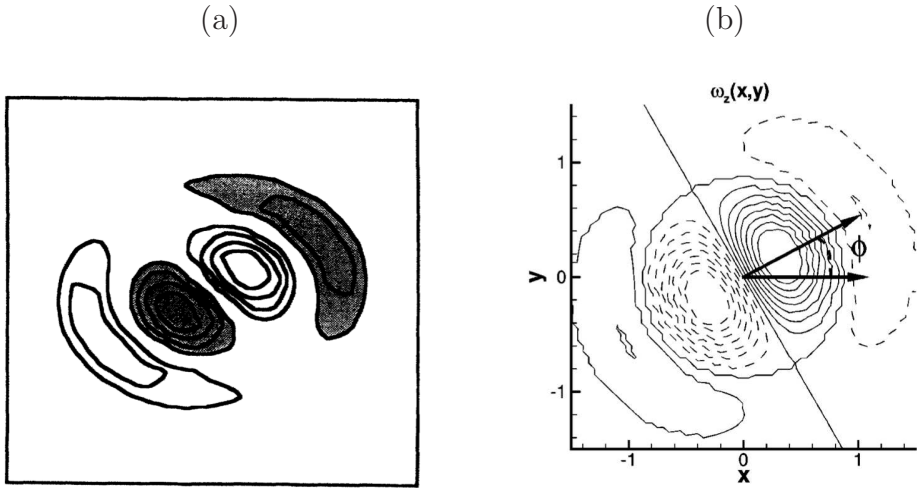

Figure 4.8: Axial vorticity contours of the modes of the elliptic instability observed by (a) Pierrehumbert (1986) [67] and (b) Sipp (2000) [82].

ure 4.8). For a comprehensive review on the elliptic instability see § 1.3.1. Furthermore, Laceze *et al.* (2007) [41] showed how the most unstable modes of the elliptic instability correspond to $|m| = 1$ (helical mode) when the axial velocity strength W_0 (ratio of maximum swirl velocity to the maximum azimuthal velocity) is low. Here, the axial velocity strength is estimated to be $W_0 = 0.159$ (using the axial velocity data from Mula *et al.* (2013) [64]), which is sufficiently low, and see from figure 4.3 that the helical mode dominates the energy spectrum of the vortex filament. And so, the helical mode is the most unstable mode of the elliptic instability in the current study.

In order to study the evolutionary behavior of this helical mode, its real component is shown in figure 4.9 over the range of vortex ages measured. At the earliest vortex age, $\psi = 45°$, two counter-rotating eddies are manifest

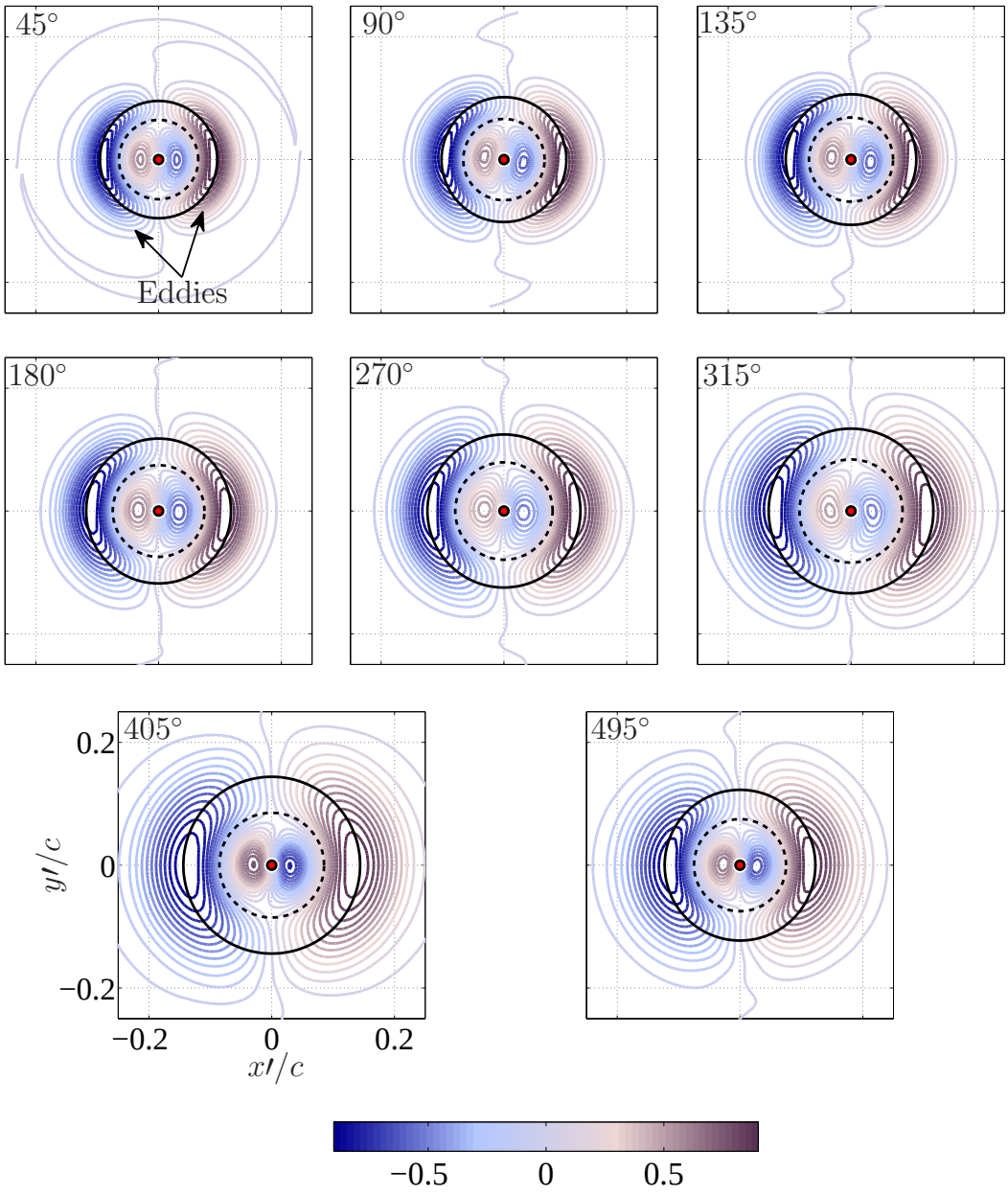

Figure 4.9: Contours of the real component of the axial vorticity of the helical mode $(m, n) = (1, 1)$ at $\psi = 45° - 495°$. Circles of mean core-radius (__) and peak TKE (....) are indicated.

which reside on the circle of mean core-radius. These eddies remain centered on the mean core-radius for all vortex ages without modifying the structure of the helical mode. Likewise, the size of these eddies increases as the core-radius increases. Therefore, the helical mode of the elliptic instability in figure 4.9 is shown to be in the linear regime, since in the non-linear regime such an instability mode would undergo either a rotation [82] or a modification in its structure [80] (which is not observed here). A review on the non-linear aspects of the elliptic instability is given in § 1.3.1. Furthermore, where short-wave instabilities are concerned, Hattori & Fukumoto (2009, 2014) [29, 30] have shown how torsion produces a second-order correction to the growth rate of the curvature instability, which is first order in ϵ (the ratio of core-radius to curvature radius). From this, it can be inferred that torsion also influences the growth-rate of the elliptic instability which is of $O(\epsilon^2 \log(1/\epsilon))$ [19, 30]. Given the amount of torsion in the current set of measurements ($\hat{\tau} = 0.046$), the most unstable mode of elliptic instability (the helical mode) is shown to be in the linear regime for the entire range of vortex ages studied. It is postulated that by reducing the amount of torsion (of the helix), non-linearities will develop in this most unstable mode, and will accelerate the breakdown of the tip vortex structure [46, 80].

While the evolutionary characteristics of the dominant mode of the elliptic instability are demonstrated, it would be interesting to see how this mode might reveal itself in an instantaneous sense for the current set of measurements. Therefore, a low-dimensional reconstruction of the instantaneous

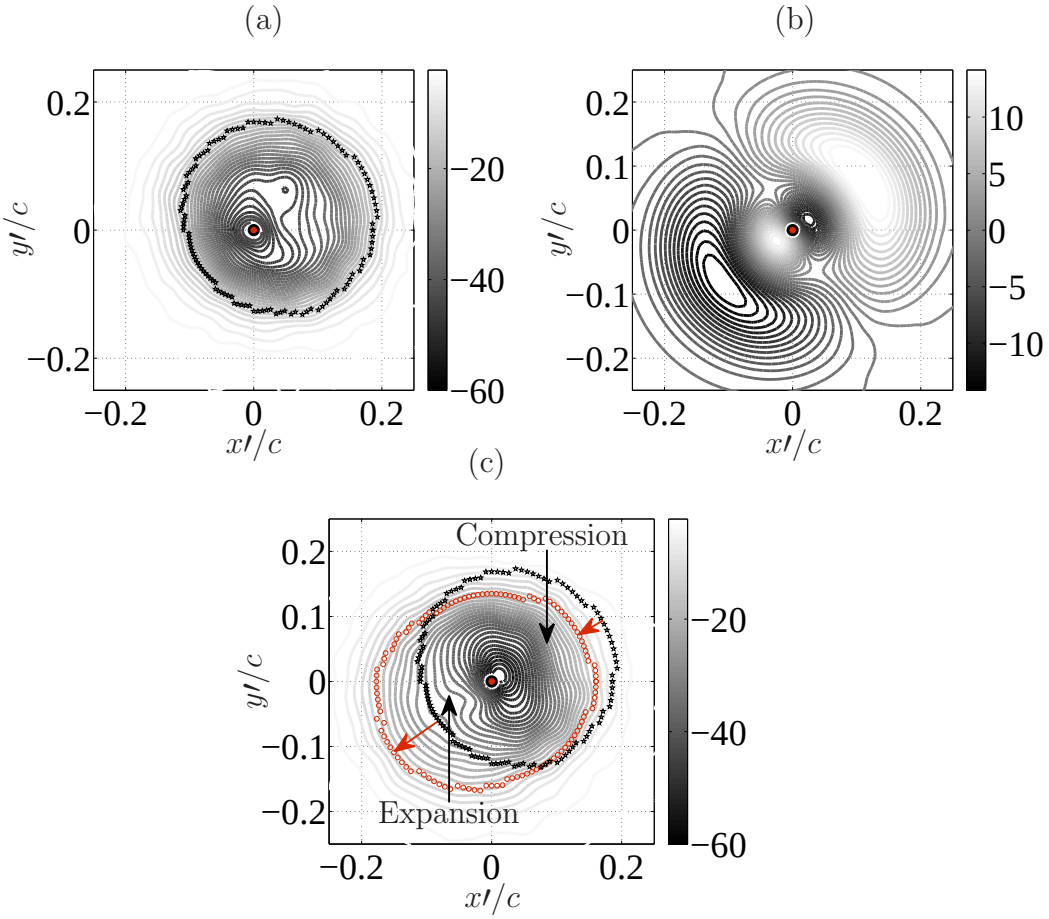

Figure 4.10: (a) Mean axial vorticity (ω_z/Ω), (b) reconstruction of the fluctuating vorticity at an instant in time using $(m, n) = (1, 1)$, (c) mean vorticity plus the $(1, 1)$ mode at $\psi = 405°$. Core-boundaries for the mean (black) and low-dimensional (red) vortices also indicated.

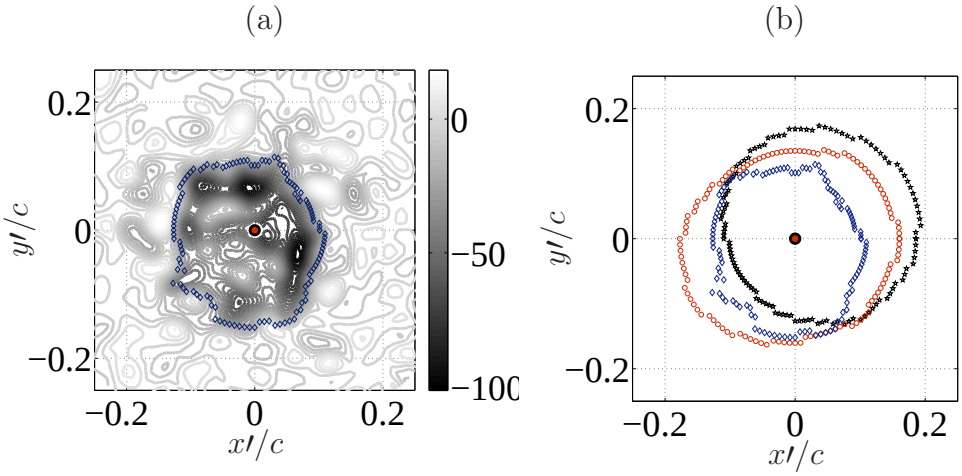

Figure 4.11: (a) Original instantaneous vorticity at an instant in figure 4.10 and (*b*) the corresponding core-boundaries for the mean (figure 4.10a), low-dimensional (figure 4.10b) and original instantaneous vortices for a sample set of data at $\psi = 405°$. Mean (black), low-dimensional (red) and instantaneous (blue) core boundaries.

vorticity field using $(m, n) = (1, 1)$ at $\psi = 405°$ is shown in figure 4.10c. This is performed by combining the average vorticity field at that vortex age (figure 4.10a) with an instantaneous sample of the low-dimensional fluctuating vorticity field (figure 4.10b). The boundaries of the vortex core associated with the mean flow (figure 4.10a) are shown in figure 4.10c alongside the boundaries of the vortex core with the effects imposed by the addition of a low-dimensional vorticity field (figure 4.10b). The discrepancies between these boundaries coincide with the compression and expansion of contour lines, which is typical of the elliptic instability; the inward radial displacement of the instantaneous boundary (from the mean) causes streamline-compression, while the outward displacement causes streamline-expansion [46]. Figure 4.11a shows the raw instantaneous vorticity field (without the mean subtracted), which corresponds

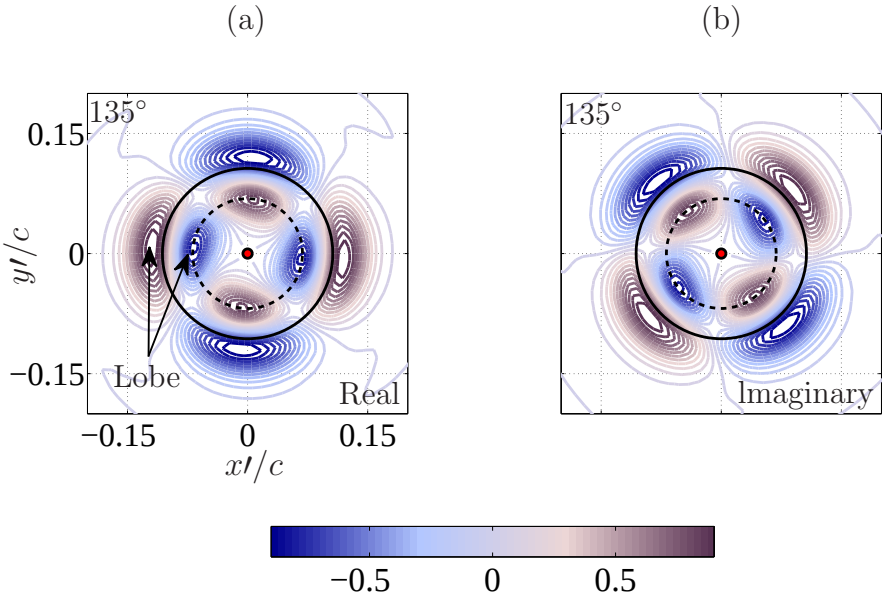

Figure 4.12: Contours of the (a) real and (b) imaginary components of the axial vorticity of the double helical mode $(m, n) = (1, 1)$ at $\psi = 135°$. Circles of mean core-radius (__) and peak TKE (....) are indicated.

to the same instant as that of the low-dimensional sample in figure 4.10c. The core-boundaries of the mean, low-dimensional and raw samples are illustrated in figure 4.11b (black, red and blue, respectively). The discrepancies between the core-boundaries of the low-dimensional (red) and raw samples (blue) are attributed to the energies that reside in higher POD and Fourier modes.

As for the double-helical mode ($m = 2$), figure 4.12 illustrates the real and imaginary components of the axial vorticity field at a sample $\psi = 135°$. Once again, their structures are identical and differ in orientation by $\pi/(2m) = 45°$ due to the nature of Fourier functions. The structure of this double helical mode is four-lobed in azimuth with each lobe containing a pair of counter-

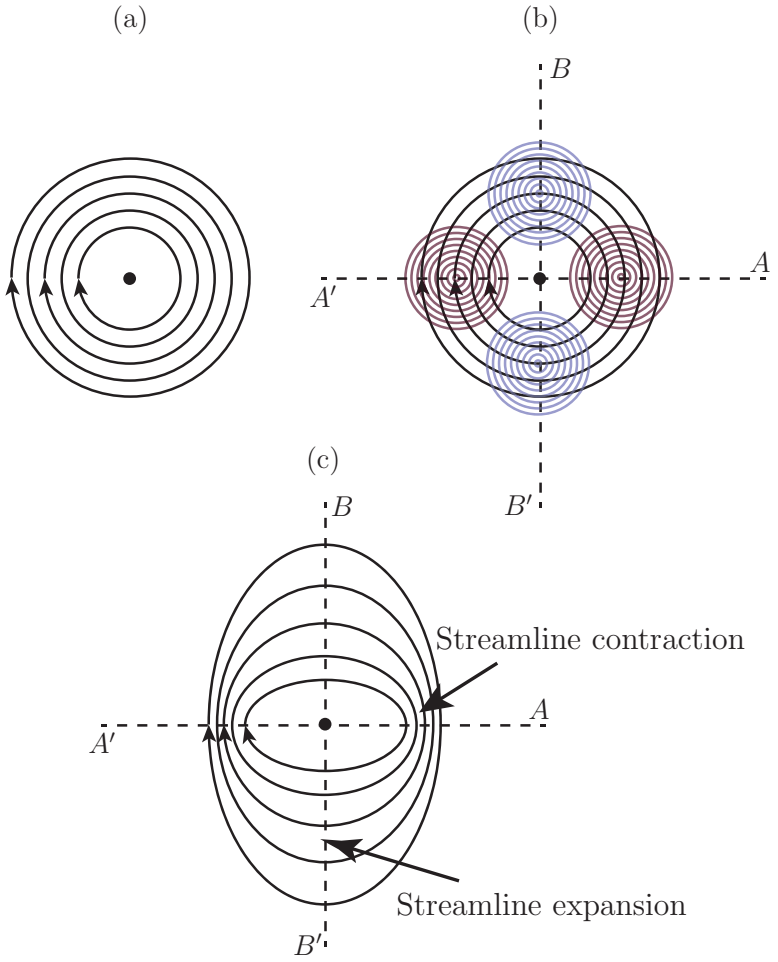

Figure 4.13: Schematic of a double helical mode of the elliptic instability. (a) Base flow with circular streamlines, (b) application of the double helical mode to the base flow, and (c) resultant flow of elliptical streamlines.

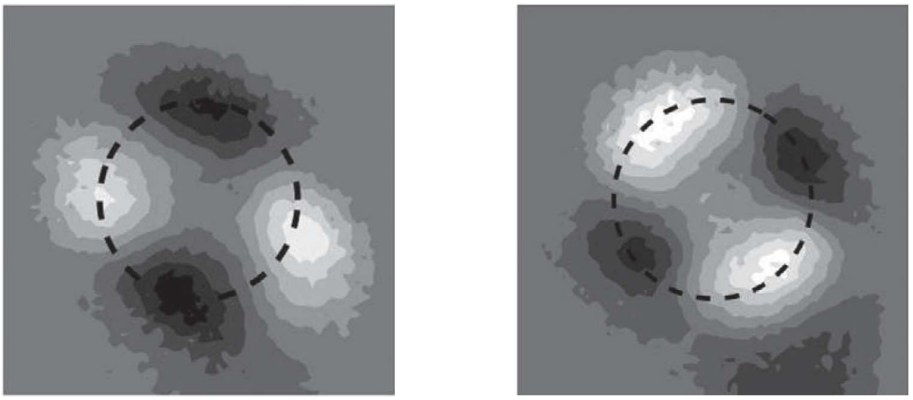

Figure 4.14: Light intensity of the four-lobed structures of the double helical mode of the elliptic instability from the findings of Roy *et al.* (2011) [79].

rotating eddies, which are radially separated. In order to demonstrate the role of this double-helical mode ($m = 2$), consider the schematic shown in figure 4.13, which is similar to the schematic shown in figure 4.6 for the helical mode, where the base vortex flow with circular streamlines (see figure 4.13a) is considered. On the application of a simple four-lobed double helical mode (represented by its axial vorticity field in figure 4.13b), with each lobe containing only a single eddy, the resultant flow is deformed (figure 4.13c). Once again, the clockwise (blue) and anticlockwise (red) eddies of this mode cause an expansion and contraction of the streamlines of the base vortex flow, respectively (figure 4.13c). As a consequence, the streamlines are again elliptically deformed. It is deduced that the double helical mode in figure 4.12 also causes an elliptical deformation of the streamlines of the base vortex flow. Therefore, this mode is also associated with the elliptic instability. A four-lobed structure of such an instability mode was also observed by Roy *et al.* (2011) (see

figure 4.14) in tip vortices from a fixed wing.

As for the evolutionary behavior of the double-helical mode over the range of vortex ages studied here, the spatial structure of the mode increases in size as the core-radius increases. Further, pairs of co-rotating eddies indicated in figure 4.15 at $\psi = 90°$ appear to merge with the increasing vortex age, thereby slightly modifying the structure of the double-helical mode. At $\psi = 495°$, a single elongated eddy appears to have formed from each such pair. In a non-linear regime an elliptic instability mode undergoes a rotation [82] or a modification in its structure [80]. Therefore, the double-helical mode of the elliptic instability in figure 4.15 is in a slightly non-linear regime, unlike the helical mode which was in the linear regime (figure 4.9).

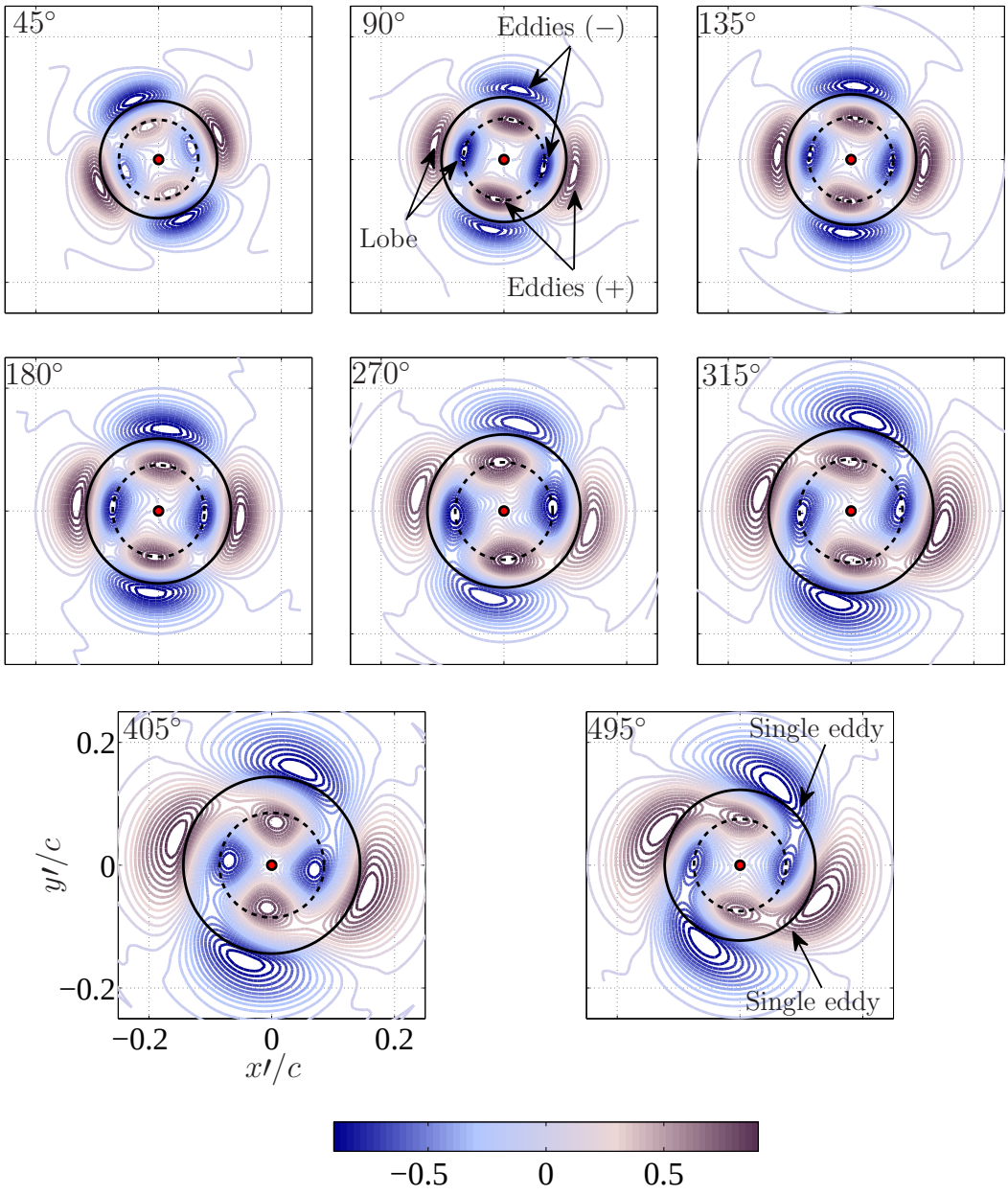

Figure 4.15: Contours of the real component of the axial vorticity of the double helical mode $(m, n) = (2, 1)$ at $\psi = 45° - 495°$. Circles of mean core-radius (__) and peak TKE (....) are indicated.

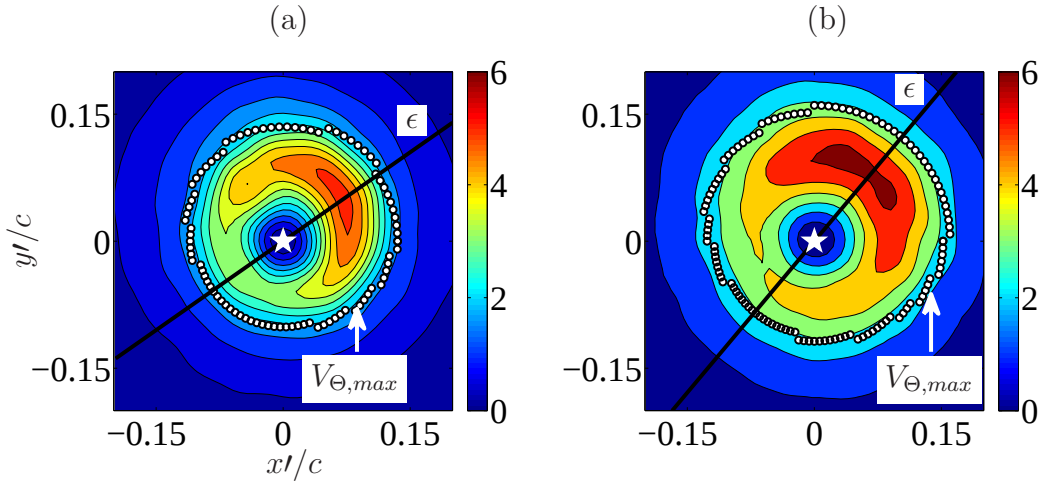

Figure 4.16: Turbulence kinetic energy per unit mass, $(\text{TKE}/V_{tip}^2)\times 10^3$, at (a) $\psi = 180°$ and (b) $\psi = 315°$. Vortex core boundary identified by the locations of peak swirl velocity ($V_{\Theta,max}$) also identified.

4.2.1.1 Asymmetries in the vortex filament

An interesting question that remains to be addressed is which mode, or combinations of modes, is responsible for producing asymmetries in the turbulence kinetic energy per unit mass (TKE) in the plane perpendicular to the vortex filament axis. See figure 4.16a, b (duplication of findings in figure 3.9), which shows that the TKE is asymmetric inside the vortex core at sample $\psi = 180°$ and 315°, respectively. In order to address the above question, a low-dimensional reconstruction of the turbulence kinetic energy per unit mass ($\mathfrak{E} = 0.5\langle \mathfrak{u}_1^2 + \mathfrak{u}_2^2\rangle$ with $\mathfrak{u}_{i=1,2}$ being the in-plane low-dimensional fluctuating velocity obtained from Eq. 3.23) using the axisymmetric, helical and double helical modes associated with the first POD mode, on a vortex slice (ϵ) at a sample $\psi = 180°$ and 315°, is shown in figure 4.17a, b, respectively. A slice of

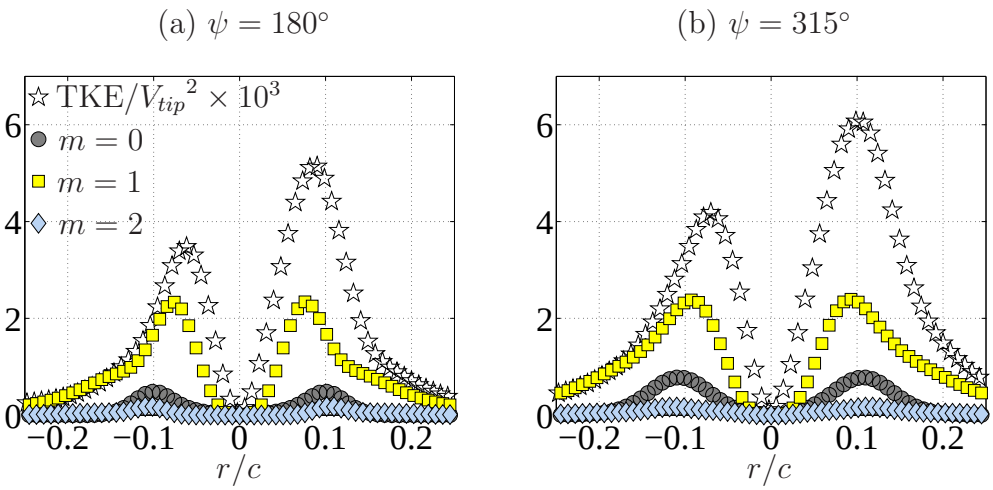

Figure 4.17: $(\mathfrak{E}/V_{tip}^2) \times 10^3$ constructed using the individual Fourier modes for the first $(n = 1)$ POD mode at (a) $\psi = 180°$ and (b) $\psi = 315°$ on a vortex slice.

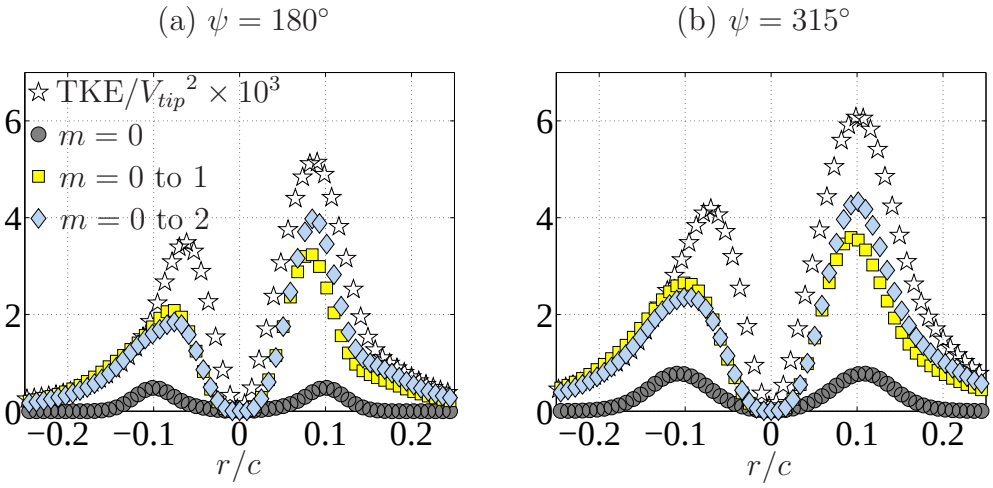

Figure 4.18: $(\mathfrak{E}/V_{tip}^2) \times 10^3$ constructed using the combinations of Fourier modes for the first $(n = 1)$ POD mode at (a) $\psi = 180°$ and (b) $\psi = 315°$ on a vortex slice.

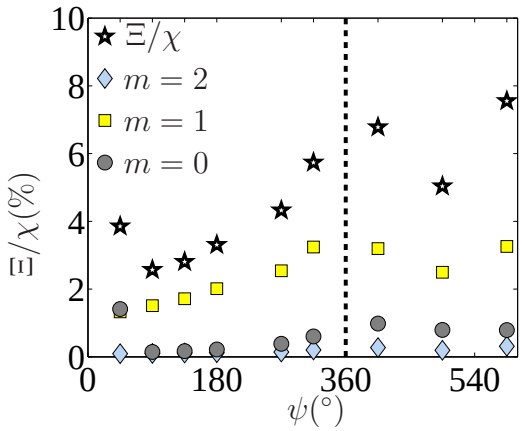

Figure 4.19: Total resolved turbulence kinetic energy (Ξ) normalized with the total resolved kinetic energy (χ) of the flow. Contributions from the axisymmetric ($m = 0$), helical ($m = 1$) and double helical ($m = 2$) modes for the first ($n = 1$) POD mode relative to the mean kinetic energy (χ) of the flow also indicated.

the original TKE is also shown; once again, the TKE is clearly asymmetric. Where the individual modes are concerned, the slices in figure 4.17 appear symmetric. However, in figure 4.18, where $\mathfrak{E}$ is constructed using the first two ($m = 0$ to 1) and the first three ($m = 0$ to 2) Fourier modes, the $\mathfrak{E}$ is shown to comprise asymmetries. Thus, it is evident here how a combination of at least the axisymmetric, helical and double helical modes are responsible for the significant distinguishable asymmetries in the turbulence kinetic energy (per unit mass) inside the tip vortex.

At this point it is also worth addressing the trends observed earlier (figure 3.11) in the total resolved turbulence kinetic energy (Ξ) relative to the kinetic energy of the mean flow (χ), based on the above low-dimensional features of the tip vortex derived. A duplication of these trends is shown

in figure 4.19, along with the individual contributions from the axisymmetric, helical and double helical modes (for the first POD mode) relative to the kinetic energy of the mean flow. Once again, Ξ is on the order of $2-8\%$ of χ over the range of vortex ages studied. However, Ξ/χ at $\psi = 45^\circ$ is distinguishably greater than that at 90°. As the axisymmetric mode is the only mode that shows a similar trend in figure 4.19, this behavior is attributed to the vortex roll-up that occurs at early ages. Further, the turbulence inside the vortex (of vortex Reynolds number, Γ_v/ν, in the range between 8.3 $\times 10^4$ and 8.7×10^4 over the vortex ages studied) increases as the vortex age increases. However, the Ξ/χ (along with the energy contributions from other organized motions) is discontinuous around $\psi = 360^\circ$ due to the first blade passage.

4.2.2 Spatial structures of the Fourier modes for the second POD mode

In this section, non-linearities in the helical ($m = 1$) and double helical ($m = 2$) modes are demonstrated for the second POD mode ($n = 2$). Figure 4.20 illustrates the Fourier energy spectrum for $n = 2$. The helical mode contributes about $3-6\%$ of the resolved energy, and the double helical mode contributes about $2-3\%$ of the resolved energy for the range of vortex ages studied.

The real component of the axial vorticity field of the helical mode is illustrated in figure 4.21. It is clear that the structure of the helical mode is deforming with the increasing age with low-vorticity fluid stripping azimuthally

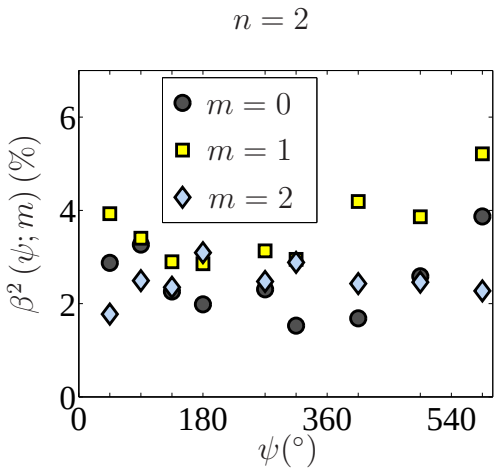

Figure 4.20: Fourier energy spectrum: $m = 0$, 1, and 2 for the second POD mode ($n = 2$).

and radially outward from the two-counter rotating eddies. Fluid stripping is indicated at $\psi = 90°$. It is postulated that the stripped fluid (see at $\psi = 135°$) moves radially away from the vortex axis and breaks down into small scales. Further, there also appears to be a change in the orientation of the eddies at later ages ($\psi > 315°$). Hence, the helical mode of the elliptic instability appears to be in a non-linear regime for the second POD mode ($n = 2$), unlike the linear behavior observed for $n = 1$.

Evolution of the spatial mode of the double-helical mode ($m = 2$) is illustrated in figure 4.22. The double helical mode also demonstrates fluid-stripping. Fluid appears to begin striping at $\psi = 90°$ azimuthally and radially outward from the eddies shown in figure 4.22 and the process continues until $\psi = 495°$.

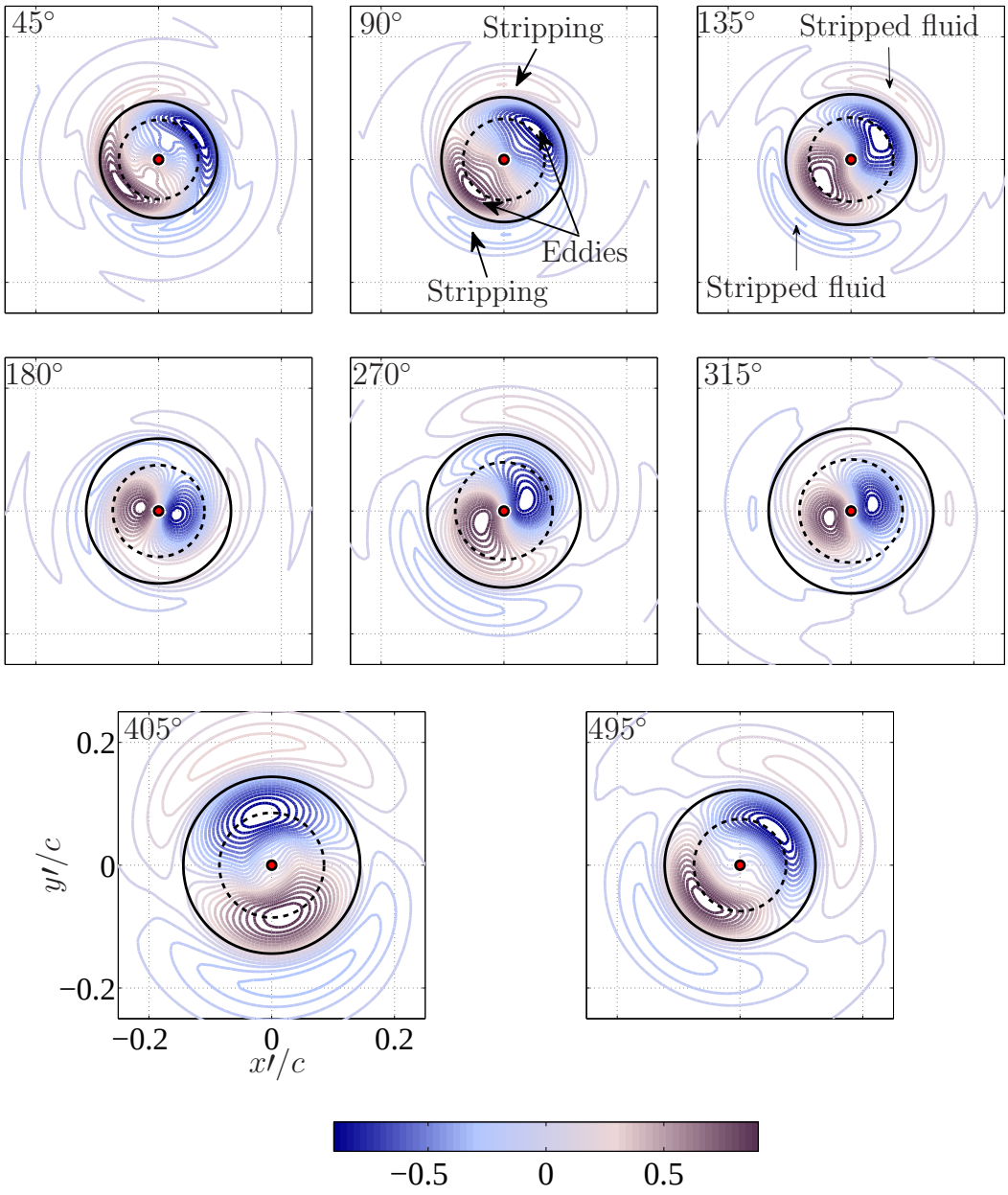

Figure 4.21: Contours of the real component of the axial vorticity of the helical mode $(m, n) = (1, 2)$ at $\psi = 45° - 495°$. Circles of mean core-radius (__) and peak TKE (....) are indicated.

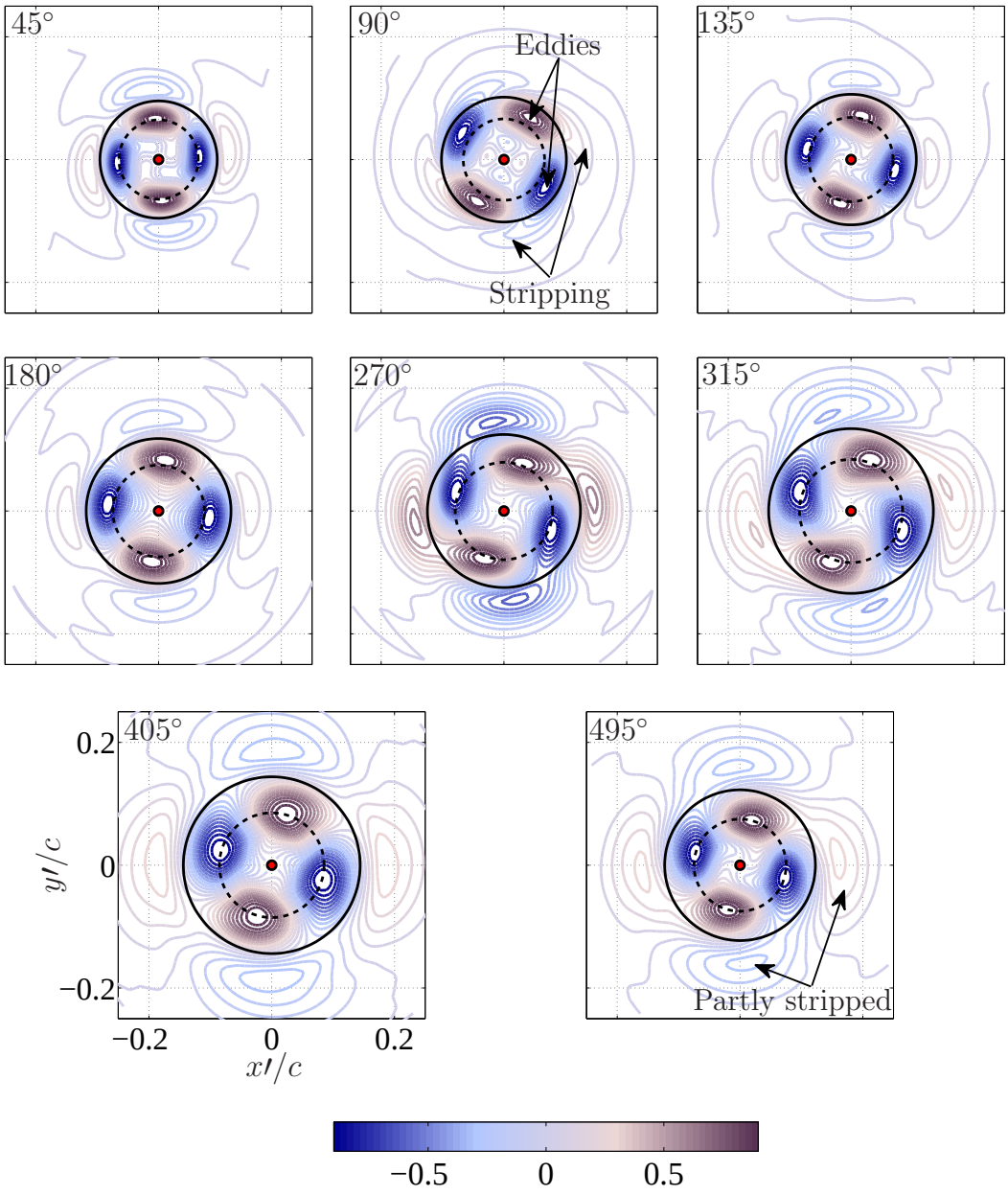

Figure 4.22: Contours of the real component of the axial vorticity of the helical mode $(m, n) = (1, 2)$ at $\psi = 45° - 495°$. Circles of mean core-radius (__) and peak TKE (....) are indicated.

Chapter 5

Comparisons between classical and snapshot forms of POD applied to spiraling vortex filament

Based on the understanding of the low-dimensional features of the tip vortex observed using the classical POD in § 4, subsequent comparisons with that of the snapshot POD which is computationally more efficient are provided in this chapter.

5.1 Energy spectrum and organized motions

As it was demonstrated earlier in § 4.2, given the resolution of the spatial grid in the current setup, the POD modes of the classical technique manifested a rapid convergence in energy with approximately 75% of the energy residing in the first POD mode ($n = 1$) alone. With regard to the snapshot technique, figure 5.1a, b illustrates the energy spectra at two sample vortex

This chapter may compose material from the author's previously published articles,
S. M. Mula and C. E. Tinney. A study of the turbulence within a spiralling vortex filament using proper orthogonal decomposition. *J. Fluid Mech.*, 769: 570–589, 2015. For this project, Tinney served as the project advisor.
S. M. Mula and C. E. Tinney. Classical and Snapshot forms of the POD technique applied to a helical vortex filament. *AIAA Paper* 2014-3257, 2014. For this project, Tinney served as the project advisor.

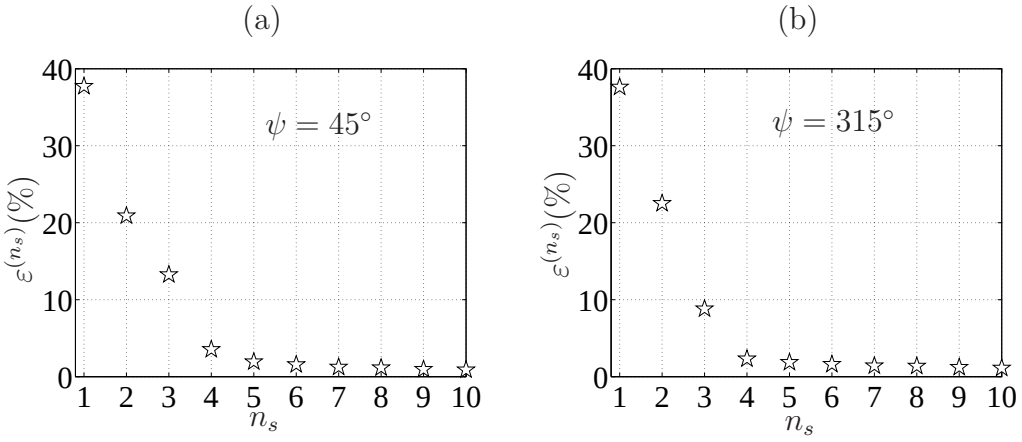

Figure 5.1: Energy spectra of the first ten POD modes of the snapshot technique at (a) $\psi = 45°$ and (b) $\psi = 315°$.

ages $\psi = 45°$ and 315°, respectively, with only the first ten, out of a total of 350 POD modes, being shown. Once again, a rapid convergence in energy is evident here where the first three ($n_s = 1$, 2 and 3) POD modes of the snapshot technique together contain approximately 70% of the resolved energy, which again reflects the presence of highly organized motions within the tip vortex filament. Similar convergence behavior is observed at other vortex ages in the measurement envelope (not shown here).

As for the spatial structures of these first three ($n_s = 1$, 2 and 3) dominant modes, figures 5.2 and 5.3 demonstrate at two sample vortex ages $\psi = 45°$ and 315°, respectively, alongside comparisons with the counterparts of these modes in the classical POD. At $\psi = 45°$, the first mode $n_s = 1$ is expressed by way of its radial profile of circulation, which resembles that of a vortex with viscous core (see Han *et al.* (1997) [27], Bhagwat & Leishman (2000) [10] and Ramasamy *et al.* (2007) [73]), and it forms the counterpart

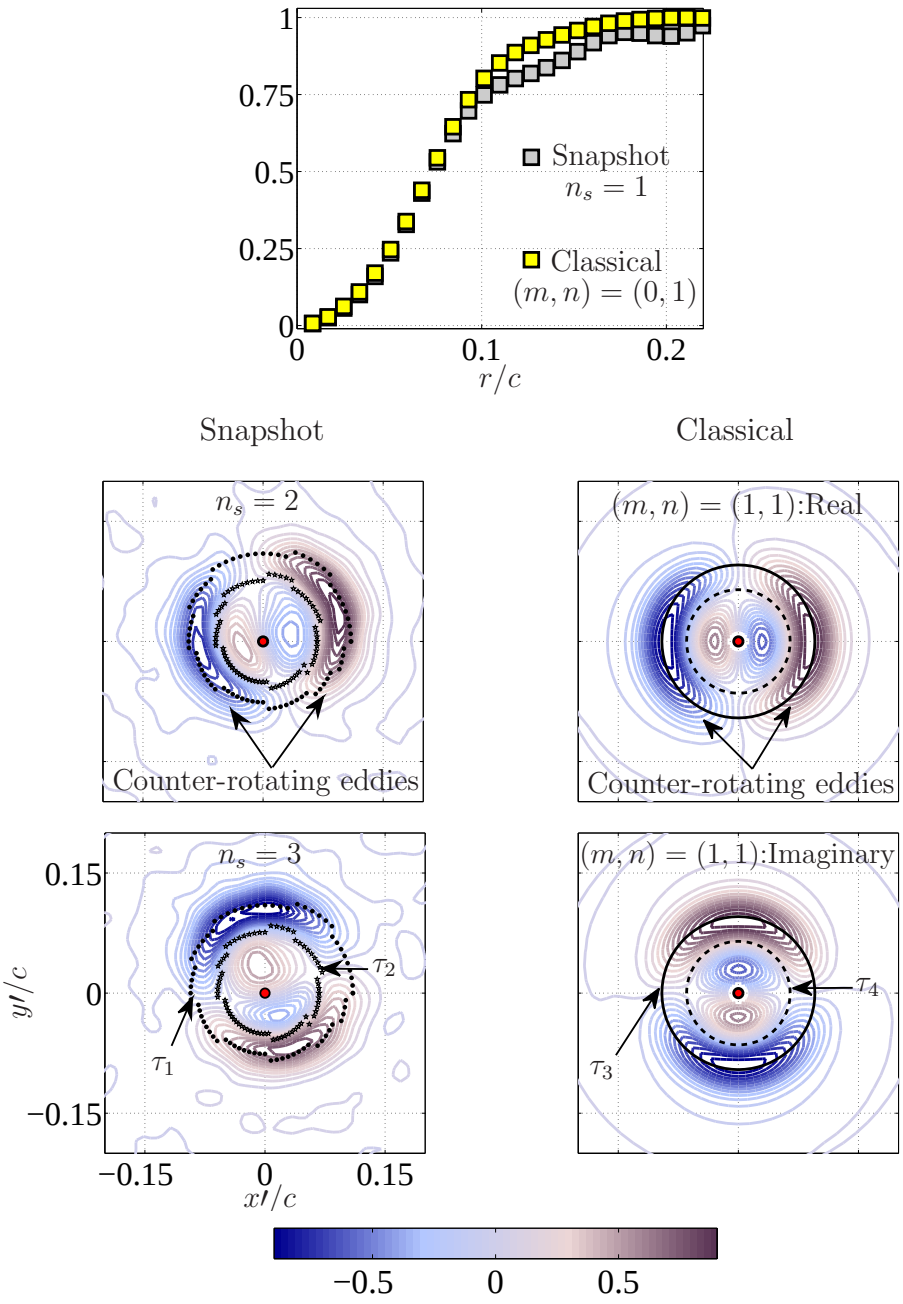

Figure 5.2: Mode shapes of the snapshot POD alongside their counterparts of the classical POD at $\psi = 45°$: (top) radial profile of circulation; (top & bottom) axial vorticity contours. τ_1: mean core-boundary, τ_2: locations of peak TKE, τ_3: mean core-radius, τ_4: mean location of peak TKE.

of the axisymmetric mode $(m, n) = (0, 1)$ (classical POD) as illustrated in figure 5.2. Therefore, the $n_s = 1$ here is associated with the roll-up of the vorticity-sheet trailed from the rotor blade at early ages. Whereas the higher modes $n_s = 2$ and $n_s = 3$, at $\psi = 45°$ in figure 5.2, form the counterparts of the real and imaginary components, respectively, of the helical mode $(m, n) = (1, 1)$ (classical POD), which was shown earlier to be the most unstable mode associated with the elliptic instability in the current set of measurements. As for the counter-rotating eddies (figure 5.2) of this most unstable mode of the elliptic instability, they reside on the mean core-radius in the classical technique, whereas they reside on the mean core-boundary in the snapshot POD.

In contrast to the order of dominant motions observed at $\psi = 45°$, figure 5.3 shows that at $\psi = 315°$ the first two modes ($n_s = 1$ and $n_s = 2$) of the snapshot technique resemble the real and imaginary components of the helical mode $(m, n) = (1, 1)$ (classical POD); the $n_s = 3$ mode closely resembles that of the axisymmetric mode $(m, n) = (0, 1)$ (classical POD), which behaves as a swirling jet (see Liang & Maxworthy (2005) [52]) at higher ages. Similar order of dominance was observed at all other vortex ages (except at 45°) in the measurement envelope.

Having seen that the helical mode $(m, n) = (1, 1)$ (classical POD) has a counterpart in the snapshot POD, their evolutionary behavior is compared here over the range of vortex ages measured. For the sake of comparison, the evolutionary characteristics of this helical mode $(m, n) = (1, 1)$ (classical

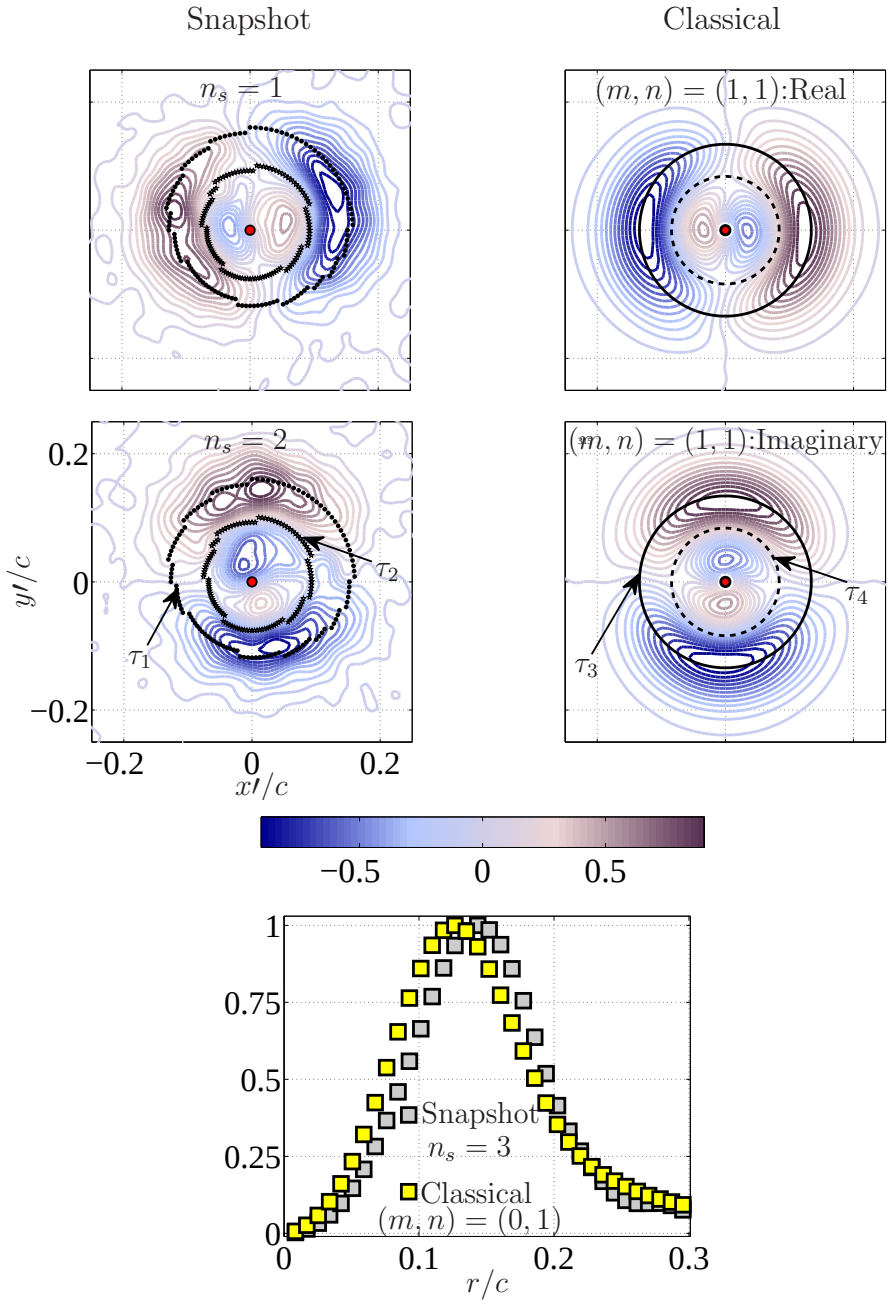

Figure 5.3: Mode shapes of the snapshot POD alongside their counterparts of the classical POD at $\psi = 315°$: (top & middle) axial vorticity contours; (bottom) radial profile of circulation. τ_1: mean core-boundary, τ_2: locations of peak TKE, τ_3: mean core-radius, τ_4: mean location of peak TKE.

POD), which was shown earlier in figure 4.9, is duplicated in figure 5.4 alongside that of its counterpart in the snapshot technique. Once again, the two counter-rotating eddies in the helical mode $(m, n) = (1, 1)$ (classical POD) which reside on the circle of mean core-radius at $\psi = 45°$ (figure 5.4b) continue to remain centered on the mean core-radius for all the vortex ages without modifying the structure of the helical mode; therefore, this helical mode of the elliptic instability exhibits a linear behaviour. Similarly in the case of snapshot technique, the two counter-rotating eddies of the mode in figure 5.4a remain centered on the mean core-boundary for all the vortex ages in the measurement envelope, without significantly modifying the structure of this mode. Therefore, this mode of the elliptic instability as seen by the snapshot technique (figure 5.4*a*) is also in the linear regime.

Since both the snapshot and classical techniques of POD have demonstrated similar dominant motions, at this point it is worth addressing if the resolved turbulence kinetic energies (from Eq. 3.13 and Eq. 3.20, respectively) contained in these dominant motions are also consistent between these two techniques. For this, figure 5.5a, b illustrates the resolved energy residing in the axisymmetric $(m, n) = (0, 1)$ and helical $(m, n) = (1, 1)$ modes (classical POD), respectively, along with their counterparts of the snapshot POD for the range of vortex ages studied. It is evident that the resolved energy contributions from these large-scale motions are also consistent between these two forms of POD.

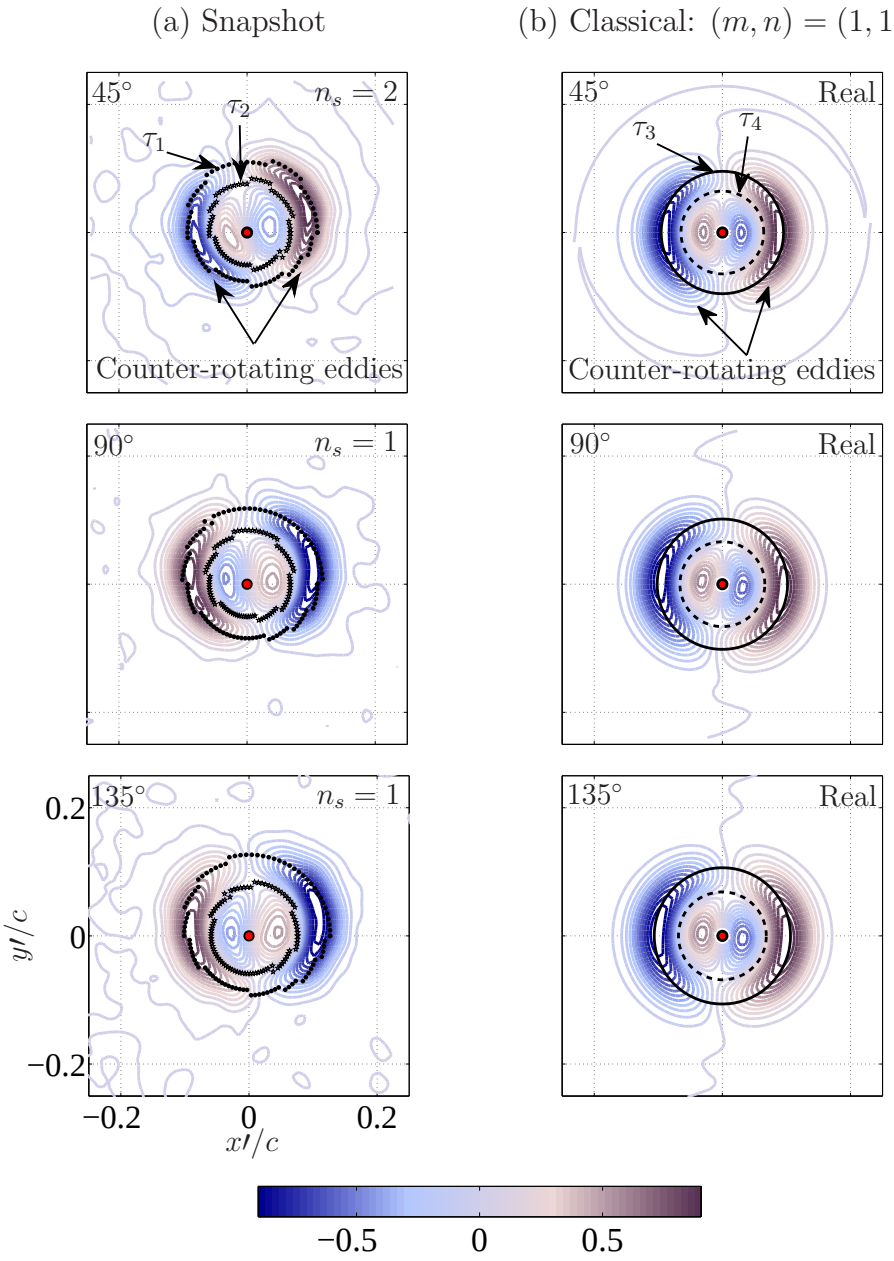

Figure 5.4: Continued on next page and caption provided at the end of the figure.

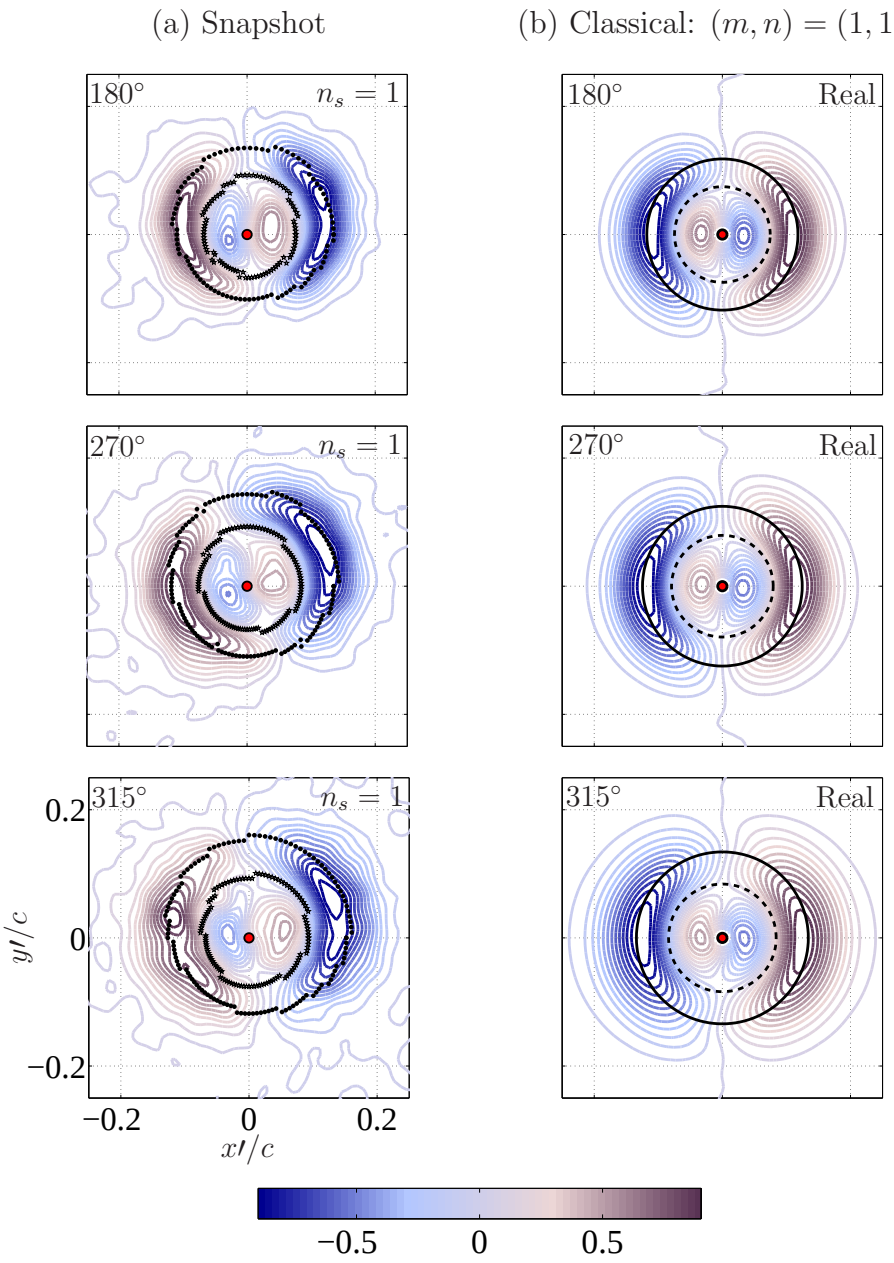

Figure 5.4: Continued on next page and caption provided at the end of the figure.

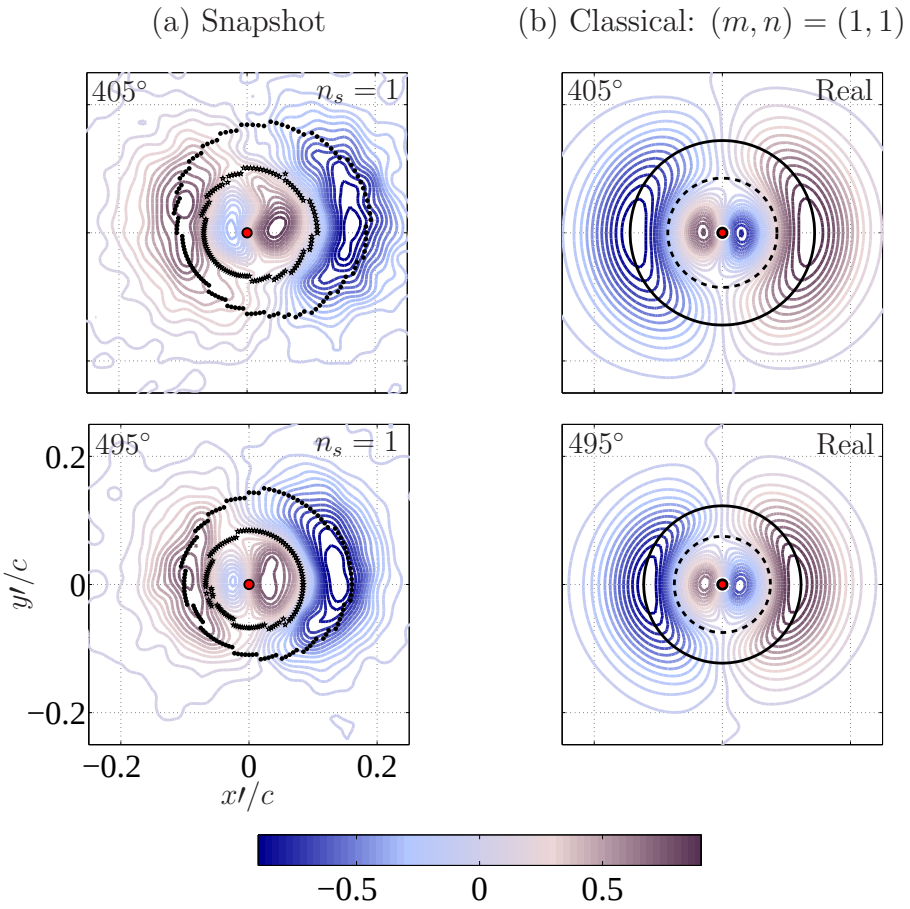

Figure 5.4: Axial vorticity of the most unstable mode of elliptic instability, from (a) snapshot POD and (b) classical POD: (real component) helical mode $(m, n) = (1, 1)$, at $\psi = 45° - 495°$. τ_1: mean core-boundary, τ_2: locations of peak TKE, τ_3: mean core-radius, τ_4: mean location of peak TKE.

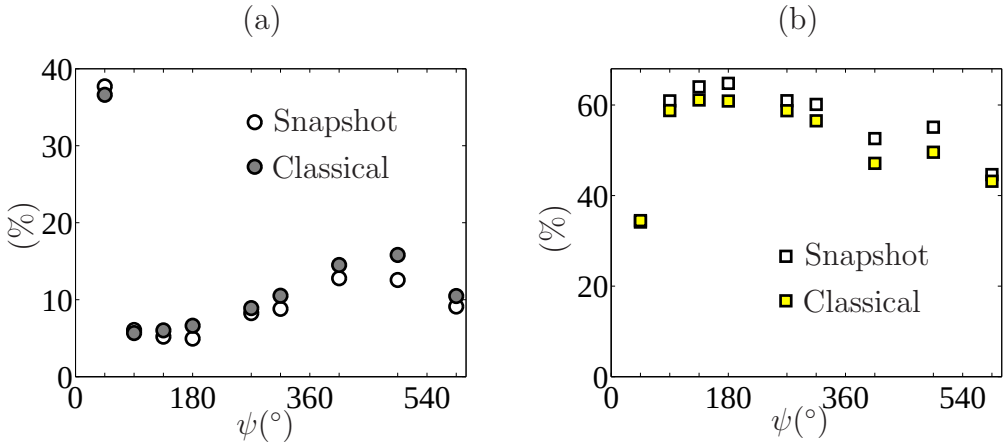

Figure 5.5: Resolved energy comparisons between (a) the axisymmetric mode $(m, n) = (0, 1)$ (classical POD) and its counterpart of the snapshot POD, (b) the helical mode $(m, n) = (1, 1)$ (classical POD) and its counterpart of the snapshot POD.

5.1.1 Asymmetries in the vortex filament

Concerning the asymmetries in the turbulence kinetic energy per unit mass (TKE) in the plane perpendicular to the vortex axis, once again, figure 5.6a, b (duplication of the findings in figure 3.9) shows that the TKE is asymmetric inside the vortex core at sample $\psi = 180°$ and 315°, respectively. Therefore, it is worth comparing how these asymmetries in TKE are introduced in the tip vortex between the snapshot and classical forms of POD. To do so, a low-dimensional reconstruction of the turbulence kinetic energy per unit mass ($\mathfrak{E} = 0.5\langle \mathfrak{u}_1^2 + \mathfrak{u}_2^2 \rangle$ with $\mathfrak{u}_{i=1,2}$ being the in-plane low-dimensional fluctuating velocity obtained from Eq. 3.14 and Eq. 3.23) using the above large-scale motions is shown in figures 5.7, 5.9 and 5.11 (a, b) from the snapshot and classical techniques, respectively. To start with, figure 5.7 shows $\mathfrak{E}$

constructed using the helical mode $(m, n) = (1, 1)$ (classical POD) alongside that of its counterpart ($n_s = 1$ to 2) in the snapshot technique at $\psi = 180°$ and 315°. It is evident that this counterpart ($n_s = 1$ and 2) of the snapshot technique introduces more asymmetry in $\mathfrak{E}$ than that of the helical mode from the classical POD. This variation in asymmetry established here by these two techniques is also demonstrated on slices of $\mathfrak{E}$ (indicated by ϵ in figure 5.7) in figure 5.8a, b at $\psi = 180°$ and 315°, respectively.

As an extension, $\mathfrak{E}$ is constructed using the combination of axisymmetric and helical modes ($m = 0$ to 1; $n = 1$) in the classical POD alongside that of their counterpart ($n_s = 1$ to 3) in the snapshot technique at $\psi = 180°$ and 315° as shown in figure 5.9. Once again, the asymmetry in $\mathfrak{E}$ introduced by the combination of modes ($m = 0$ to 1; $n = 1$) of the classical POD does not appear to match that of their counterpart in the snapshot technique. Such a nonconformity can also be seen on slices of $\mathfrak{E}$ (indicated by ϵ in figure 5.9) illustrated in figure 5.10a, b at $\psi = 180°$ and 315°, respectively. Nevertheless, as it was also demonstrated earlier in § 4.2.1.1, the combination of axisymmetric and helical modes of the classical technique produced more asymmetries in $\mathfrak{E}$ (figures 5.9 and 5.10) compared to that of the helical mode alone (figures 5.7 and 5.8). Further, if another mode is introduced (double helical mode) along with the axisymmetric and helical modes (classical POD) in the construction of $\mathfrak{E}$, this new combination ($m = 0$ to 2; $n = 1$) was shown earlier to introduce more asymmetry in $\mathfrak{E}$ than that of the combination of helical and axisymmetric modes ($m = 0$ to 1; $n = 1$). Following this, if $\mathfrak{E}$ that is constructed

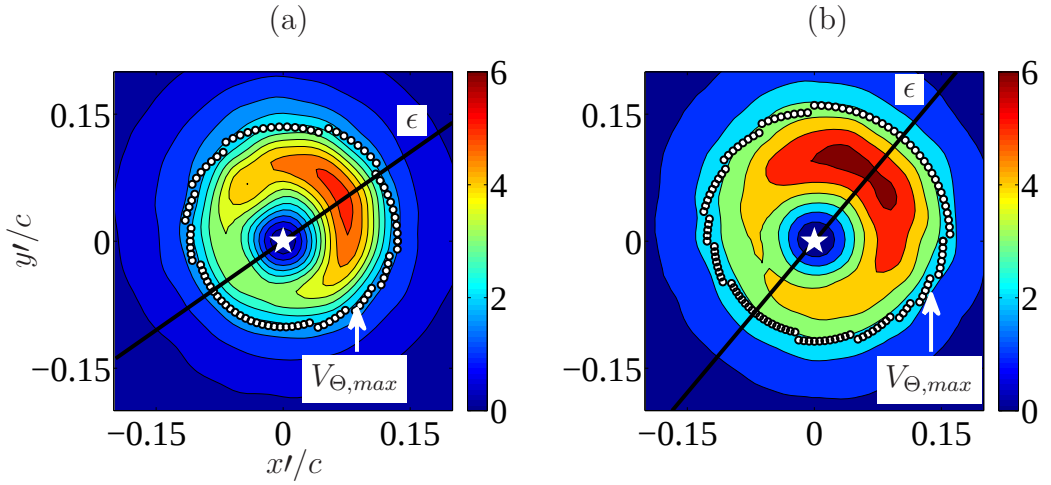

Figure 5.6: Turbulence kinetic energy per unit mass, $(\mathrm{TKE}/V_{tip}^2) \times 10^3$, at (a) $\psi = 180°$ and (b) $\psi = 315°$. Mean vortex core boundary identified by the locations of peak swirl velocity ($V_{\Theta,max}$) also identified.

using $n_s = 1$ to 3 (snapshot technique) in figure 5.9 is duplicated in figure 5.11 and compared to that of the new combination of modes of the classical POD: axisymmetric, helical and double helical modes ($m = 0$ to 2; $n = 1$), the asymmetries in $\mathfrak{E}$ appear to nearly match. Such an equivalence in asymmetries is also demonstrated on the slices of $\mathfrak{E}$ (indicated by ϵ in figure 5.11) in figure 5.10a, b at $\psi = 180°$ and 315°, respectively. Therefore, as for the asymmetries in turbulence kinetic energy (per unit mass), the classical POD requires more modes when compared to that of the snapshot POD; hence, once again the snapshot technique is more efficient than the classical POD. Nevertheless, the classical form was preferred in the current study (see § 4) owing to the easier interpretation of the Fourier-azimuthal modes.

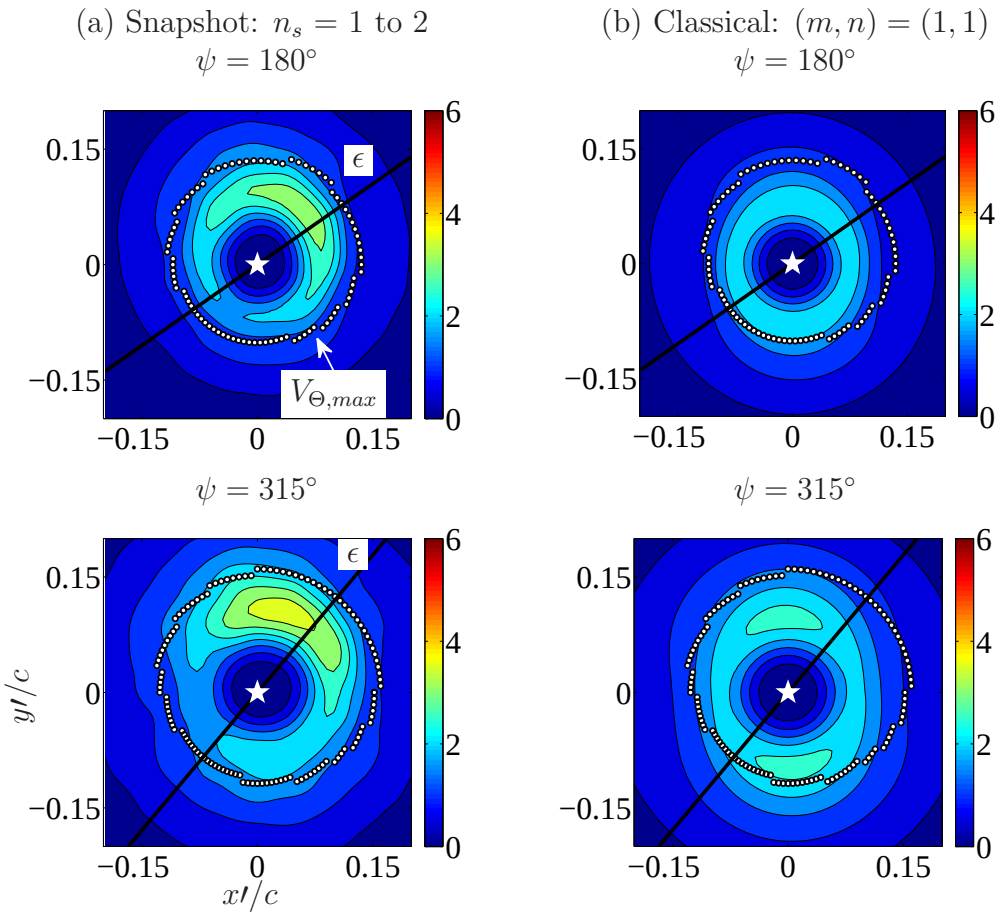

Figure 5.7: Low-dimensional turbulence kinetic energy per unit mass, $\mathfrak{E}/V_{tip}^2 \times 10^3$, at $\psi = 180°$ and 315°. Slice ϵ at each vortex age corresponds to the slice drawn in figure 5.6 for the respective vortex age. Mean vortex core boundary identified by the locations of peak swirl velocity ($V_{\Theta,max}$) also identified.

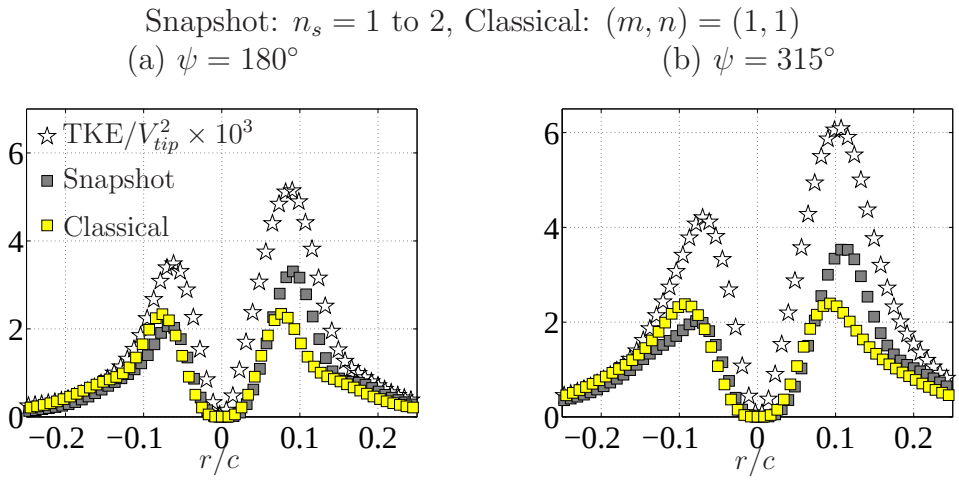

Figure 5.8: Low-dimensional turbulence kinetic energy per unit mass, $\mathfrak{E}/V_{tip}^2 \times 10^3$, on a vortex slice ϵ in figure 5.7 at $\psi = 180°$ and 315°. Actual TKE on the vortex slice also indicated.

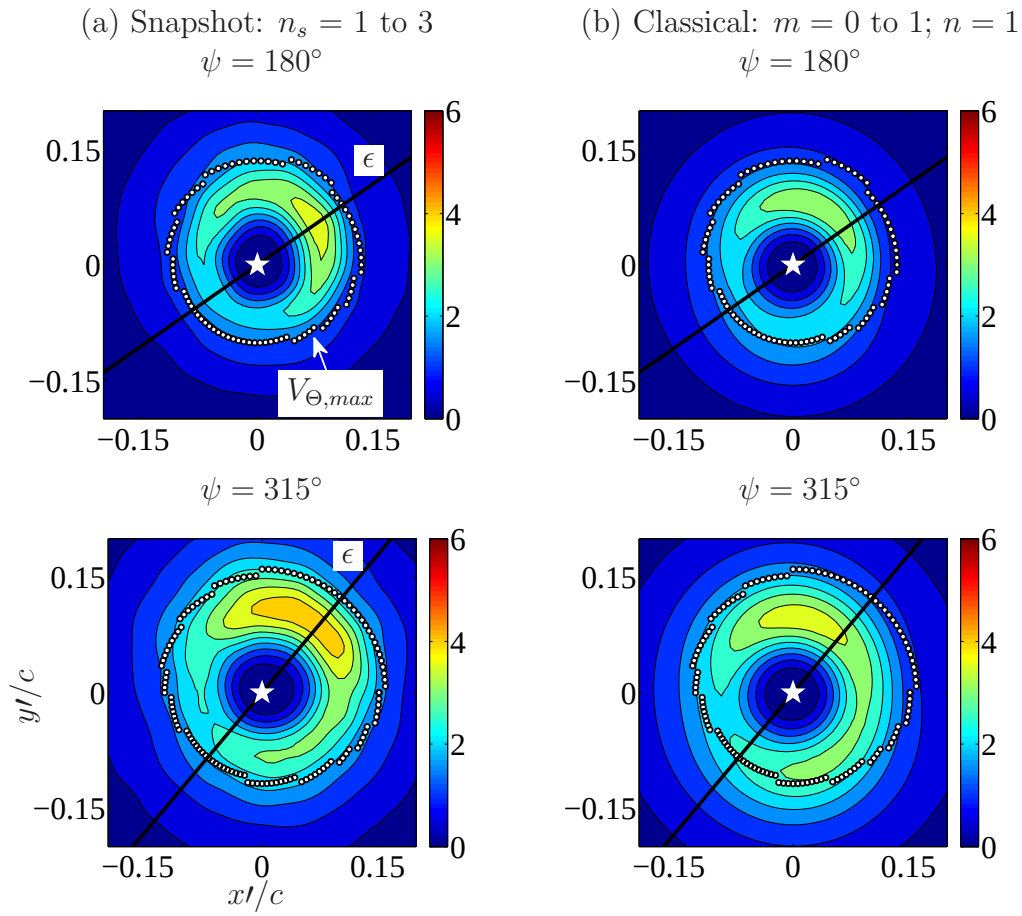

Figure 5.9: Low-dimensional turbulence kinetic energy per unit mass, $\mathfrak{E}/V_{tip}^2 \times 10^3$, at $\psi = 180°$ and 315°. Slice ϵ at each vortex age corresponds to the slice drawn in figure 5.6 for the respective vortex age. Mean vortex core boundary identified by the locations of peak swirl velocity ($V_{\Theta,max}$) also identified.

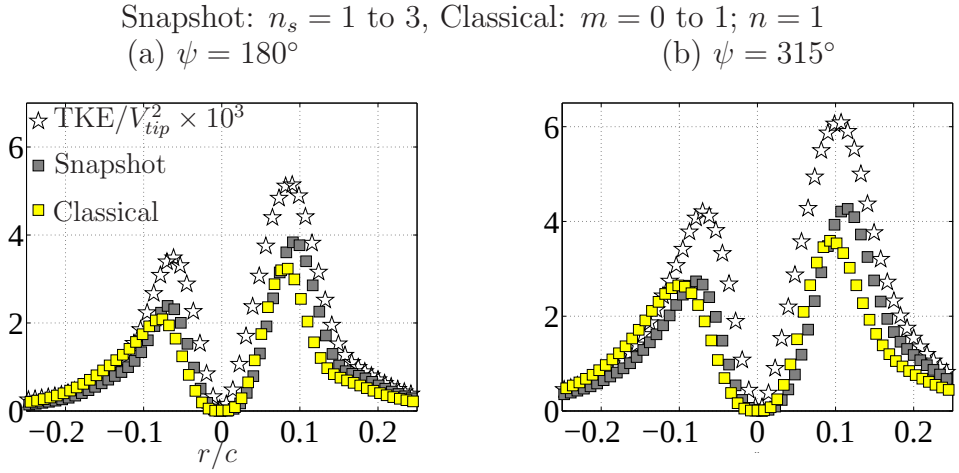

Figure 5.10: Low-dimensional turbulence kinetic energy per unit mass, $\mathfrak{E}/V_{tip}^2 \times 10^3$, on a vortex slice ϵ in figure 5.7 at $\psi = 180°$ and 315°. Actual TKE on the vortex slice also indicated.

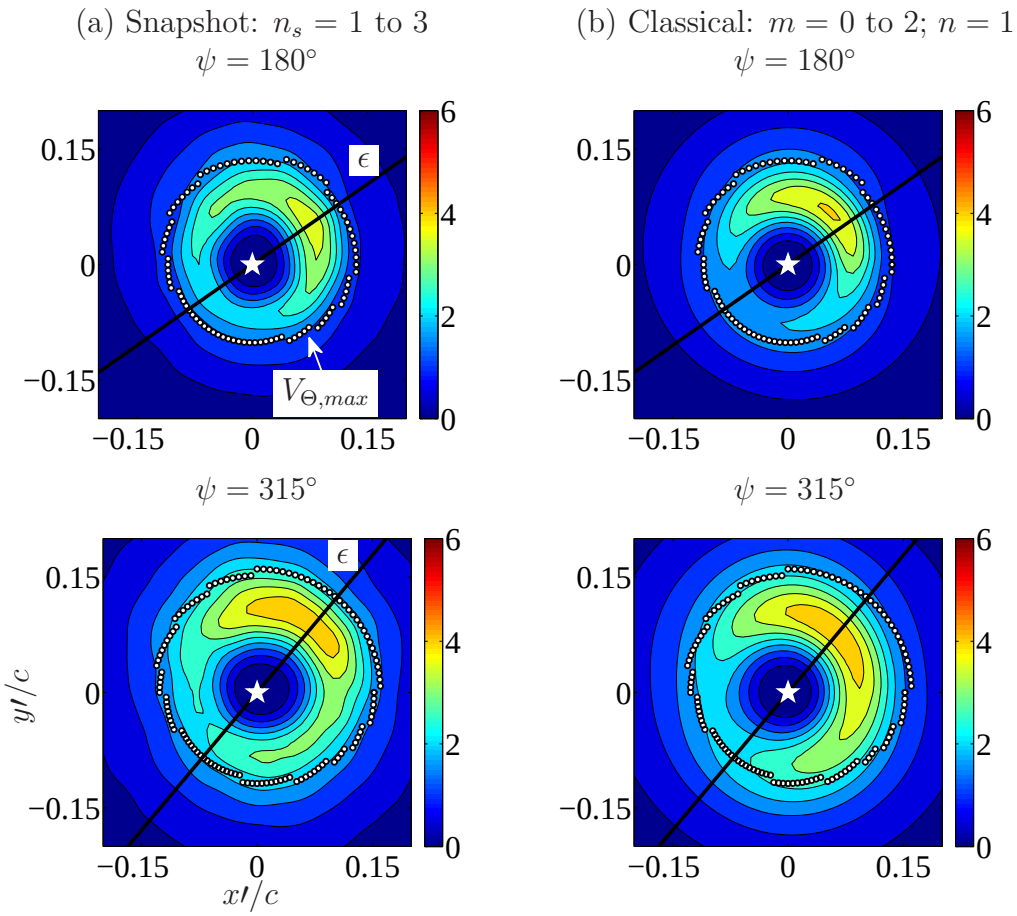

Figure 5.11: Low-dimensional turbulence kinetic energy per unit mass, $\mathfrak{E}/V_{tip}^2 \times 10^3$, at $\psi = 180°$ and 315°. Slice ϵ at each vortex age corresponds to the slice drawn in figure 5.6 for the respective vortex age. Mean vortex core boundary identified by the locations of peak swirl velocity ($V_{\Theta,max}$) also identified.

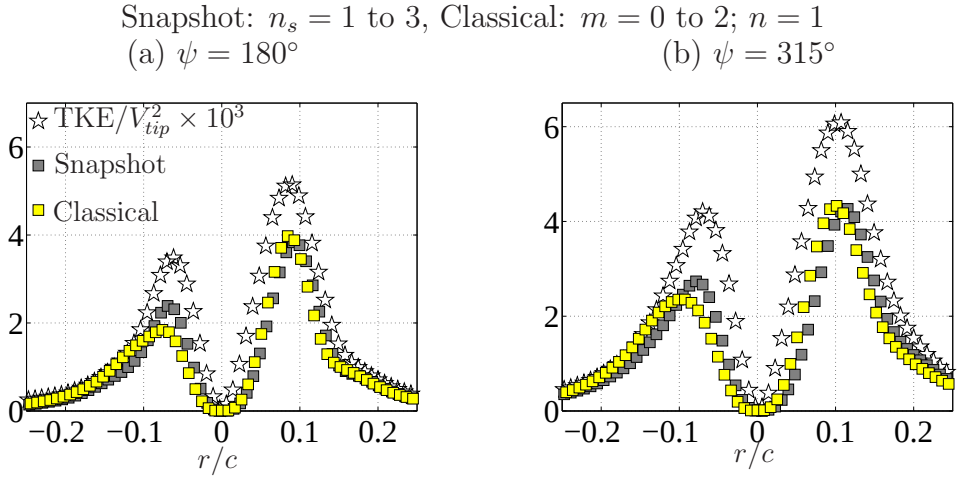

Figure 5.12: Low-dimensional turbulence kinetic energy per unit mass, $\mathfrak{E}/V_{tip}^2 \times 10^3$, on a vortex slice ϵ in figure 5.7 at $\psi = 180°$ and 315°. Actual TKE on the vortex slice also indicated.

Chapter 6

Sensitivity of POD to the choice of the vortex centering technique

In the previous chapters, using the Γ_1 centering technique (described in § 3 for wander correction) low-dimensional characterization of the velocity fluctuations (within the tip vortex) was performed by way of the proper orthogonal decomposition (see § 3, § 4 and § 5). At this point, an interesting question that is worth addressing is to what affect does the choice of the vortex centering technique have on the low-dimensional features obtained by POD. The Γ_1 method was preferred earlier since it is a non-divergence based technique and is very efficient in identifying the location of zero swirl (defined as the vortex center [56, 57]) within the vortex core. For the current set of measurements this method produced zero in-plane turbulence at the vortex center (see figures 3.9 and 3.10) which is an inherent characteristic of a vortex flow (as $\tilde{u}_{i=1,2} = u_i = 0$ at the vortex center). But the concern is whether aligning

This chapter may compose material from the author's previously published articles,

S. M. Mula and C. E. Tinney. A study of the turbulence within a spiralling vortex filament using proper orthogonal decomposition. *J. Fluid Mech.*, 769: 570–589, 2015. For this project, Tinney served as the project advisor.

S. M. Mula and C. E. Tinney. Classical and Snapshot forms of the POD technique applied to a helical vortex filament. *AIAA Paper* 2014-3257, 2014. For this project, Tinney served as the project advisor.

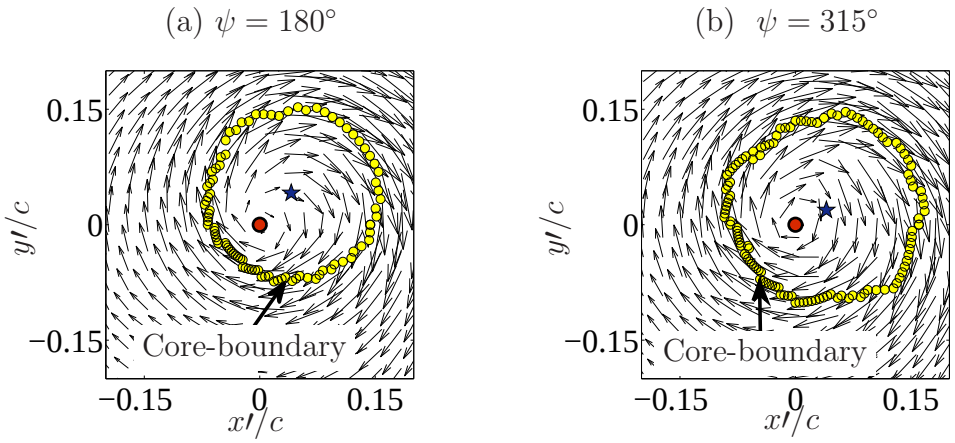

Figure 6.1: Sample instantaneous vector maps with centers identified by the Γ_1 ($\circ$) and GC ($\star$) methods at (a) $\psi = 45°$ and (b) $\psi = 315°$. Instantaneous vortex core boundaries are also identified.

the inner core region with the Γ_1 approach causes regions outside the core to be smeared. Therefore, a second approach is examined which aims to align the regions outside the core by biasing the vortex centering technique with features associated with the outer portions of the vortex core. This is accomplished by aligning each vortex by way of its geometric center (hereafter referred to as GC), which is the area center (or centroid) of its vortex core. Sample illustrations of the geometric centers of the instantaneous vortex cores are shown in figure 6.1a, b at sample $\psi = 180°$ and 315°, respectively. Alongside the geometric centers the corresponding vortex centers (identified by Γ_1) are also indicated to demonstrate the differences between their locations. Subsequent effects of these two centering techniques on the low-dimensional features (by way of POD) are illustrated and compared in this chapter. However, prior to comparing the low-dimensional features, the effect of the GC technique on the

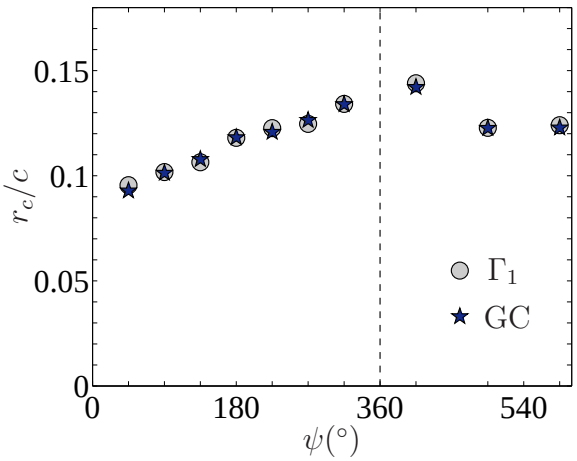

Figure 6.2: Mean core-radius trends in the current study using the two vortex centering techniques: Γ_1 and GC methods.

mean characteristics and velocity fluctuations of the tip vortex are discussed and compared with the findings obtained earlier (§ 3.2.3) using the Γ_1 method.

6.1 Mean statistics

Following the correction for wander using the GC method, mean core-radius is estimated at each ψ in the measurement envelope and the resulting trends are demonstrated in figure 6.2 alongside the findings (duplication of the results in figure 3.7) using the Γ_1 method. It is evident that the mean core-radius (at any ψ) is nearly uneffected to the choice of the centering technique.

Details of the mean axial vorticity of the tip vortex are demonstrated in figure 6.3a, b using the Γ_1 and GC techniques, respectively, at sample $\psi = 180°$ and $\psi = 315°$. Also, sample slices (horizontal) of the corresponding mean axial vorticity at $\psi = 180°$ and $\psi = 315°$ are shown in figure 6.4a, b, respectively.

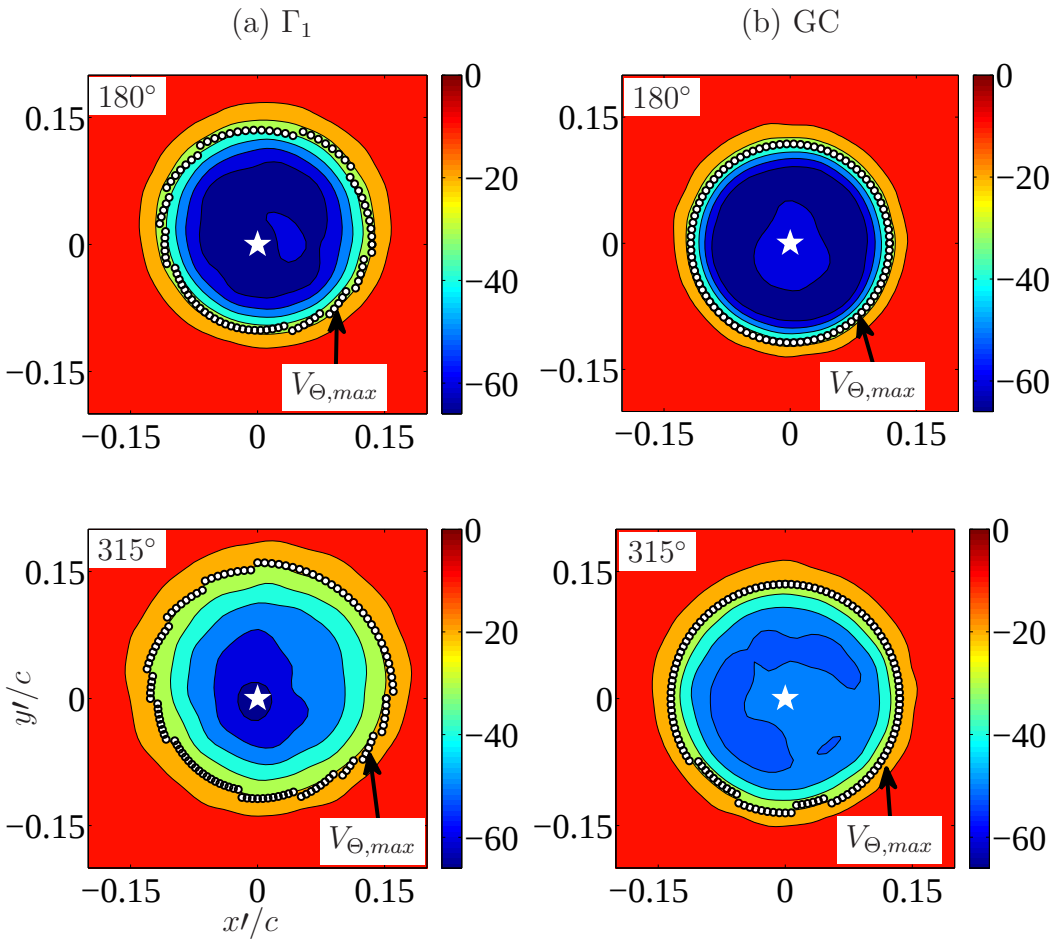

Figure 6.3: Mean axial vorticity (ω_z/Ω) using (a) Γ_1 approach and (b) GC method at $\psi = 180°$ and 315°. Locations of peak swirl velocity ($V_{\Theta,max}$), which define the mean core-boundary, also identified.

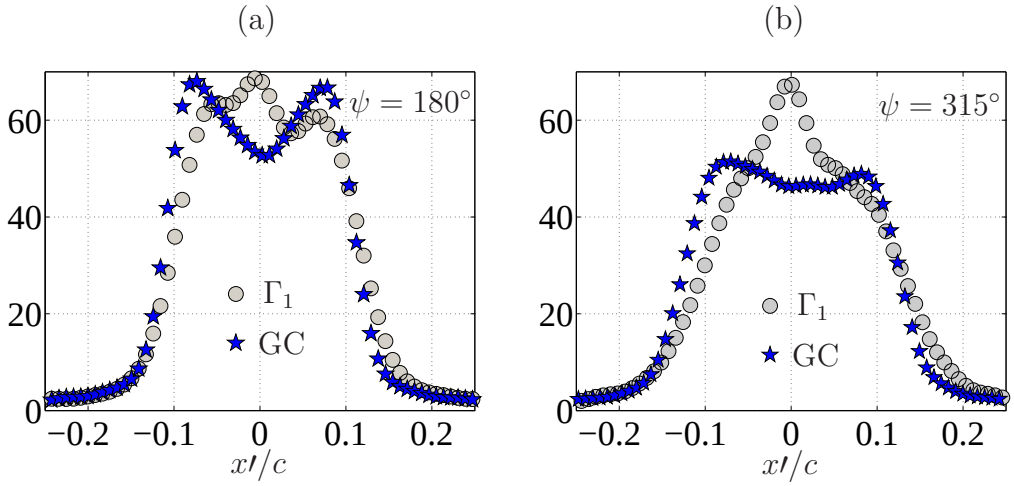

Figure 6.4: Mean axial vorticity $(-\omega_z/\Omega)$ at (a) $\psi = 180°$ and (b) $\psi = 315°$ on a vortex slice through the vortex center.

While differences between the two centering techniques are manifest in the inner vortex core region (close to the vortex axis in figures 6.3 and 6.4), the outer portions of the core appear to remain nearly unaffected.

Having seen that the GC technique has an effect on the axial vorticity in the inner core region of the vortex, figure 6.5 shows how it effects the turbulence kinetic energy per unit mass (TKE) at sample $\psi = 180°$ and 315°. While the Γ_1 method produces an asymmetric TKE (in azimuth) inside the vortex, the GC method appears to introduce more symmetry with less turbulence fluctuations except near the vortex axis. See sample slices (indicated by ϵ in figure 6.5) of TKE (along with mean swirl velocities) in figure 6.6, which further demonstrates how the GC method introduces artificially elevated turbulence levels at the vortex center. Whereas the Γ_1 method, once again, preserves the inherent characteristic of zero in-plane turbulence at the vortex axis.

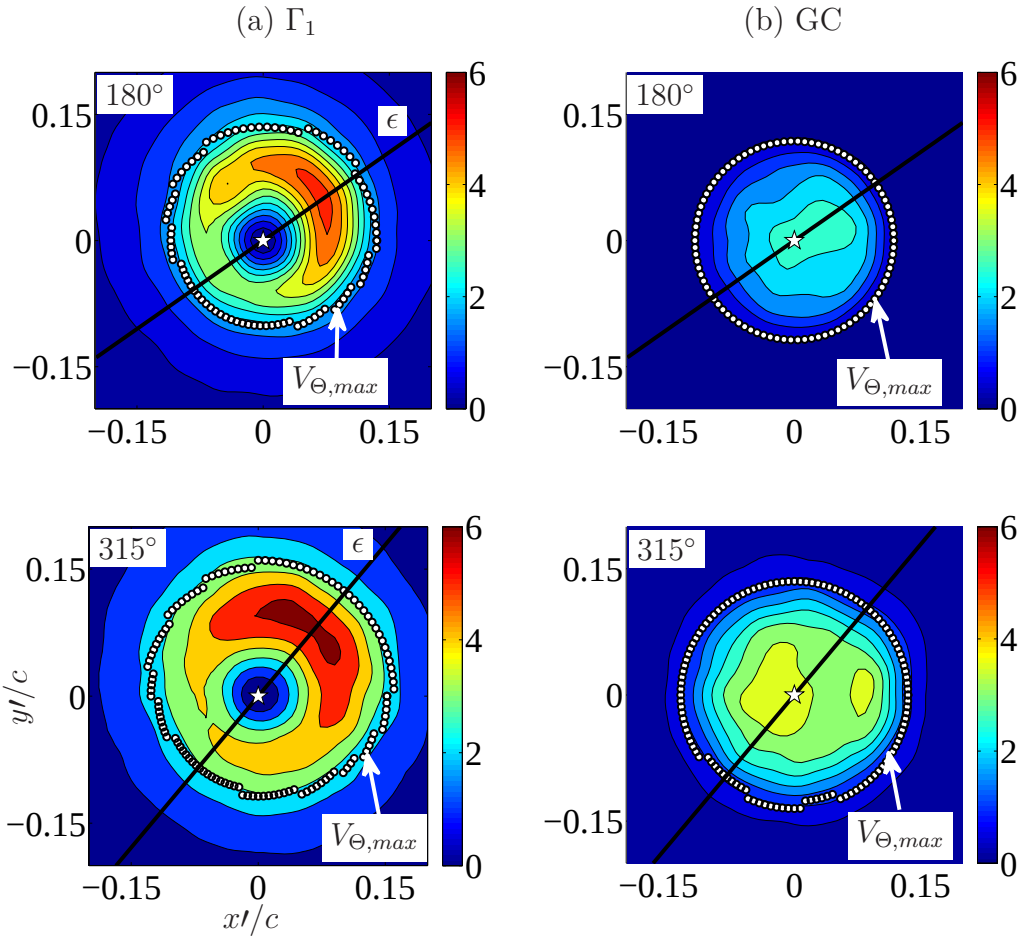

Figure 6.5: Turbulence kinetic energy per unit mass, $(\text{TKE}/V_{tip}^2)\times 10^3$, using (a) the Γ_1 approach and (b) the GC technique at $\psi = 180°$ and 315°. Mean vortex core boundary identified by the locations of peak swirl velocity ($V_{\Theta,max}$) also identified.

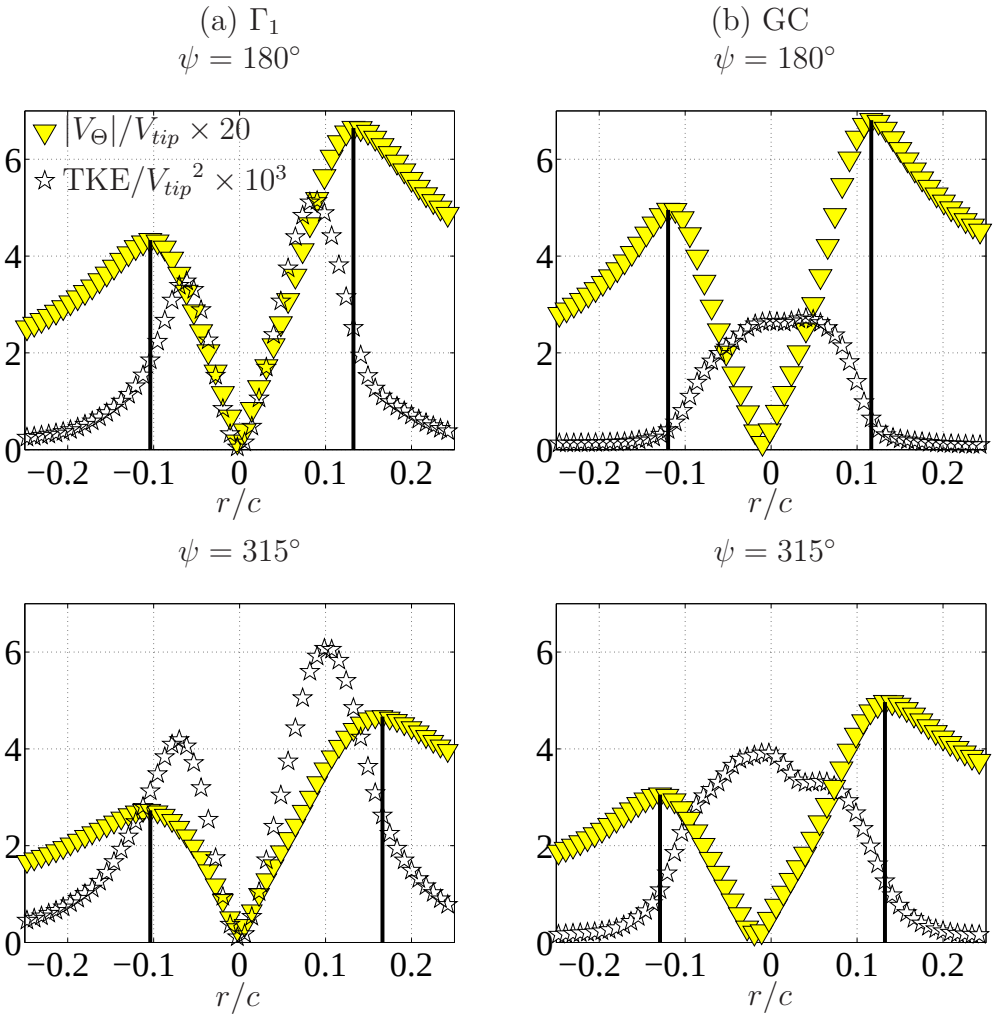

Figure 6.6: Swirl velocity, $(|V_\Theta|/V_{tip}) \times 20$ ($\bigtriangledown$), and $(\mathrm{TKE}/V_{tip}^2) \times 10^3$ ($\star$) at (a) $\psi = 180°$ and (b) $\psi = 315°$ on a vortex slice. Vortex core boundary identified by peak swirl velocity also indicated.

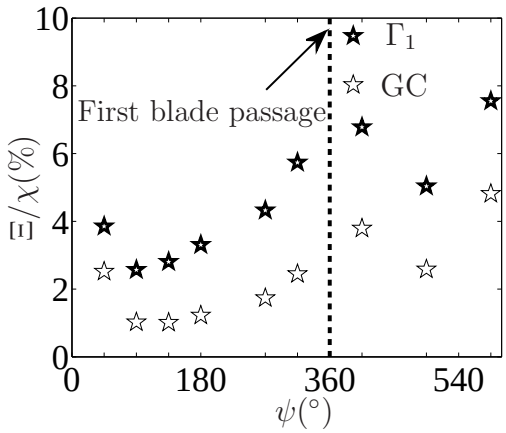

Figure 6.7: Total resolved turbulence kinetic energy (Ξ) normalized with the total resolved kinetic energy (χ) of the flow.

As for the total resolved turbulence kinetic energy (Ξ), comparisons between the Γ_1 and GC techniques are provided in figure 6.7. Though the trends in Ξ (discussed earlier in § 4.2.1.1) are similar between these two techniques, the GC method produces lower turbulence energies at all the vortex ages in the measurement envelope.

6.2 Low-dimensional characteristics

Having shown the effect of the GC technique on the statistical properties of the vortex, its effect on the low dimensional features is examined here. For this, the classical form of POD is employed owing to the easier interpretation of the Fourier modes. Figure 6.8a illustrates the POD energy spectrum for sample vortex ages in the measurement envelope. As demonstrated earlier using the Γ_1 method (in § 4.2), 75% of the resolved turbulence kinetic energy resides in the first ($n = 1$) POD mode (for the entire range of ψ studied). Once

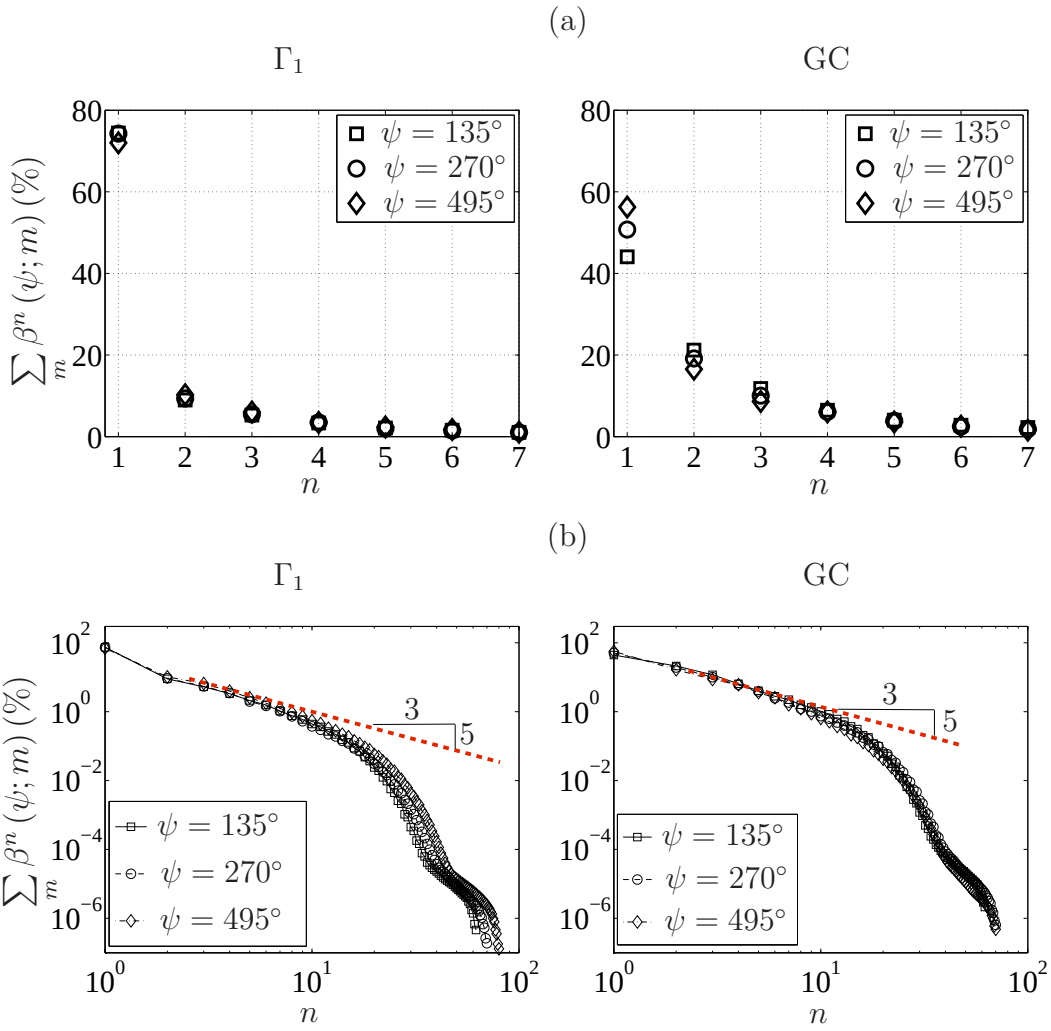

Figure 6.8: (a) Energy spectra of the first seven POD modes. (b) Energy spectra of the POD modes on a logarithmic scale.

again, such a rapid convergence reflects the presence of highly organized motions inside the tip vortex. However, using the GC method a different quantum (of the resolved energy) resides in the first POD mode. Nevertheless, it still manifests a rapid convergence within the first few POD modes. Furthermore, figure 6.8b demonstrates the POD energy spectrum on a logarithmic scale; irrespective of the centering technique used, the energy spectrum exhibits a $k^{-5/3}$ inertial range [62] in the first decade of POD modes.

6.2.1 Fourier-azimuthal modes for the first $n = 1$ POD mode

As for the Fourier energy spectrum associated with the first ($n = 1$) POD mode, figure 6.9 shows how the GC technique produces exactly the opposite behavior than the Γ_1 method where the axisymmetric ($m = 0$) and helical ($m = 1$) modes are concerned. As demonstrated earlier using the Γ_1 method (in § 4.2), the helical mode ($m = 1$) dominates the energy spectrum at all ψ (except at 45°), followed by the axisymmetric ($m = 0$) and double helical ($m = 2$) modes. However, at $\psi = 45°$ the helical and axisymmetric modes are equally dominant. Whereas using the GC method, at $\psi = 45°$ only the axisymmetric mode is dominant, while at other ψ equal levels of contributions from the axisymmetric and helical modes are manifest in the measurement envelope. Furthermore, figure 6.10 illustrates the Fourier spectra on a logarithmic scale where (apart from the first few azimuthal modes) both the Γ_1 and GC methods demonstrate similar overall rates of convergence.

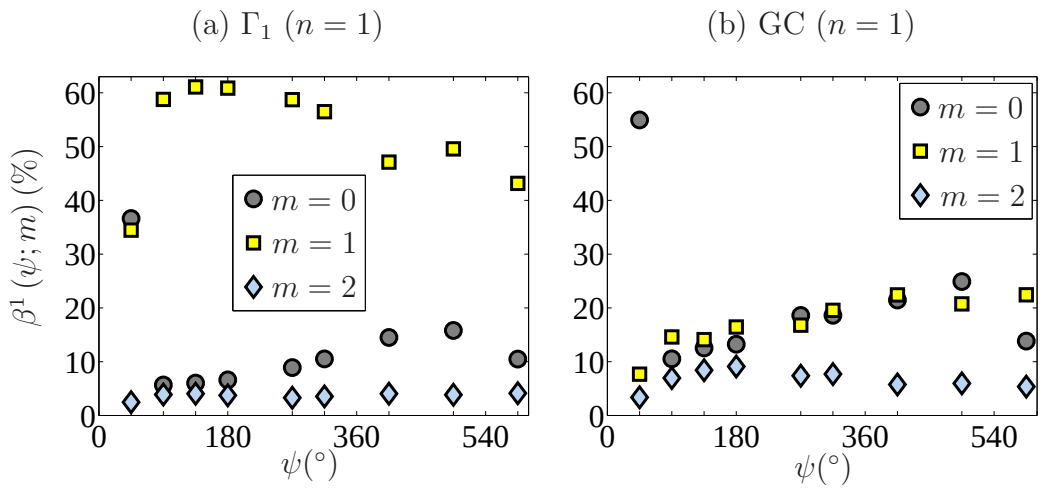

Figure 6.9: Fourier mode energy spectra associated with the first $(n = 1)$ POD mode.

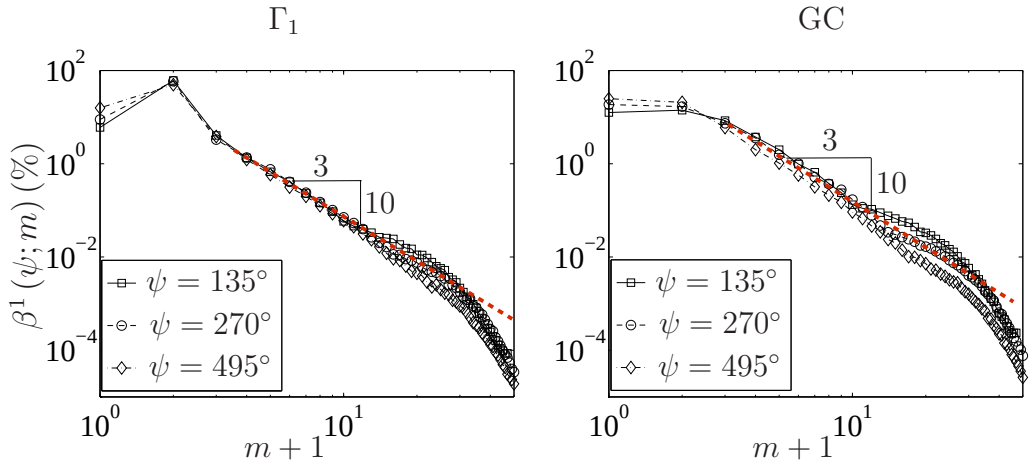

Figure 6.10: Fourier energy spectra associated with the first POD mode on a logarithmic scale.

Where the spatial distribution of the resolved energy is concerned, figure 6.11 shows how the radial profile of energy (per unit mass) is for the Fourier modes displayed in figure 6.9. These profiles, which are in normalized form, are originally determined from the following standard expression

$$\mathfrak{B}_{ii}^{(1)}(r,\psi;m) = \Lambda^{1}(\psi;m)\,\Phi_{i}^{(1)}(r,\psi;m)\Phi_{i}^{(1)*}(r,\psi;m), \tag{6.1}$$

with subscripts written in the Einstein notation. At $\psi = 45°$ it is interesting to see how the Γ_1 and GC techniques produce matching profiles (figure 6.11a) for the axisymmetric mode ($m = 0$). However, at later ages (figure 6.11b) the GC technique shifts the peak energy radially inward (toward vortex center) from that of the Γ_1 method. Furthermore, the GC technique demonstrates to significantly effect the helical ($m = 0$) and double helical ($m = 1$) modes at both early and later vortex ages. It is also interesting to point out how the helical mode here, in the GC technique, produces non-zero in-plane turbulence energy at the vortex center ($r = 0$), which is more prominent at later vortex ages (see figure 6.11b). This suggests that the elevated velocity fluctuations at the vortex center in figure 6.6b are caused predominantly by the helical mode.

Spatial structures of the above dominant motions are presented in figures 6.12, 6.13 and 6.14. To begin with the axisymmetric mode, its radial profiles of circulation are displayed in figure 6.12a, b for $\psi = 45°$ and 315°, respectively. Using the Γ_1 method, at $\psi = 45°$ the profile was shown earlier (in figure 4.4) to resemble that of a vortex with viscous core; while at later ages, the axisymmetric mode was shown to behave as a swirling jet. It is interesting to note that the GC technique produces similar characteristics of the

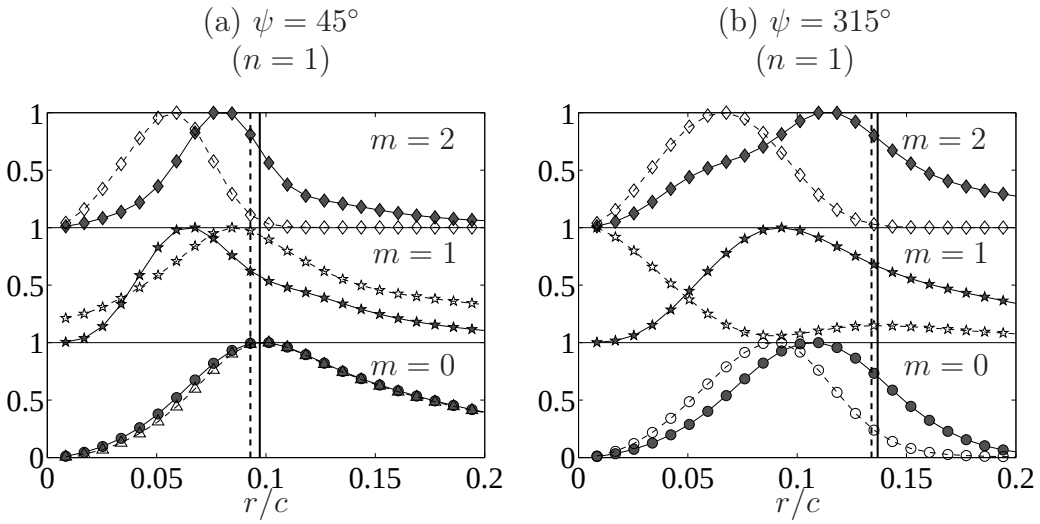

Figure 6.11: Radial profile (in normalized form) of the resolved energy (per unit mass) of the first three ($m = 0$ to 2) Fourier-azimuthal modes associated with the first ($n = 1$) POD mode at (a) $\psi = 45°$ and (b) $\psi = 315°$ using the Γ_1 (filled symbols) and GC (open symbols) methods. Mean core radius using the Γ_1 (solid line) and GC (dashed line) methods also identified.

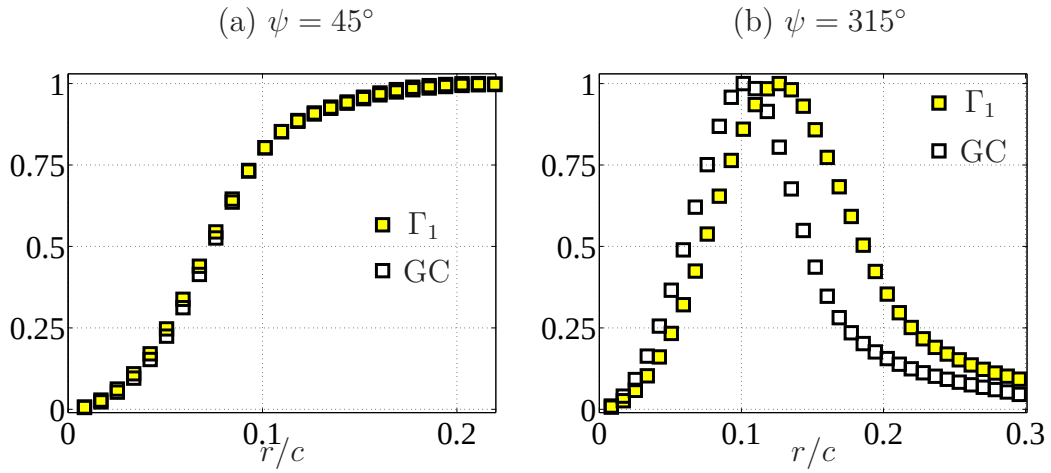

Figure 6.12: Radial profiles of circulation (□) for $(m, n) = (0, 1)$ at (a) $\psi = 45°$ and (b) $\psi = 315°$.

axisymmetric mode in figure 6.12a, b. However, the GC technique manifests to shift the peak circulation of the swirling jet mode (figure 6.12b) radially inward (towards vortex axis) from that of the Γ_1 method at later ages.

As for the spatial structure of the helical mode ($m = 1$), axial vorticity contours (real component) are displayed in figure 6.13 at $\psi = 45° - 495°$. Using the Γ_1 method, the helical mode in figure 6.13a was demonstrated earlier (see figures 4.6 and 4.6) to be associated with the elliptic instability. Once again, the counter-rotating eddies (indicated in figure 6.13a at $\psi = 45°$) of this helical mode reside on the circle of core-radius for all the vortex ages without modifying the structure of the helical mode. Therefore, this mode in figure 6.13a exhibits a linear behavior, as in the non-linear regime such an instability mode would undergo either a rotation [82] or modification in its structure [80] (which is not observed here). Using the GC technique, the

structure of the helical mode (figure 6.13b) is significantly different (at any ψ) from that of the Γ_1 technique (figure 6.13a) especially inside the circle of core-radius. In addition to this, the helical mode lacks an organized evolution using the GC method.

Having seen that the spatial structure of the helical mode is significantly effected by the GC technique, its effect on the double helical mode is also examined. Findings from the Γ_1 method in figure 6.14a are duplications of the findings in figure 4.15, where, like the helical mode, even the four-lobed structure of $m = 2$ mode was demonstrated earlier to be one of the modes of the elliptic instability. Once again, pairs of co-rotating eddies (indicated in figure 6.14a) at $\psi = 90°$ appear to merge with the increasing vortex age, thereby slightly modifying the structure of the double-helical mode (non-linear mode of the elliptic instability). A single elongated eddy from each such pair is evident in figure 6.14a at $\psi = 495°$. Using the GC technique, the structure of the double helical mode (figure 6.14b) is significantly different (at any ψ) from that of the Γ_1 technique (figure 6.14a). For example, while each lobe at $\psi = 90°$ in the Γ_1 method comprises a pair of counter-rotating eddies (radially separated), only a single eddy per lobe is manifest in the GC method.

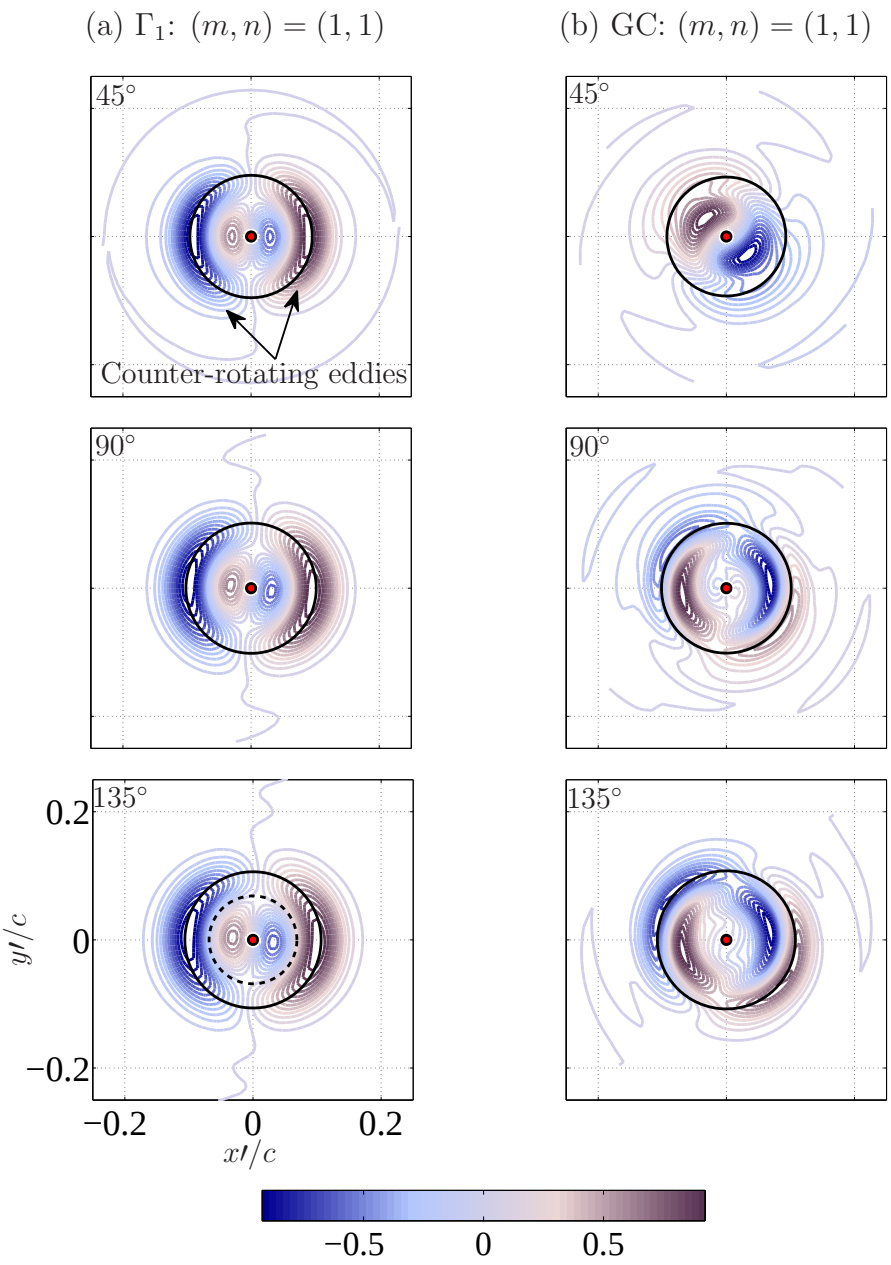

Figure 6.13: Continued on next page and caption provided at the end of the figure.

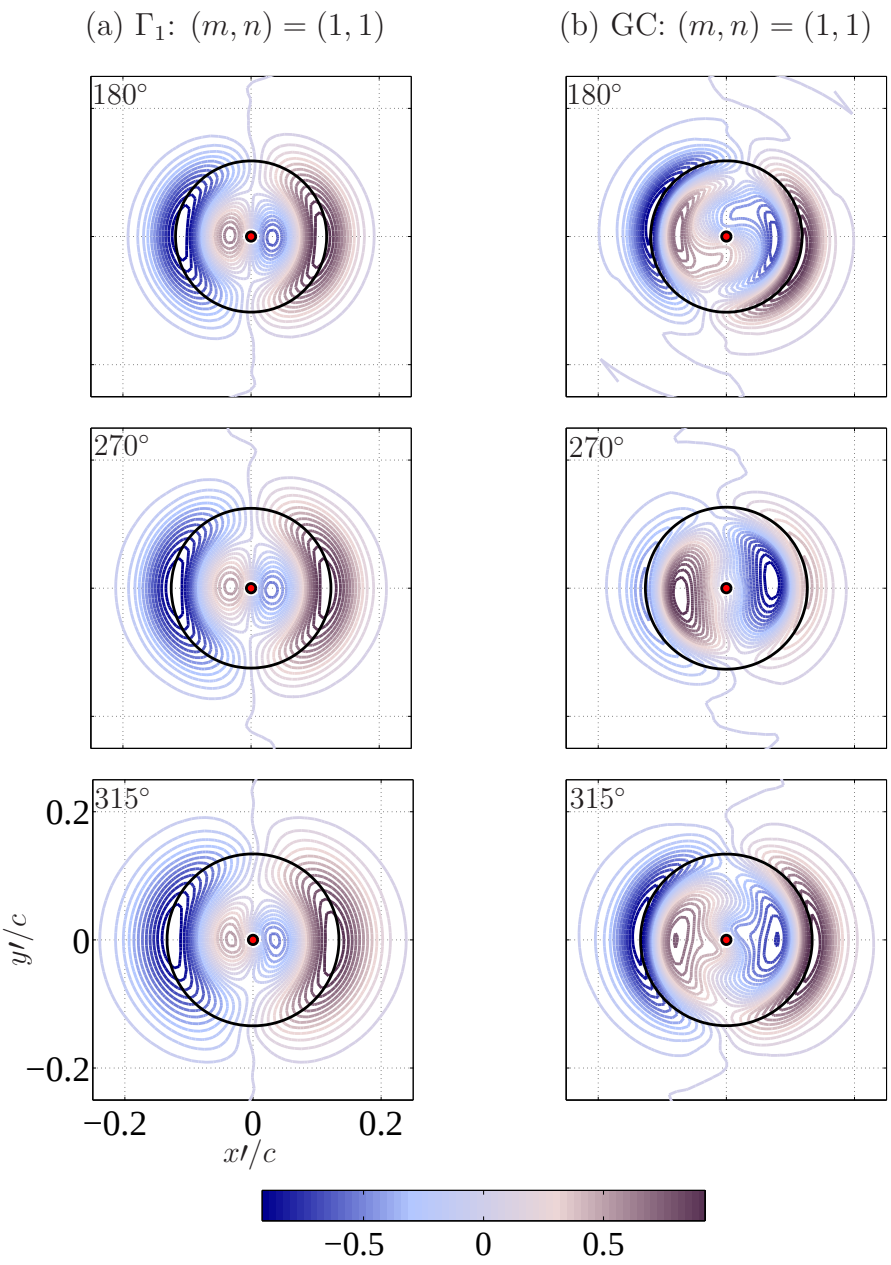

Figure 6.13: Continued on next page and caption provided at the end of the figure.

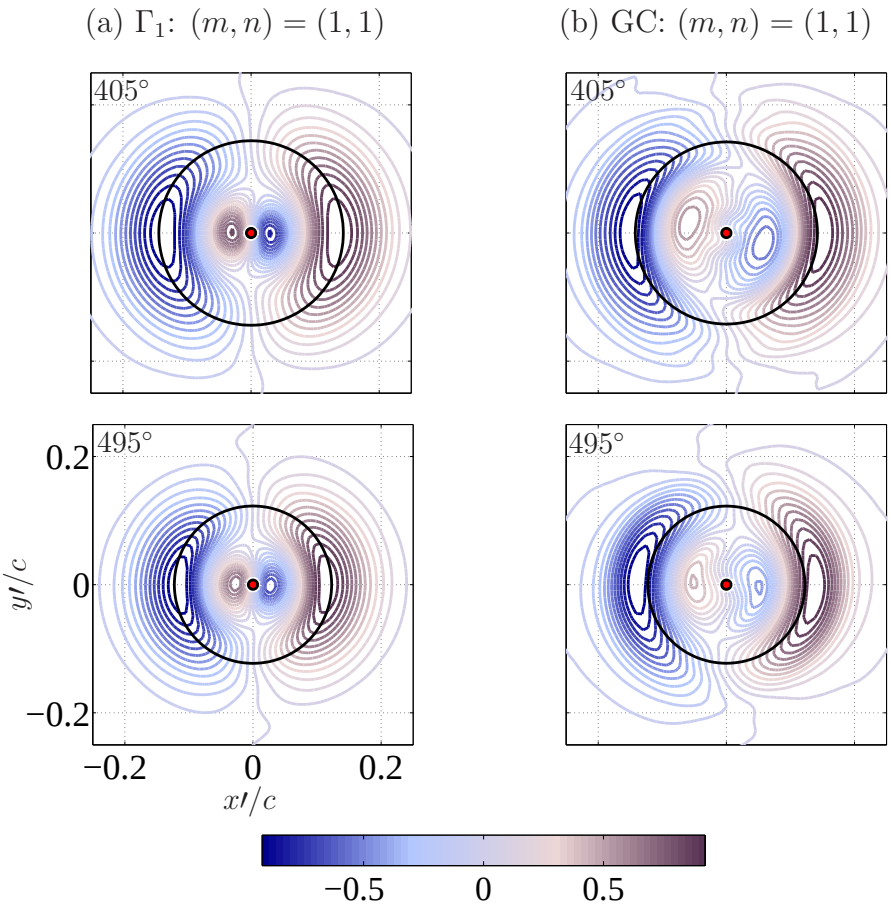

Figure 6.13: Contours of the real component of the axial vorticity of the helical mode $(m,n) = (1,1)$ at $\psi = 45° - 495°$. Circles of mean core-radius (__) are indicated.

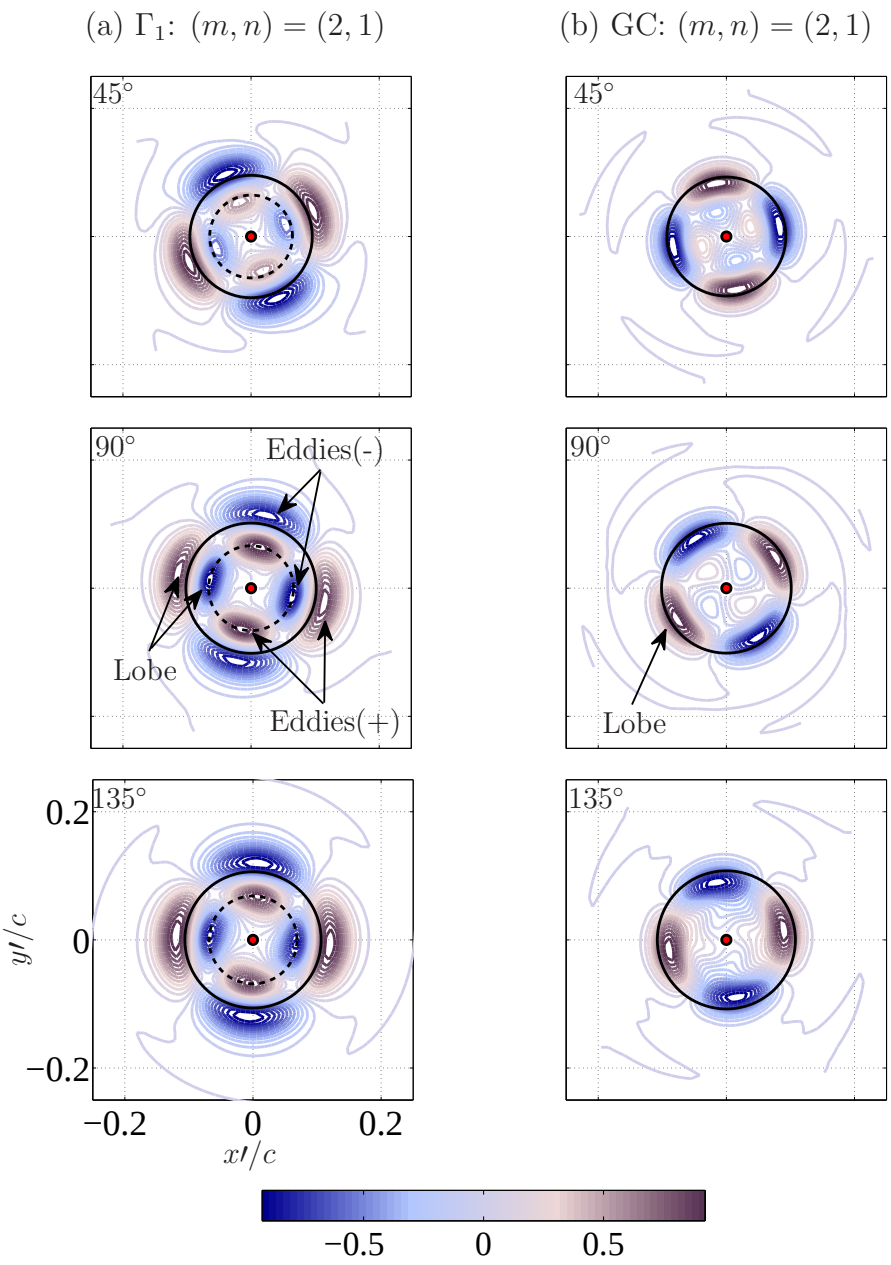

Figure 6.14: Continued on next page and caption provided at the end of the figure.

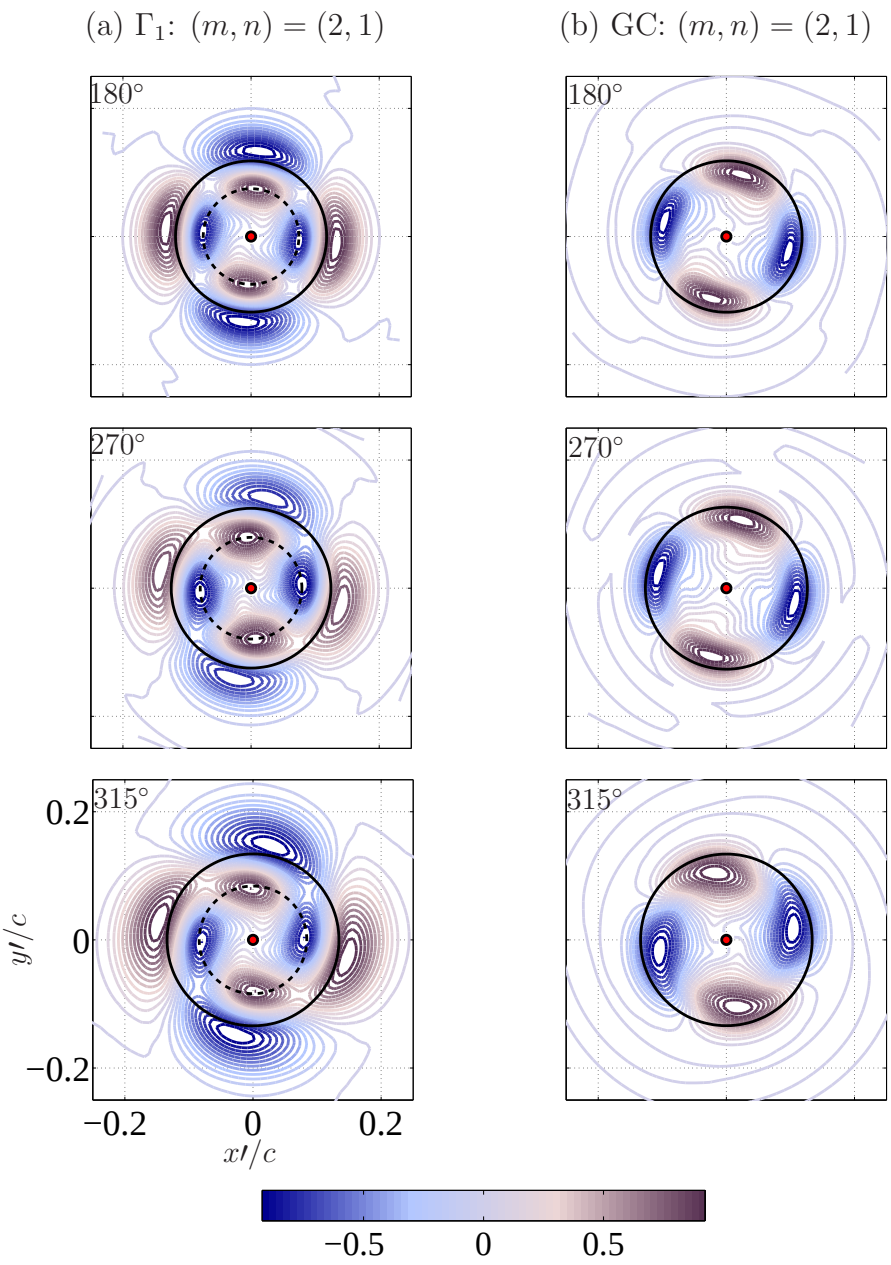

Figure 6.14: Continued on next page and caption provided at the end of the figure.

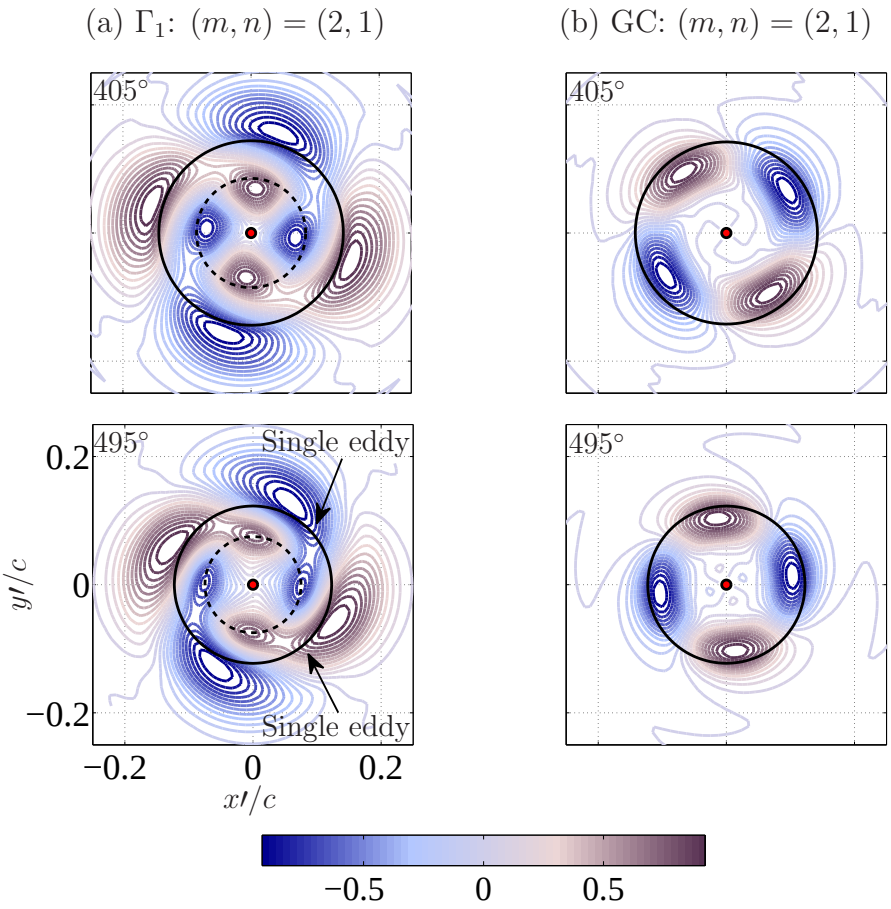

Figure 6.14: Contours of the real component of the axial vorticity of the helical mode $(m,n) = (2,1)$ at $\psi = 45° - 495°$. Circles of mean core-radius (__) are indicated.

6.2.1.1 Higher Fourier modes associated with the first $n = 1$ POD mode

Concerning the higher Fourier-azimuthal modes ($m \geq 3$) associated with the first $n = 1$ POD mode, radial profiles of the resolved energy (per unit mass) are shown in figure 6.15a, b using the Γ_1 and GC methods, respectively. These profiles (determined from Eq. 6.1) are once again normalized for each m. It is evident from figure 6.15a, b that, at any ψ, higher the Fourier-mode number, farther the location (from the vortex axis $r = 0$) where the energy peaks. This indicates smaller scales of turbulence occur farther away from the vortex axis. Also, for $\psi = 45°$, the peak energy appears to suddenly shift in space at around $r = 0.88r_c$. Based on the measurement resolution for the current setup ($L_m = 0.88$ mm), at $r = 0.88r_c$ up to $m = 15$ modes can be resolved. Therefore, at $\psi = 45°$ the sudden radial shift in peak energy, which is shown to occur about $m = 6$ (see figure 6.15), is not an indication of insufficient spatial resolution (at $r = 0.88r_c$) to resolve this Fourier-azimuthal mode. While such a discontinuity occurs at higher m with the increasing vortex age, the associated amount of radial shift in peak energy also gets smaller, which is attributed to turbulence diffusion.

Where the spatial structures of these higher Fourier modes ($m \geq 3$) are concerned, figure 6.16a, b shows for sample $\psi = 315°$ using the Γ_1 and GC techniques, respectively. For the sake of comparing these two centering techniques, only modes $m = 3$ to 8 are shown. It is evident that for each m in figure 6.16 the spatial structures are similar between the Γ_1 and GC techniques;

however, the eddies corresponding to the GC method are slightly smaller in size. Overall, the higher Fourier-azimuthal modes illustrated in figures 6.15 and 6.16 remain nearly uneffected by the choice of the centering technique.

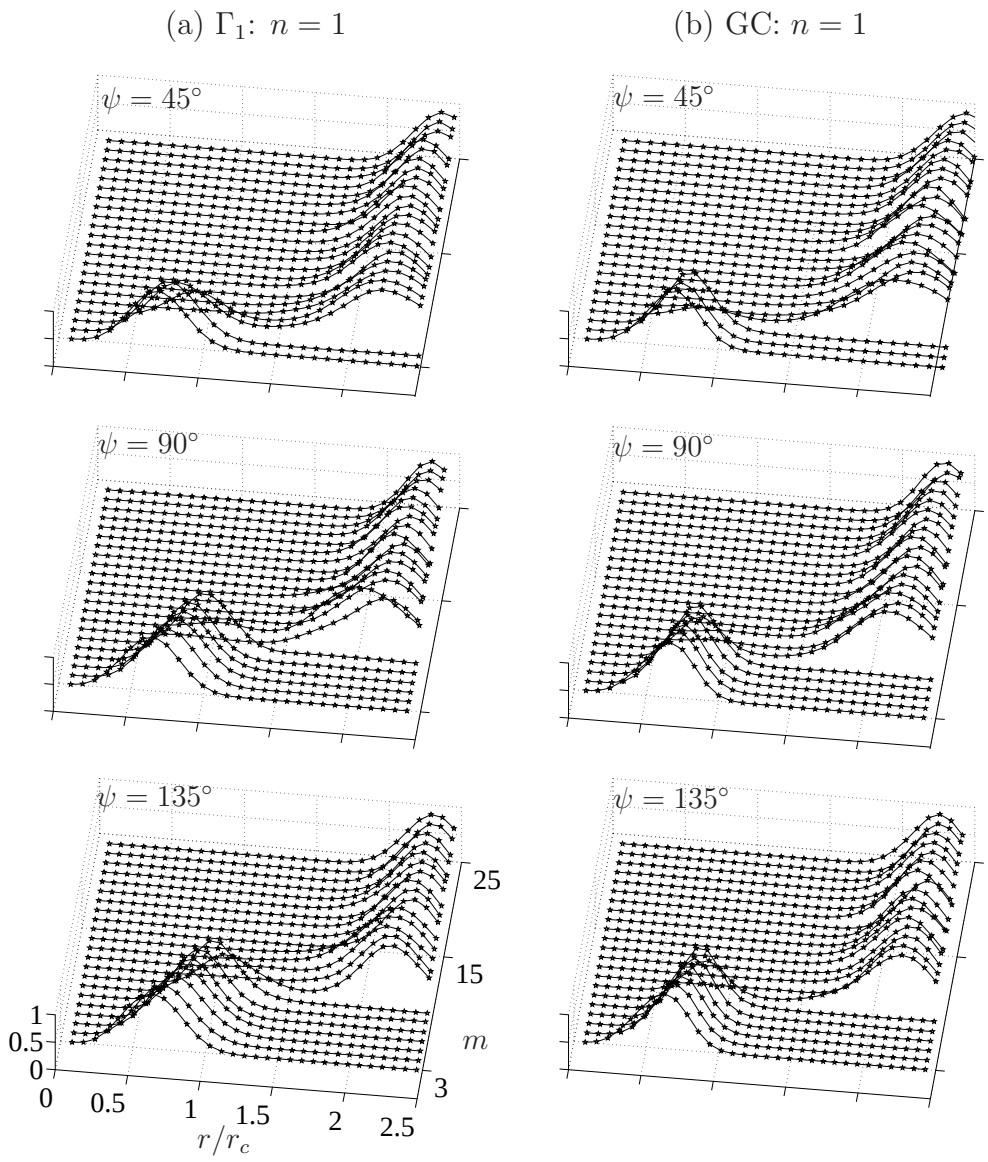

Figure 6.15: Continued on next page and caption provided at the end of the figure.

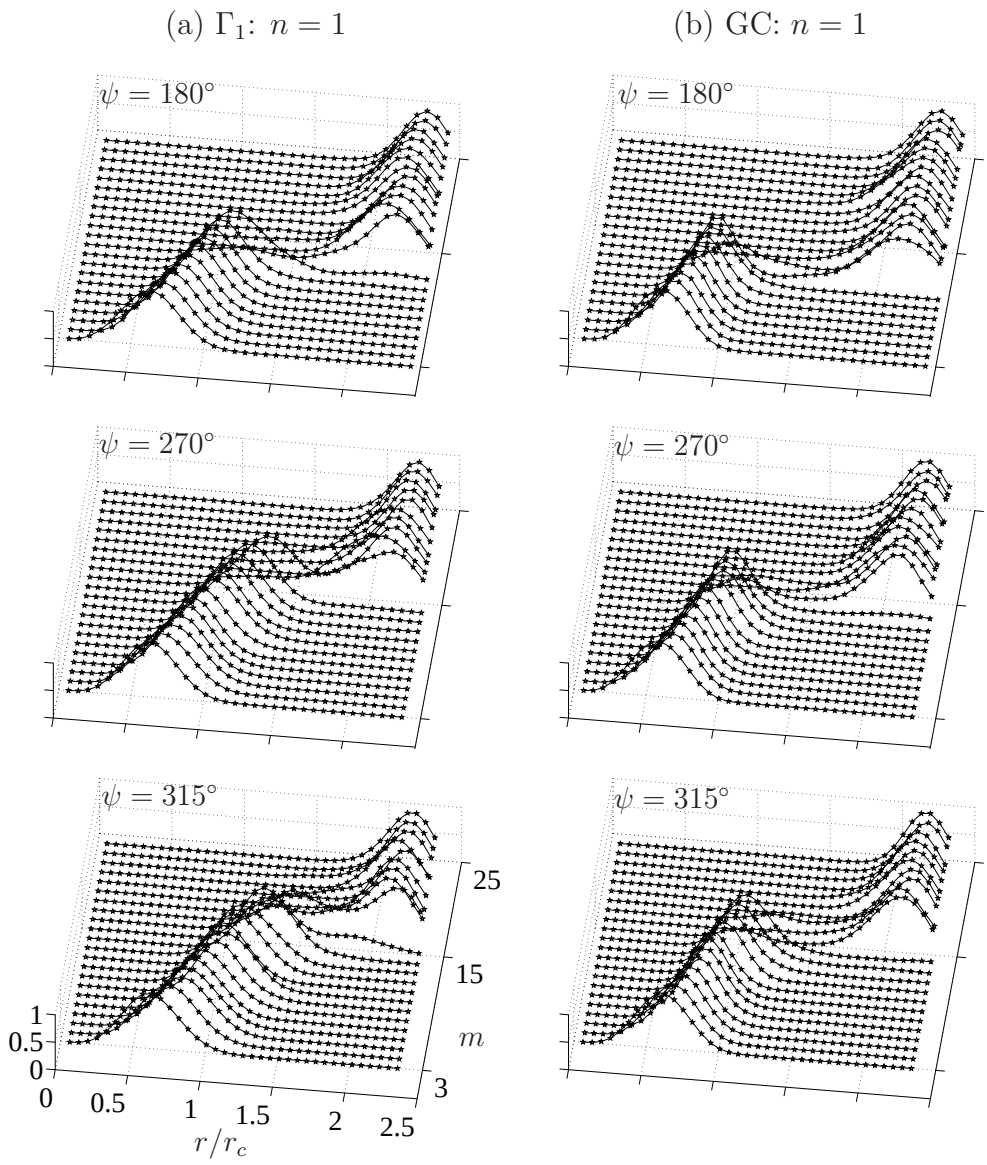

Figure 6.15: Continued on next page and caption provided at the end of the figure.

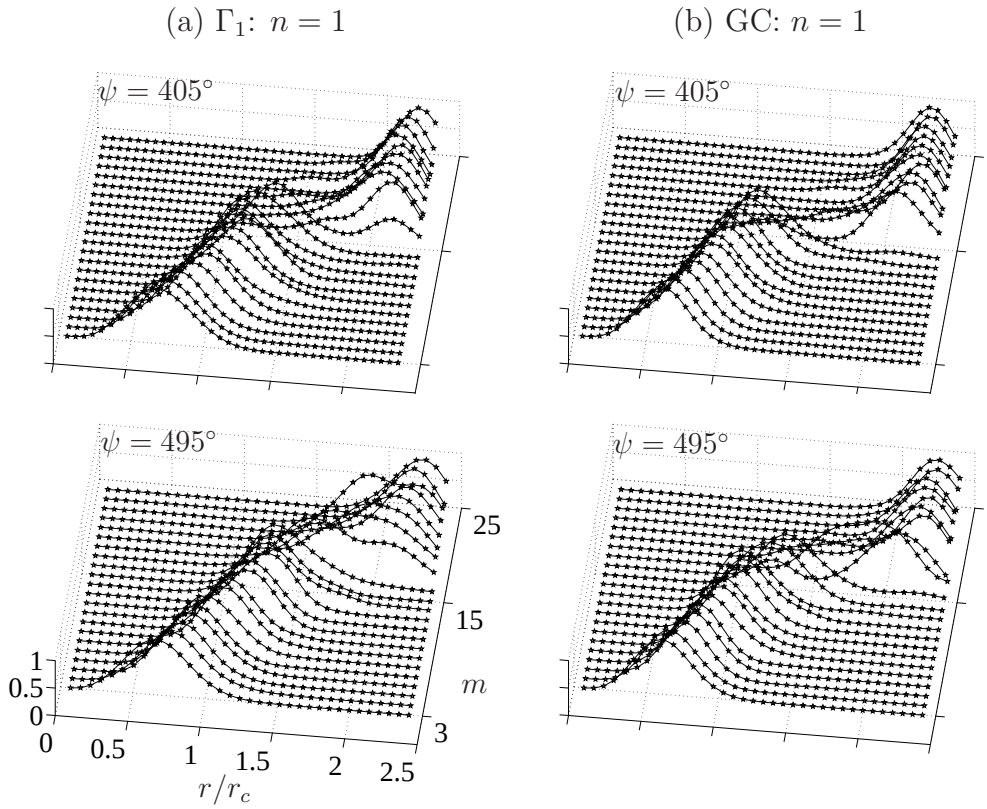

Figure 6.15: Radial profiles (in normalized form) of the resolved energy (per unit mass) of $m = 3$ to 25 associated with the first ($n = 1$) POD mode at $\psi = 45° - 495°$ using (a) Γ_1 and (b) GC methods.

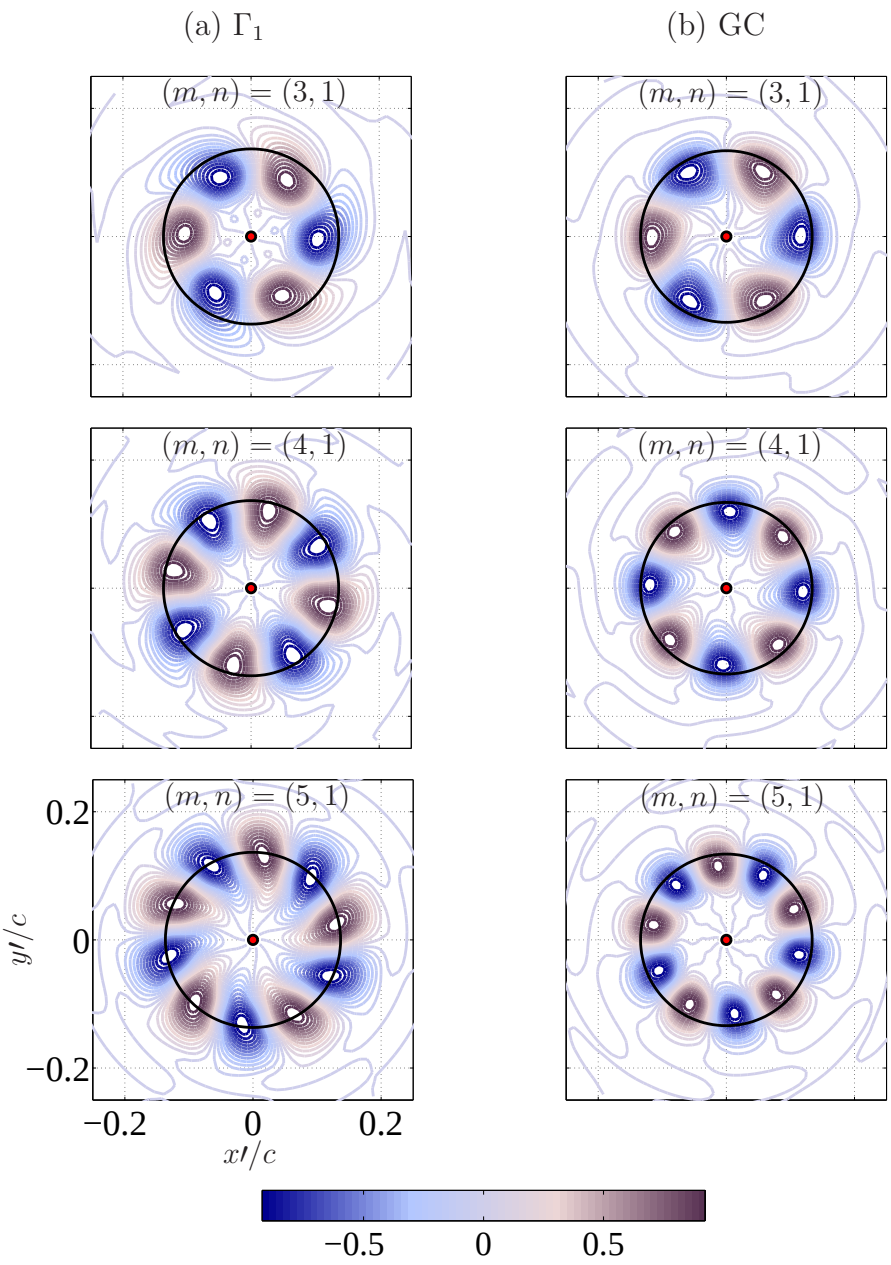

Figure 6.16: Continued on next page and caption provided at the end of the figure.

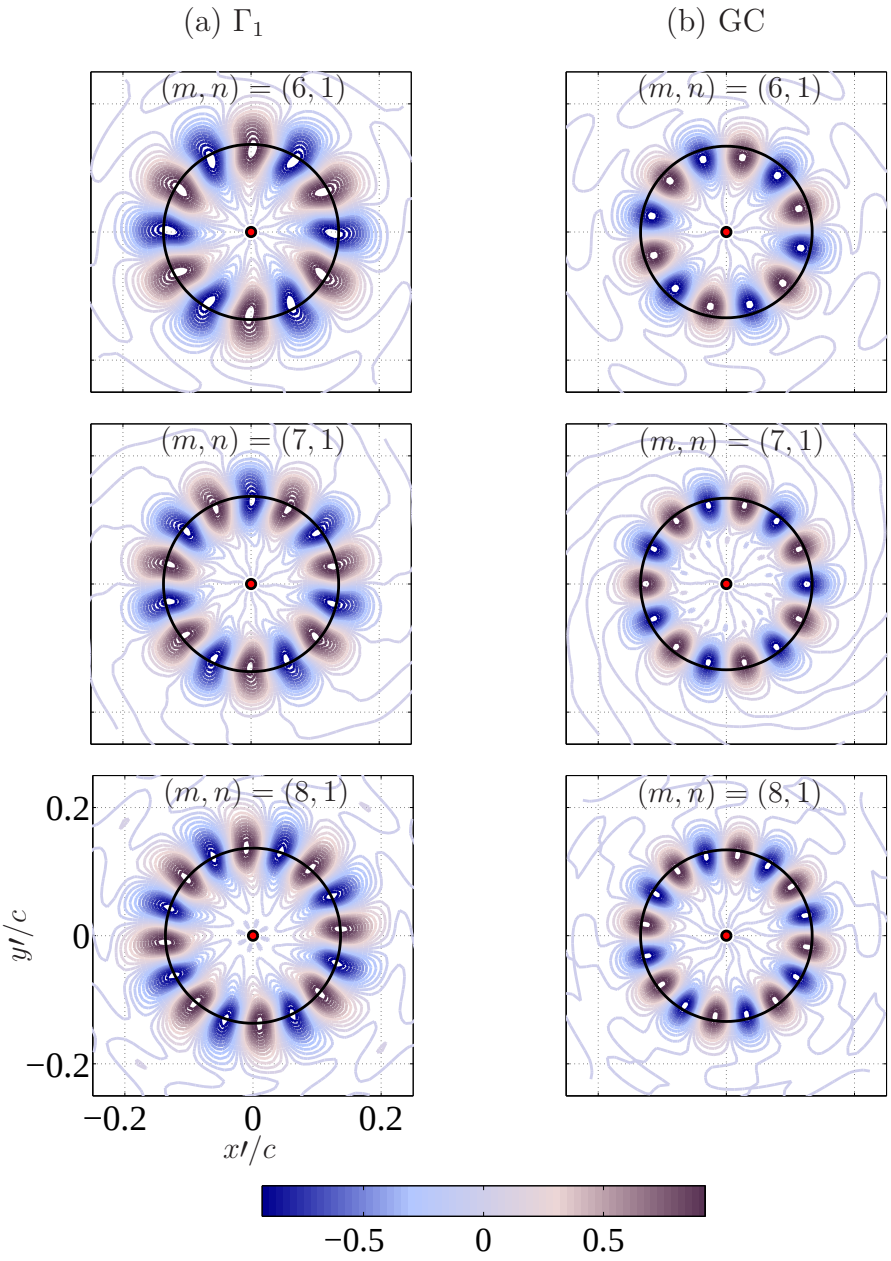

Figure 6.16: Contours of the real component of the axial vorticity of the higher Fourier modes ($m = 3$ to 8) associated with $n = 1$ at $\psi = 315°$ using (a) Γ_1 and (b) GC methods. Circles of mean core-radius (—) are indicated.

Chapter 7

Summary and future work

In this chapter, summary of the current work is described in § 7.1 and the recommendations for future work are provided in § 7.2.

7.1 Summary

Investigations were developed on a reduced-scale rotor to better understand the characteristics of tip vortices that play a very important role in the performance of helicopters. These vortices form compact filaments that are helical in geometry. Helical vortex filaments, under the influence of strain which is inherently induced by the proximity of the vortex to neighboring vortices along with curvature and torsional effects, are subject to three-dimensional long-wave instabilities. The strain also causes streamlines to deform elliptically on a plane perpendicular to the vortex axis, and so the vortex filament becomes the subject of the so called elliptic instability which is a three-dimensional short-wave instability. Elliptic instabilities have been studied analytically, numerically and experimentally in a variety of vortex flows. However, in the context of rotor tip vortices, there are limited quantitative experimental studies characterizing the behavior of these instabilities and over extended vortex

ages. Therefore, in the current study, investigations were developed on the short-wave instabilities as well as the organized turbulence that reside within the vortex produced by a rotor blade in hover. The vortex studied here was formed by a single-bladed rotor and was captured by way of particle image velocimetry (PIV). Proper orthogonal decomposition (POD) was utilized to flush out the more energetic features responsible for characterizing the bulk motions of the tip vortex and was performed over extended vortex ages.

In order to characterize the statistical properties of the tip vortex, the vortex center was identified using the Γ_1 method which is a non-divergence based scheme and hence the results were not corrupted by the noise due to velocity gradients. This is followed by obtaining the vortex wander, which is a scatter in the instantaneous positions of the vortex center (on a plane normal to the vortex axis) due to the inherent unsteadiness of the rotor wake. The wander was found to be anisotropic, which was in agreement with the findings in the literature. The growth of wander with the increasing vortex vortex age was analyzed along two perpendicular axes: along the preferred direction of wander (major axis) and normal to the preferred direction (minor axis). The wandering motion was shown to grow linearly along the minor axis, whereas along the major axis the wander did not show a continuous growth as it manifested a local minimum near $\psi = 360°$. It is postulated that this discontinuity is a consequence of long-wave instabilities with non-integer wave numbers.

After performing corrections for wander, some of the mean statistics of

the tip vortex were determined and compared to a sampling of data provided in the open literature that provided confidence in the measurements reported in this study. The measurements were found to satisfy the resolution criterion for determining the structural characteristics (such as the core-radius and turbulence fluctuations) of the tip vortex. As for the core-radius trends, up until the first rotor revolution, the core-radius was demonstrated to increase (monotonically from 10% to 15% of the blade chord) due to diffusion; however, after the first blade passage, the core-radius was shown to decrease due to vortex stretching caused by the oncoming blade in agreement with the findings in the literature.

In-plane velocity fluctuations (normal to the vortex axis) were found to peak within the vortex core; the turbulence kinetic energy per unit mass (TKE), based on the in-plane velocity, was illustrated to be zero at the vortex center (an inherent characteristic of a vortex flow) which demonstrates the accuracy of the Γ_1 method. A noticeable asymmetry in TKE was also observed within the vortex core and, over the range of vortex ages studied, the total resolved turbulence kinetic energy (Ξ) was found to vary between 2-8% of the total resolved mean kinetic energy associated with the tip vortex.

The most energetic features of the turbulence fluctuations that reside within the blade tip vortex were identified using the proper orthogonal decomposition. While it is customary for one to use the snapshot form of POD owing to the advantages of its computational efficiency, the classical form was employed in this study owing to the physical relevance of the Fourier modes.

In the classical form, the velocity fluctuations were first decomposed in azimuth using the Fourier-decomposition followed by the radial decomposition using POD. Also, this form of POD preserved the dependence of the azimuthal decomposition on the origin of the azimuthal angle thereby not imposing any homogeneity in velocity.

Using the classical POD, nearly 75% of the resolved energy was shown to reside in the first ($n = 1$) POD mode alone (comprising all the Fourier modes) for the entire range of vortex ages studied. Given the spatial grid resolution used to obtain the POD modes, this is a reflection of the organized events that characterize the active motions of the spiraling vortex filament. The POD energy spectrum was also shown to exhibit a $k^{-5/3}$ inertial range in the first decade of the POD modes, which is expected even for an inhomogeneous turbulence flow at high Reynolds number. As 75% of the resolved energy that was contained in the first POD mode was distributed amongst the Fourier-azimuthal modes, the Fourier energy spectrum was also analyzed. The findings revealed that the helical mode ($m = 1$) dominated the energy spectrum at all the vortex ages (except at $\psi = 45°$), followed by the axisymmetric ($m = 0$) and double helical ($m = 2$) modes. However, at $\psi = 45°$, the axisymmetric and helical modes were found to be equally dominant.

As for the spatial characteristics of the Fourier modes of the first ($n = 1$) POD mode, the axisymmetric mode ($m = 0$) was shown to resemble a vortex with viscous core at $\psi = 45°$. Therefore, the axisymmetric mode is associated with the roll-up of the vorticity sheet trailed from the rotor blade at early ages.

This explains the reason for its equal dominance as that of the helical mode at $\psi = 45°$. At higher vortex ages, once the roll-up process was complete, the axisymmetric mode was found to manifest features similar to that of an axisymmetric swirling jet, which further enhances the flow-entrainment and diffusion mechanisms. Due to the nature of the Fourier functions, non-zero Fourier modes such as the helical ($m = 1$) and double helical ($m = 2$) modes comprise both real and imaginary components. These components are identical but separate in orientation by $\pi/2m$. While the helical and double helical modes were shown to be associated with the elliptic instability, the helical mode was demonstrated to be the most unstable mode of the elliptic instability. At the earliest vortex age ($\psi = 45°$), the helical mode comprised two counter-rotating eddies residing on the circle of core-radius. As for the evolutionary behavior of this mode, the counter-rotating eddies remained centered on the mean core-radius for all the vortex ages without modifying the structure of the helical mode. Therefore, the helical mode exhibited a linear mode of the elliptic instability, since in a non-linear regime such an instability mode would undergo either a rotation or a modification in its structure. Concerning the double helical mode, the spatial structure was four-lobed in azimuth. This mode was found to undergo a slight modification in its structure with the increasing vortex age. Therefore, unlike the helical mode, the double helical mode exhibited a non-linear mode of the elliptic instability. Furthermore, it was shown that a combination of at least the above axisymmetric, helical and double helical modes of the first POD mode were responsible for producing

distinguishable asymmetries in the turbulence kinetic energy per unit mass (TKE) inside the tip vortex.

While the helical mode of the first ($n = 1$) POD mode was a linear mode of the elliptic instability, for the second ($n = 2$) POD mode the helical mode displayed a non-linear behavior with low-vorticity fluid stripping azimuthally and radially outward from the two-counter rotating eddies thereby modifying the structure of the mode. Fluid stripping was also observed in the double helical mode (of the second POD mode). It is postulated that the stripped fluid moves radially away form the vortex axis and breaks down into small scales.

Having observed the low-dimensional features of the tip vortex using the classical POD, comparisons with that of the snapshot POD were also provided, as the latter approach is computationally more efficient than the former. Using the snapshot POD, the first three ($n_s = 1, 2$ and 3) POD modes of this technique comprised nearly 70% of the resolved energy which again reflects the presence of highly organized motions within the tip vortex over the range of vortex ages studied. As for the spatial structures of the first three ($n_s = 1, 2$ and 3) dominant modes, at $\psi = 45°$, $n_s = 1$ was shown to resemble a vortex with viscous core, thereby becoming the counterpart of the axisymmetric mode $(m, n) = (0, 1)$ (classical POD); $n_s = 2$ and $n_s = 3$ formed the counterparts of the real and imaginary components, respectively, of the helical mode $(m, n) = (1, 1)$ (classical POD). However, at higher ages, once the roll-up process was complete, the first two modes ($n_s = 1$ and $n_s = 2$) resembled the

real and imaginary components of the helical mode $(m, n) = (1, 1)$ (classical POD); the $n_s = 3$ mode formed the counterpart of the axisymmetric mode $(m, n) = (0, 1)$, which behaved as a swirling jet.

As the findings revealed that the helical mode $(m, n) = (1, 1)$ (classical POD) had a counterpart in the snapshot POD, the evolutionary behavior was also compared. While in the classical POD the helical mode comprised two counter-rotating eddies residing on the circle of core-radius, its counterpart in the snapshot POD comprised two counter-rotating eddies that remained centered on the mean core-boundary for all the vortex ages in the measurement envelope. Therefore, the most unstable mode of the elliptic instability as seen by snapshot technique was also in the linear regime. Furthermore, the resolved energy residing in the axisymmetric $(m, n) = (0, 1)$ and helical $(m, n) = (1, 1)$ modes (classical POD), respectively, along with their counterparts of the snapshot POD was also analyzed for the range of vortex ages studies. The findings revealed that the resolved energy contributions from these large-scale motions were also consistent between these two forms of POD. As for the asymmetries in TKE inside the tip vortex, the snapshot POD was found to require less modes when compared to that of the classical POD. Nevertheless, the classical technique was preferred in this study owing to the easier interpretation of the Fourier-azimuthal modes.

Since the low-dimensional characterization of the velocity fluctuations inside the tip vortex was executed after performing corrections for vortex wander, sensitivity of POD to the choice of the wander correction technique was

also analyzed. As the Γ_1 method aligned the regions of the inner core by producing zero in-plane turbulence at the vortex center (an inherent characteristic of a vortex flow), a second approach was examined which positioned vortices such that the regions outside the core were aligned; in the latter approach, each vortex was aligned by way of its geometric center (GC). This new centering technique was found not to effect the trends of the core-radius, which were observed earlier using the Γ_1 method. However, it was found to significantly effect the turbulence kinetic energy per unit mass (TKE) inside the tip vortex as it produced more symmetry (in TKE) with less turbulence fluctuations (except near the vortex axis); at the vortex center, the GC approach was shown to introduce artificially elevated turbulence fluctuations. Overall, by estimating the total resolved turbulence kinetic energy (Ξ), the GC method generated lower resolved energy than that of the Γ_1 technique over the range of vortex ages studied.

As for the low-dimensional characterization of the turbulence fluctuations (obtained using the GC method) inside the tip vortex, the classical form of POD was employed, once again, due to the easier interpretation of the Fourier modes. While the Γ_1 technique revealed 75% of the resolved energy residing in the first ($n = 1$) POD mode (over the range of vortex ages studied), the GC method showed a different quantum residing in the first POD mode. Nevertheless, using the latter approach, the POD energy spectrum demonstrated a $k^{-5/3}$ inertial range in the first decade of POD modes, which was observed earlier using the Γ_1 technique.

With regard to the Fourier energy spectrum associated with the first ($n = 1$) POD mode, the GC technique produced exactly the opposite behavior than the Γ_1 method where the axisymmetric ($m = 0$) and helical ($m = 1$) modes contributions were concerned; using the GC method, at early ages ($\psi = 45°$), the turbulence kinetic energy was governed entirely by the axisymmetric mode which immediately changed to equal levels of contribution from the axisymmetric and helical modes at all other vortex ages. Nevertheless, the additional findings from the Fourier energy spectrum (associated with the first POD mode) revealed that both the centering techniques produced similar rates of energy convergence within the first decade of the azimuthal modes.

Concerning the spatial characteristics, the GC method demonstrated a similar structure of the axisymmetric mode $(m, n) = (0, 1)$ as that of the Γ_1 technique; however, at higher vortex ages, the former approach shifted the position of the peak circulation of the swirling jet mode, radially towards the vortex axis, from that of the latter. The spatial structures of the helical ($m = 1$) and double helical ($m = 2$) modes of the first ($n = 1$) POD mode were found to be significantly affected by the choice of the centering technique, where the GC technique produced a lack of organized motion in their evolutionary behavior. Also, the artificially elevated velocity fluctuations (at the vortex center), which were obtained using the GC approach, were found to be caused predominantly by the helical mode $(m, n) = (1, 1)$. While the higher azimuthal modes were observed in the outer portions of the vortex, they appeared to be minimally affected by the choice of the wander correction technique used.

7.2 Future work

Following are the recommendations for further work based on the findings of the current study using the Γ_1 technique.

1. Measurements in the current study were not time-resolved. It would be interesting to obtain time-resolved PIV measurements on the rotor tip vortex filaments in order to quantitatively determine dominant long-wave instabilities (by estimating the integral length scales and time scales), as these instabilities are equally important as the short-wave instabilities in the breakdown of tip vortices.

2. In the current set of measurements, vortex roll-up was seen only at the earliest vortex age ($\psi = 45°$) measured, at which the axisymmetric and helical modes (associated with the first POD) were found to be equally dominant (using the Γ_1 technique). This raises concerns if such an equal dominance between these modes persists throughout the entire evolution of the vortex roll-up. Therefore, in order to study the evolutionary behavior of this roll-up process, it is essential to acquire measurements at multiple vortex ages in the first quarter of the rotor revolution.

3. The low-dimensional characteristics of the turbulence fluctuations observed here within the tip vortex suggests that the tip vortex was active (and not completely diffused) over the range of vortex ages studied ($\psi = 45°$ to $585°$). As an extension to the current work, it would be interesting to see how the short-wave instabilities that were found to

reside within the tip vortex, in combination with the long-wave instabilities, would completely diffuse the vortex. In order to do this, it would be essential to acquire measurements at higher vortex ages ($\psi > 585°$) using a higher resolution camera (so as to provide sufficient measurement resolution for resolving the structural characteristics of the tip vortex, while also providing provisions for the vortex wander).

4. The rotor blade in the current study was manufactured with a square tip. It would be worth investigating how by changing the shape of the blade tip would influence the low-dimensional characteristics of the tip vortex, as the blade tip plays a very important role in the performance of helicopters.

5. As an extension to the current study, it would also be interesting to study the low-dimensional characteristics of the tip vortex (using POD) in ground effect as it might find a very useful application in the helicopter brownout. Once again, the evolutionary characteristics of the short-wave instabilities (and any organized turbulence), in combination with the long-wave instabilities, can be studied to see how they completely diffuse the tip vortex in ground effect. Subsequently, comparisons with the observations in the absence of ground effect can also be made.

Bibliography

[1] R. J. Adrian. Particle-imaging techniques for experimental fluid mechanics. *Annu. Rev. Fluid. Mech.*, 23: 261–304, 1991.

[2] S. C. C. Bailey and S. Tavoularis. Measurements of the velocity field of a wing-tip vortex, wandering in grid turbulence. *J. Fluid Mech.*, 601: 281–315, 2008.

[3] G. R. Baker, S. J. Barker, K. K. Bofah and P. G. Saffman. Laser anemometer measurements of trailing vortices in water. *J. Fluid Mech.*, 65(2): 325–336, 1974.

[4] P. R. Bandyopadhyay, D. J. Stead and L. A. Robert. Organized nature of a turbulent trailing vortex. *AIAA J.*, 29(10): 1627–1633, 1991.

[5] G. K. Batchelor. Axial flow in trailing line vortices. *J. Fluid Mech.*, 20(4): 645–658, 1964.

[6] B. J. Bayly. Three-dimensioanal instability of elliptical flow. *Phys. Rev. Lett.*, 57(17): 2160–2163, 1986.

[7] S. J. Beresh, J. F. Henfling and R. W. Spillers. Meander of a fin trailing vortex and the origin of its turbulence. *Exp. Fluids*, 49: 599–611, 2010.

[8] G. Berkooz, P. Holmes and J. L. Lumley. The proper orthogonal decomposition in the analysis of turbulent flows. *Annu. Rev. Fluid Mech.*, 25: 539–575, 1993.

[9] M. J. Bhagwat and J. G. Leishman. Stability analysis of helicopter rotor wakes in axial flight. *J. Am. Helicopter Soc.*, 45(3): 165–178, 2000a.

[10] M. J. Bhagwat and J. G. Leishman. Correlation of helicopter rotor tip vortex measurements. *AIAA J.*, 38(2): 301–308, 2000b.

[11] D. M. Birch and N. Martin. Tracer particle momentum effects in vortex flows. *J. Fluid Mech.*, 723: 665–691, 2013.

[12] J. Boersma and D. H. Wood. On the self-induced motion of a helical vortex. *J. Fluid Mech.*, 384: 263–280, 1999.

[13] J. H. Citrinity and W. K. George. Reconstruction of the global velocity field in the axisymmetric mixing layer utilizing the proper orthogonal decomposition. *J. Fluid Mech.*, 418: 137–166, 2000.

[14] A. D. D. Craik. The stability of unbounded two- and three-dimensional flows subject to body forces: some exact solutions. *J. Fluid Mech.*, 198: 275–292, 1989.

[15] S. C. Crow. Stability theory for a pair of trailing vortices. *AIAA J.*, 8(12): 2172–2179, 1970.

[16] W. J. Devenport, M. C. Rife, S. I. Liapis and G. J. Follin. The structure and development of a wing-tip vortex. *J. Fluid Mech.*, 312: 67–106, 1996.

[17] S. Discetti and R. J. Adrian. High accuracy measurement of magnification for monocular PIV. *Meas. Sci. Tech.*, 23, 117001, 2012.

[18] Flow master product-manual for DaVIS*v*7.2. *LaVision*, 1105011-4, 2007.

[19] Y. Fukumoto and Y. Hattori. Curvature instability of a vortex ring. *J. Fluid Mech.*, 526: 77–115, 2005.

[20] Y. Fukumoto and V. L. Okulov. The velocity induced by a helical vortex tube. *Phys. Fluids*, 17(10), 107101, 2005.

[21] L. J. Garodz. Federal aviation administration full-scale aircraft vortex wake turbulence flight test investigations: past, present and future. *AIAA paper* 71-97, 1971.

[22] E. B. Gledzer and V. M. Ponomarev. Instability of bounded flows with elliptical streamlines. *J. Fluid Mech.*, 240: 1–30, 1992.

[23] M. N. Glauser and W. K. George. Orthogonal decomposition of the axisymmetric jet mixing layer including azimuthal dependence. *Advances in Turbulence*, ed. G. Comte-Bellot and J. Mathieu: 357–366, Springer, 1987.

[24] L. Graftieaux, M. Michard and N. Grosjean. Combining PIV, POD and vortex identification algorithms for the study of unsteady turbulent swirling flows. *Meas. Sci. Tech.*, 12: 1422–1429, 2001.

[25] I. Grant. Particle image velocimetry. *Proceedings of the Institution of Mechanical Engineers*, 211(C): 55–76, 1997.

[26] P. Hall. Taylor-Gortler vortices in fully developed boundary layer flows. *J. Fluid Mech.*, 124: 475–494, 1982.

[27] Y. O. Han, J. G. Leishman and A. J. Coyne. Measurements of the velocity and turbulent structure of a rotor tip vortex. *AIAA J.*, 35(3): 477–485, 1997.

[28] R. Hartley and A. Zissermann. Multiple view geometry in computer vision. *Cambridge University Press*, UK, ISBN 0521623049, 1997.

[29] Y. Hattori and Y. Fukumoto. Short-wavelength stability analysis of a helical vortex tube. *Phys. Fluids*, 21, 014104, 2009.

[30] Y. Hattori and Y. Fukumoto. Modal stability analysis of a helical vortex tube with axial flow. *J. Fluid Mech.*, 738: 222–249, 2014.

[31] A. L. Heyes, R. F. Jones and D. A. R. Smith. Wandering of wing-tip vortex. In *International symposium on applications of laser techniques to fluid mechanics, Lisbon, Portugal*, 2004.

[32] R. M. Huffaker, A. V. Jelalian and J. A. L. Thompson. Laser doppler system for detection of aircraft trailing vortices. *Proc. IEEE*, 58: 322–326, 1970.

[33] J. C. R. Hunt, A. A. Wray and P. Moin. Eddies, stream, and convergence zones in turbulent flows. *Center for Turbulence Research Report*, S88: 193–208, 1988.

[34] Imaging tools product-manual for DaVISv7.2. *LaVision*, 1005xxx, 2009.

[35] J. Jimenez. Stability of a pair of co-rotating vortices. *Phys. Fluids*, 18(11): 1580–1581, 1975.

[36] D. Jung, S. Gamard and W. K. George. Downstream evolution of the most energetic modes in a turbulent axisymmetric jet at high Reynolds number. Part 1. The near-field region. *J. Fluid Mech.*, 514: 173–204, 2004.

[37] A. Karpatne, J. Sirohi, S. M. Mula and C, E. Tinney. Vortex ring model of tip vortex aperiodicity in a hovering helicopter rotor. *J. Fluids Engg.*, 136(7), 071104, 2014.

[38] R. R. Kerswell. Elliptic instability. *Annu. Rev. Fluid Mech.*, 34: 83–113, 2002.

[39] K. Kindler, K. Mulleners, H. Richard, B. G. van der Wall and M. Raffel. Aperiodicity in the near field of full-scale rotor blade tip vortices. *Exp. Fluids*, 50(6): 1601–1610, 2010.

[40] A. R. Kriebel. Particle trajectories in a gas centrifuge. *J. Basic Engg.*, 83(3): 333–339, 1961.

[41] L. Lacaze. K. Ryan and S. L. Dizes. Elliptic instability in a strained Batchelor vortex. *J. Fluid Mech.*, 577: 341–361, 2007.

[42] H. Lamb. Hydrodynamics. *Sixth edition Cambridge University Press,* Cambridge, UK, 1932.

[43] M. J. Landman and P. G. Saffman. The three-dimensional instability of strained vortices in a viscous fluid. *Phys. Fluids*, 30: 2339–2342, 1987.

[44] E. Levich and A. Tsinober. On the role of helical structures in three-dimensional turbulent flow. *Phys. Lett.*, 93A(6): 293–297, 1983.

[45] Y. Levy, D. Degani and A. Segineer. Graphical visualization of vortical flows by means of helicity. *AIAA J.*, 28(8): 1347–1352, 1990.

[46] T. Leweke and C. H. K. Williamson. Cooperative elliptic instability of a vortex pair. *J. Fluid Mech.*, 360: 85–119, 1998.

[47] T. Leweke and C. H. K. Williamson. Experiments on long-wavelength instability and reconnection of a vortex pair. *Phys. Fluids*, 23, 024101, 2011.

[48] T. Leweke, H. U Quaranta, H. Bolnot, F. J. Blanco-Rodriguez and S. Le Dizes. Long- and short-wave instabilities in helical vortices. *Journal of Physics: Conference Series*, 524, 012154, 2014.

[49] J. G. Leishman. Seed particle dynamics in tip vortex flows. *J. Aircraft*, 33(4): 823–825, 1996.

[50] J. G. Leishman, A. Baker and A. Coyne. Measurements of rotor tip vortices using three-component laser doppler velocimetry. *J. Am. Helicopter Soc.*, 41(4): 342–353, 1996.

[51] J. G. Leishman. Measurements of the aperiodic wake of a hovering rotor. *Exp. Fluids*, 25: 352–361, 1998.

[52] H. Liang and T. Maxworthy. An experimental investigation of swirling jets. *J. Fluid Mech.*, 525: 115–159, 2005.

[53] J. L. Lumley. The structure of inhomogeneous turbulent flows. In *Atmospheric Turbulence and Radio Wave Propagation*, (ed. A. M. Yaglom & V. I. Tatarsky): 166–178, Nauka, Moscow, 1967.

[54] W. V. R. Malkus. An experimental study of global instabilities due to the tidal (elliptical) distortion of a rotating elastic cylinder. *Geophys. Astrophys. Dyn.*, 48: 123–134, 1989.

[55] P. B. Martin, J. G. Leishman, G. J. Pugliese and S. L. Anderson. Stereoscopic PIV measurements in the wake of a hovering helicopter rotor. In *Am. Helicopter Soc. Forum 56*, 2000.

[56] K. W. McAlister. Rotor wake development during the first rotor revolution. In *Am. Helicopter Soc. Forum 59*, 2003.

[57] K. W. McAlister. Rotor wake development during the first rotor revolution. *J. Am. Helicopter Soc.*, 59(4): 371–390, 2004.

[58] C. D. Meinhart and S. T. Wereley. Theory of diffraction-limited resolution in micro particle image velocimetry. *Meas. Sci. Technol.*, 14: 1047–1053, 2003.

[59] A. Melling. Tracer particles and seeding for particle image velocimetry. *Meas. Sci. Technol.*, 8: 1406–1416, 1997.

[60] P. Meunier and T. Leweke. Elliptic instability of a co-rotating vortex pair. *J. Fluid Mech*, 533: 125–159, 2005.

[61] D. W. Moore and P. G. Saffman. The instability of a straight vortex filament vortex field in a strain field. *Proc. R. Soc. Lond. A.*, 346: 413–425, 1975.

[62] R. D. Moser. Kolmogorov inertial range spectra for inhomogeneous turbulence. *Phys. Fluids*, 6(2): 794–801, 1994.

[63] S. M. Mula, J. H. Stephenson, C. E. Tinney and J. Sirohi. Dynamical and evolutionary characteristics of the tip vortex from a four-bladed rotor in hover. In *Am. Helicopter Soc. Forum 68*, 2012.

[64] S. M. Mula, J. H. Stephenson, C. E. Tinney and J. Sirohi. Dynamical characteristics of the tip vortex from a four-bladed rotor in hover. *Exp. Fluids*, 54, 1600, 2013.

[65] J. Nogueira, A. Lecuona and P. A. Rodriguez. Data validation false vectors correction and derived magnitudes calculation on PIV data. *Meas. Sci. Technol.*, 8(12): 1493–1501, 1997.

[66] C. V. Ohanian, G. J. McCauley and O. Savas. A visual study of vortex instabilities in the wake of a rotor in hover. *J. Am. Helicopter Soc.*, 57, 042005, 2012.

[67] R. T. Pierrehumbert. Universal short-wave instability of two-dimensional eddies in an inviscid fluid. *Phys. Rev. Lett.*, 57: 2157–2159, 1986.

[68] W. R. C. Phillips and J. A. H. Graham. Reynolds-stress measurements in a turbulent trailing vortex. *J. Fluid Mech.*, 147: 353–371, 1984.

[69] M. Raffel, C. Willert and J. Kompenhans. Particle image velocimetry, 1998. Springer.

[70] S. Ragab, and M. Sreedhar. Numerical simulation of vortices with axial velocity deficits. *Phys. Fluids*, 7: 549–558, 1995.

[71] M. Ramasamy and J. G. Leishman. Interdependence of diffusion and straining of helicopter blade tip vortices. *J. Aircraft*, 41(5): 1014–1024, 2004.

[72] M. Ramasamy and J. G. Leishman. Benchmarking PIV with LDV for rotor wake vortex flows. *AIAA Paper* 2006-3479, 2006.

[73] M. Ramasamy, E. L. Timothy and J. G. Leishman. Flowfield of a rotating-wing micro air vehicle. *J. Aircraft*, 44(4): 1236–1244, 2007.

[74] M. Ramasamy, B. Johnson, T. Huismann and J. G. Leishman. Digital particle image velocimetry measurements of tip vortex characteristics using

an improved aperiodicity correction. *J. Am. Helicopter Soc.*, 54: 1–13, 2009a.

[75] M. Ramasamy, B. Johnson and J. G. Leishman. Turbulent tip vortex measurements using dual-plane stereoscopic particle image velocimetry. *AIAA J.*, 47(8): 1826–1840, 2009b.

[76] R. L. Ricca. The effect of torsion on the motion of a helical vortex filament. *J. Fluid Mech.*, 273: 241–259, 1994.

[77] H. Richard, B. G. Van der Wall, M. Raffel and M. Thimm. Application of PIV techniques for rotor blade tip vortex characterization. *New Res. in Num. and Exp. Fluid Mech. (NNFM VI)*, 96: 446–453, 2008.

[78] A. C. Robinson and P. G. Saffman. Three dimensional stability of an elliptical vortex in a straining field. *J. Fluid Mech.*, 142: 451–466, 1984.

[79] C. Roy, T. Leweke, M. C. Thompson and K. Hourigan. Experiments on the elliptic instability in vortex pairs with axial core flow. *J. Fluid Mech.*, 677: 383–416, 2011.

[80] N. Schaeffer and S. L. Dizes. Nonlinear dynamics of the elliptic instability. *J. Fluid Mech.*, 646: 471–480, 2010.

[81] M. P. Scully. A method of computing helicopter vortex wake distortion. *Massachussets Institute of Technology*, ASRL TR 138-1, 1967.

[82] D. Sipp. Weakly nonlinear saturation of short-wave instabilities in a strained lamb-oseen vortex. *Phys. Fluids*, 12(7): 1715–1729, 2000.

[83] L. Sirovich. Turbulence and the dynamics of coherent structures. *J. Applied Math.*, 45: 561–590, 1987.

[84] T. L. Thompson, N. M. Komerath and R. B. Gray. Visualization and measurement of the tip vortex core of a rotor blade in hover. *J. Aircraft*, 25(12): 1113–1121, 1988.

[85] C. E. Tinney, M. N. Glauser and L. S. Ukeiley. Low-dimensional characteristics of a transonic jet. Part 1. Proper orthogonal decomposition. *J. Fluid Mech.*, 612: 107–141, 2008.

[86] C. E. Tinney. Proper grid resolutions for the proper basis. *AIAA Paper* 2009-0068, 2009.

[87] C. Tsai and S. E. Widnall. The stability of short waves on a straight vortex filament in a weak externally imposed strain field. *J. Fluid Mech.*, 73: 721–733, 1976.

[88] A. Tsinober and E. Levich. On the helical nature of three-dimensional coherent structures in turbulent flows. *Phys. Lett.*, 99A: 321–324, 1983.

[89] B. G. van der Wall and H. Richard. Analysis methodology for 3C PIV data of rotary wing vortices. *Exp. Fluids*, 40: 798–812, 2006.

[90] V. A. Vladimirov, V. G. Makerenko and V. F. Tarasov. Experimental investigation of non-axisymmetric inertia waves in a rotating fluid. *Fluid Dyn.*, 22: 151–156, 1987.

[91] F. Waleffe. The 3D instability of a strained vortex and its relation to turbulence. *PhD Thesis*, MIT, 1989.

[92] J. Westerweel. Efficient detection of spurious vectors in particle image velocimetry data sets. *Exp. Fluids*, 16(3): 236–247, 1994.

[93] J. Westerweel. Effect of sensor geometry on the performance of PIV interrogation. *Laser Tech. Applied to Fluid Mech.,* 9^{th} *Intl Symp., Lisbon, Portugal*, 37–55, 1998. Springer.

[94] S. E. Widnall. The stability of a helical vortex filament. *J. Fluid Mech.*, 54(4): 641–663, 1972.

[95] S. E. Widnall and J. P. Sullivan. On the stability of vortex rings. *Proc. R. Soc. Lond. A.*, 332: 335–353, 1973.

[96] S. E. Widnall, D. B. Bliss and C.-Y. Tsai. The instability of short waves on a vortex ring. *J. Fluid Mech.*, 66(1): 35–47, 1974.

[97] Y. H. Yu. Rotor blade-vortex interaction noise. *Prog. Aerospace Sciences*, 36(2): 97–115, 2000.

[98] O. Zeman. The persistence of trailing vortices: A modeling study. *Phys. Fluids*, 7: 135–143, 1995.